TECHNISCHE UNIVERSITÄT MÜNCHEN

TUM School of Natural Sciences

Organometallic Network Construction and Modification on Surface

Doctoral Dissertation

Wenchao Zhao

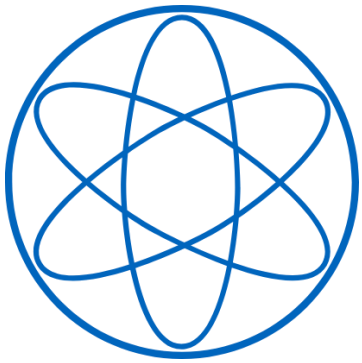

TECHNISCHE UNIVERSITÄT MÜNCHEN

TUM School of Natural Sciences

Organometallic Network Construction and Modification on Surface

Wenchao Zhao

Vollständiger Abdruck der von der TUM School of Natural Sciences der Technischen Universität München zur Erlangung des akademischen Grades eines Doktors der Naturwissenschaften (Dr. rer. nat.) genehmigten Dissertation.

Vorsitz:	Prof. Dr. –Ing. Helge Stein
Prüfer der Dissertation:	1. Prof. Dr. Johannes Barth
	2. Prof. Dr. Angela Casini

Die Dissertation wurde am 24.04.2025 bei der Technischen Universität München eingereicht und durch die TUM School of Natural Sciences am 13.06.2025 angenommen.

Abstract

Two-dimensional molecule-based frameworks have garnered significant interest over the past decades due to their tunable physical and chemical properties, frequently derived from the synergistic combination of organic and metal components. Among these, organometallic networks stabilized by metal-carbon bonds which exhibit covalent nature and reversibility, as a prominent subclass of two-dimensional frameworks, have attracted considerable attention for potential applications in catalysis, optoelectronics, magnetism, etc. The advancement of on-surface synthesis, facilitated by cutting-edge surface-sensitive technologies, has enabled the precise fabrication of single-layered organometallic networks with molecular-level control. Furthermore, the integration of scanning tunneling microscopy/spectroscopy for atomic-resolution visualization and electronic properties characterization, X-ray photoelectron spectroscopy for probing the chemical states of adsorbed molecules, and low-energy electron diffraction for characterizing the spatial arrangement of periodic networks, has allowed for monitoring *in-situ* construction and modification of organometallic networks comprehensively. Complementing the above experimental techniques, density functional theory provides fundamental insights into the underlying mechanisms and supports the interpretation of experimental data sets.

In this thesis, leveraging a suite of surface-sensitive techniques, we systematically explored the construction and modification of organometallic networks on atomically well-defined surfaces using dehydrogenation reactions of amino and alkynyl groups through gas-mediation and transmetalation strategies. First, we investigated the reactivity of aromatic amines on silver and gold surfaces via an unconventional reaction approach. Our findings reveal that O_2-mediated treatment on silver surfaces facilitates oxidative dehydrogenation of aromatic amines, leading to the formation of conjugated network, whereas the same species remain unaltered on Au(111), underscoring the substrate-dependent nature of these reactions. DFT calculations, supported by simulated core-level shifts and microscopy images, elucidate how substrate choice governs the thermodynamics of the reactions.

Next, we introduced a protocol for modifying single-layer organometallic networks through the transmetalation method. By incorporating Cu atoms into an bis-alkynyl-Ag network constructed from 1,3,5-triethynylbenzene on an Ag(111) surface, we

successfully realized its regular bis-alkynyl-Cu counterpart. While retaining the lattice periodicity and pore morphology of the original silver-containing network, the Cu-based structure exhibits enhanced thermal stability, making it more robust for practical applications.

Finally, utilizing a designed bi-component precursor featuring amino and alkynyl groups, combined with O_2-mediated treatment, we constructed ordered Ag-Ag dinuclear organometallic networks with C-Ag-N bridging linkers. Additionally, we demonstrated the ability to tune electronic properties and thermal stability by exchanging metal centers, transforming the well-ordered OMN structures with C-Cu-N linkages. This approach highlights the potential for tailoring functional materials with precise control over their properties.

Zusammenfassung

Zweidimensionale molekülbasierte Gerüststrukturen haben in den letzten Jahrzehnten aufgrund ihrer einstellbaren physikalischen und chemischen Eigenschaften, die häufig aus der synergistischen Kombination organischer und metallischer Komponenten resultieren, großes Interesse geweckt. Unter diesen haben metallorganische Netzwerke, die durch Metall-Kohlenstoff-Bindungen mit kovalentem Charakter und Reversibilität stabilisiert werden, als bedeutende Unterklasse zweidimensionaler Gerüste beträchtliche Aufmerksamkeit für potenzielle Anwendungen in Katalyse, Optoelektronik, Magnetismus etc. erlangt. Die Fortschritte in der On-surface-Synthese, ermöglicht durch moderne oberflächensensitive Technologien, haben die präzise Herstellung einlagiger metallorganischer Netzwerke mit molekularer Kontrolle realisiert. Darüber hinaus ermöglicht der kombinierte Einsatz von Rastertunnelmikroskopie/-spektroskopie zur atomauflösenden Visualisierung und Charakterisierung elektronischer Eigenschaften, Röntgenphotoelektronenspektroskopie zur Untersuchung chemischer Zustände adsorbierter Moleküle sowie Beugung niederenergetischer Elektronen zur Charakterisierung der räumlichen Anordnung periodischer Netzwerke eine umfassende In-situ-Beobachtung von Aufbau und Modifikation metallorganischer Strukturen. Ergänzt durch Dichtefunktionaltheorie, die grundlegende Einblicke in die zugrunde liegenden Mechanismen liefert und die Interpretation experimenteller Daten unterstützt, wird ein ganzheitlicher Forschungsansatz erreicht.

In dieser Arbeit untersuchten wir systematisch – unter Anwendung einer Reihe oberflächensensitiver Techniken – die Konstruktion und Modifikation metallorganischer Netzwerke auf atomar definierten Oberflächen mittels Dehydrierungsreaktionen von Amino- und Alkingruppen durch Gasvermittelungs- und Transmetallierungsstrategien. Zunächst erforschten wir die Reaktivität aromatischer Amine auf Silber- und Goldoberflächen über einen unkonventionellen Reaktionsansatz. Unsere Ergebnisse zeigen, dass eine O_2-vermittelte Behandlung auf Silberoberflächen die oxidative Dehydrierung aromatischer Amine begünstigt, was zur Bildung konjugierter Netzwerke führt, während dieselben Spezies auf Au(111) unverändert bleiben. Dies unterstreicht den substratabhängigen Charakter dieser Reaktionen. DFT-Rechnungen, gestützt durch simulierte Core-Level-Shifts und Mikroskopiebilder, verdeutlichen, wie die Substratwahl die Thermodynamik der Reaktionen bestimmt.

Anschließend entwickelten wir ein Protokoll zur Modifikation einlagiger metallorganischer Netzwerke mittels der Transmetallierungsmethode. Durch Einbringen von Cu-Atomen in ein Bis-Alkinyl-Ag-Netzwerk – aufgebaut aus 1,3,5-Triethinylbenzol auf einer Ag(111)-Oberfläche – gelang uns die gezielte Synthese des entsprechenden Bis-Alkinyl-Cu-Netzwerks. Während die Gitterperiodizität und Porenmorphologie des ursprünglichen silberhaltigen Netzwerks erhalten blieben, zeigte die Kupfer-basierte Struktur eine verbesserte thermische Stabilität, was sie für praktische Anwendungen robuster macht.

Abschließend nutzten wir einen speziell designten Zweikomponenten-Vorläufer mit Amino- und Alkingruppen in Kombination mit einer O_2-vermittelten Behandlung, um geordnete Ag-Ag-dinukleare metallorganische Netzwerke mit C-Ag-N-Verbrückungseinheiten aufzubauen. Zudem konnten wir zeigen, dass sich die elektronischen Eigenschaften und die thermische Stabilität durch Austausch der Metallzentren gezielt einstellen lassen – demonstriert durch die Umwandlung der wohlgeordneten metallorganischen Netzwerke in Strukturen mit C-Cu-N-Bindungen. Dieser Ansatz unterstreicht das Potenzial, funktionelle Materialien mit präziser Kontrolle über ihre Eigenschaften maßzuschneidern.

Contents

Contents

List of abbreviations

2D	Two-dimensional
MOFs	Metal-Organic Frameworks
OMNs	Organometallic Networks
OSS	On-Surface Synthesis
STM	Scanning Tunneling Microscopy
STS	Scanning Tunneling Spectroscopy
XPS	X-ray Photoelectron Spectroscopy
LEED	Low Energy Electronic Diffraction
DFT	Density Functional Theory
AAs	Aromatic Amines
DATP	4,4″-diamino-p-terphenyl
TEB	1,3,5-triethynylbenzene
UHV	Ultra High Vacuum
EABP	4'-ethynyl-[1,1'-biphenyl]-4-amine
OMCs	Organometallic Chains
OMRs	Organometallic Rings
LDOS	Local Density of State
JT-STM	Joule-Thomson Scanning Tunneling Microscopy
OMBE	Organic Molecular Beam Epitaxy
TSP	Titanium Sublimation Pump
LN_2	Liquid Nitrogen
LHe	Liquid Helium
PSD	Photo-Stimulated Desorption
ML	Monolayer
VASP	Vienna ab-initio Simulation Package

1. Introduction

Two-dimensional (2D) materials have emerged as a focal point in modern materials science due to their unique structural and functional properties.[1-6] Among these, 2D molecule-based frameworks, such as metal-organic frameworks (MOFs) and organometallic networks (OMNs), have garnered significant attention for their versatile applications in catalysis, adsorption and separation, and energy.[7-9] These materials, composed of metal ions coordinated with organic ligands, exhibit high surface areas, tunable porosity, and chemical functionality, making them ideal for a wide range of applications.[10-13] Recent advancements in on-surface synthesis (OSS) with the aid of advanced surface-sensitive techniques have further expanded the potential of 2D molecule-based frameworks , which allows for the precise construction of 2D molecule-based frameworks directly on substrates, enabling the development of highly ordered and functional materials with tailored properties.[14, 15] This approach enhances the control over the structural and chemical characteristics of 2D molecule-based frameworks . Modification of 2D molecule-based frameworks has also become a key area of research. By functionalizing the organic ligands or metal nodes, researchers can introduce specific physicochemical properties, such as enhanced catalytic activity or stability. These modifications enable the fine-tuning of 2D molecule-based frameworks for targeted applications, such as sensing, energy storage, and molecular recognition.[16-18] More recently, the development of OMNs on surfaces has unveiled profound insights into their formation mechanisms and stability. These networks hold significant promise for designing novel hybrid systems with tailored electronic and magnetic properties, owing to the unique characteristics of organometallic bonds—such as enhanced interaction strength and reversible behavior—compared to traditional coordination bonds.[19-21]

Meanwhile, the incorporation of functional groups, such as amino and alkynyl groups, into OMNs on surfaces has further expanded their utility. These groups can serve as active sites for chemical reactions, enabling the development of advanced OMNs materials with tailored functionalities. In summary, the integration of designed function groups into OMNs, combined with advancements in on-surface synthesis, modification, and functionalization, represents a rapidly evolving field with immense

potential. In this thesis, we mainly focus on constructing OMNs based on amino and alkylnyl terminated molecular precursors via dehydrogenation promoted by O_2-exposure and tunning the properties of OMNs combined with transmetalation strategy on surface.

Chapter 2 describes the fundamental principles of the applied surface and nanoscience techniques and experimental methods. Scanning tunneling microscopy (STM) is employed for visualizing the molecular adsorption and formation of ordered OMNs on surface. Scanning tunneling spectroscopy (STS) is used to characterize the electronic properties of realized 2D OMNs. X-ray photoelectron spectroscopy (XPS) is applied to study the chemical behavior of the precursor molecules on surface. Low energy electronic diffraction (LEED) is utilized to reveal the periodic structure of the 2D OMNs. Besides, density functional theory (DFT) is applied to rationalize experimental results. In the final part of this chapter, the applied instruments and set-ups are introduced in detail.

In Chapter 3, the first project regarding the on-surface activation of aromatic amines (AAs) is presented. We studied the reactivity of AAs on relatively inert metal substrates, focusing on crystal orientation and substrate activity. We intended to activate the dehydrogenation of 4,4″-diamino-p-terphenyl (DATP) by introducing tiny doses of O_2 gas in UHV system. Using STM and XPS, we observed the oxidative dehydrogenation reaction followed by formation uniform organometallic nanopores on Ag(111) and Ag(100), but not on Au(111). DFT calculations reveal the easier O_2 adsorption on Ag substrates, which lowers the reaction barrier compared to Au(111). This work enhances AAs reactivity on inert surfaces under mild conditions, clarifies oxidative dehydrogenation mechanisms, and expands AAs' potential application in synthesizing low-dimensional organic materials via OSS.

In Chapter 4, we introduce a transmetalation strategy to modify OMNs on surfaces. Using STM, LEED, XPS, and DFT calculations, we demonstrated the post-synthetic transmetalation of single-layer OMNs from alkynyl-Ag-alkynyl to alkynyl-Cu-alkynyl. Starting with a 1,3,5-triethynylbenzene (TEB) precursor, extended Ag-TEB OMN were synthesized on Ag(111) under ultra high vacuum (UHV) via gas-mediated method with O_2. Depositing Cu atoms and annealing transforms ordered Ag-TEB into well-defined Cu-TEB OMN, which cannot be directly formed on Cu(111). The Cu-TEB OMN exhibits higher thermal stability while maintaining lattice periodicity and pore symmetry. This strategy offers a simple method to engineer robust, carbon-based 2D nanomaterials under controlled conditions.

1. Introduction

In Chapter 5, by employing a well-designed bi-component uni-molecule precursor 4'-ethynyl-[1,1'-biphenyl]-4-amine (EABP) with amino and alkylnyl groups, we synthesized dinuclear EABP-Ag OMNs linked by C-Ag-N structure and Ag-Ag interation on Ag(111) after O_2 treatment. Furthermore, by depositing Cu atoms and proper annealing, we replaced the Ag metal center with Cu forming well-ordered EABP-Cu OMN, with the similar structural periodicity. STS measurement revealed electronic confinement in the OMN. Interestingly, annealing at 425 K transformed EABP-Cu OMNs into chiral organometallic rings (OMRs) at low molecular coverage. This work advances the design and application of multinuclear organometallic supramaterials.

At the last, in Chapter 6, the main accomplishments of these projects are summarized, which describes the significance of the projects and their contributions to the OSS field, along with their potential to inspire future research. Additionally, exciting prospects and promising directions for further exploration are presented, laying the groundwork for continued progress and innovation in the area.

2. Experimental Methods and Techniques

In this chapter, the fundamental principles of the experimental methods and techniques employed in this study are described. Scanning tunneling microscopy/spectroscopy is utilized for atomic-resolution visualization and characterization of electronic properties. X-ray photoelectron spectroscopy is employed to investigate the chemical states of molecules on surfaces, while low-energy electron diffraction is used to characterize the spatial structure of the obtained networks. Additionally, density functional theory provides essential theoretical insights into the underlying mechanisms and supports the interpretation of the experimental results.

2.1 Scanning tunneling microscopy (STM)

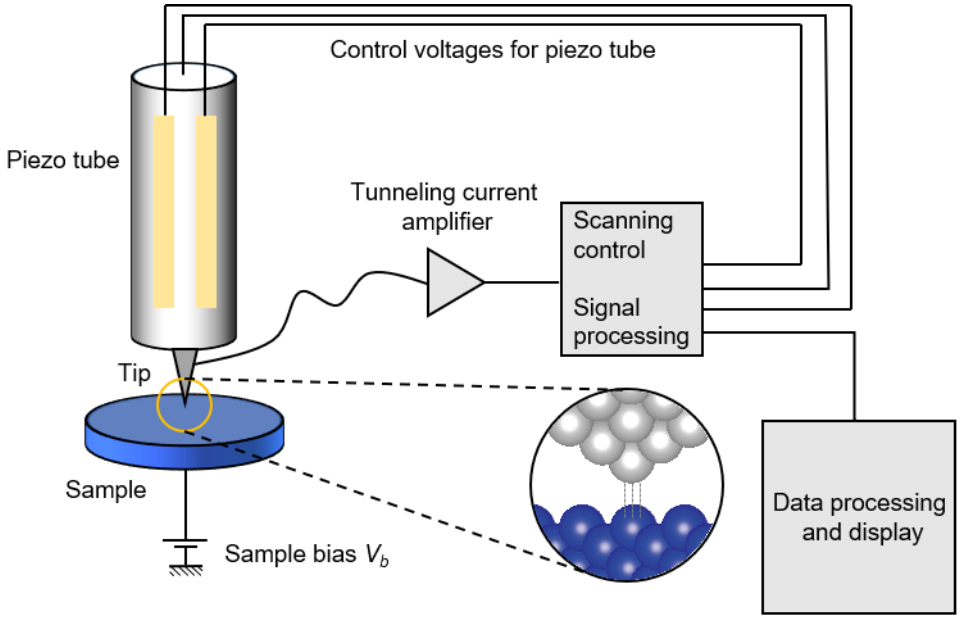

Figure 2.1: A simplified schematic of the working principle of STM. The tip is positioned and moved using a piezo tube, which is controlled by applying a voltage to the piezo. When the tip is brought sufficiently close to the sample surface and a bias voltage is applied, a tunneling current is generated between the tip and the sample. This current is used to probe the surface at the atomic scale.

Scanning tunneling microscopy (STM) is a powerful tool for characterizing nanostructures on surfaces with atomic-level spatial resolution. It is based on the quantum tunneling effect and was invented by Gerd Binnig and Heinrich Rohrer at the IBM Zurich Research Laboratories.[22] Their groundbreaking work earned them the ½ Nobel Prize in Physics in 1986. STM has revolutionized the ability to visualize materials at the atomic level, achieving resolutions of approximately 1 Å laterally and 0.1 Å vertically, or even better. This capability enables in-situ investigation of surface adsorption processes. When combined with scanning tunneling spectroscopy (STS), STM also allows for the study of electronic properties of material surfaces, providing a comprehensive understanding of both structural and electronic characteristics.

2.1.1 Basic principle of STM

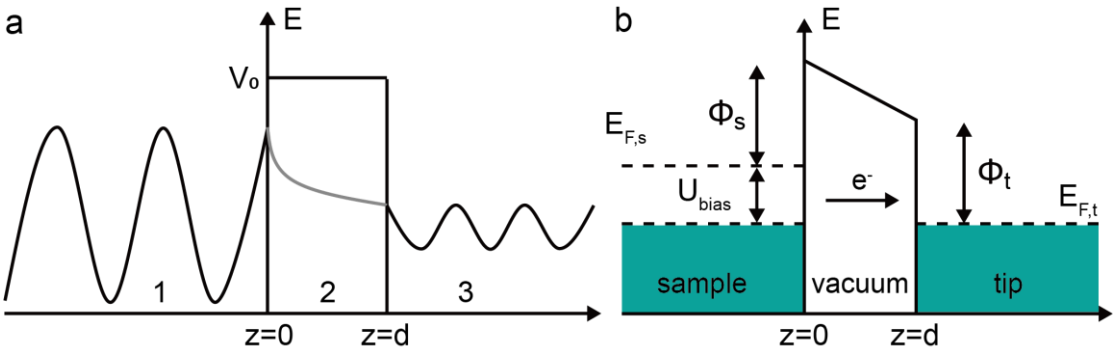

Figure 2.2: scheme illustration of quantum tunneling effect and the tip-sample tunneling model of STM. (a) The electron wave function penetrates the potential barrier with energy of V0 from region 1 to region 3, while the energy has a huge decay at the barrier region. (b) The applied voltage adjusts the fermi level alignment between tip and sample, which leads an electron tunneling through the potential barrier.

The quantum tunneling effect is a phenomenon in quantum mechanics, which mainly refers to the ability of microscopic particles to pass through potential barriers that cannot be crossed in classical physics.[23] STM relies on the quantum tunneling effect to complete the real-space high-resolution characterization of the surface.

In classical physics, a particle with energy E cannot pass through a potential barrier of height V_0 when $V_0 > E$. However, in quantum mechanics, microscopic particles such as electrons exhibit wave-like behavior, enabling them to tunnel through a potential barrier even if its height exceeds their energy. This phenomenon, known as quantum tunneling, occurs with a certain probability, although the likelihood decreases

significantly as the barrier height V_0 or width d increases, which is shown in Figure 2.2a considering a rectangular potential barrier with height V_0 and width d . Importantly, the barrier height must remain within a finite range for tunneling to be observable. This principle is fundamental to the operation of STM, where electrons tunnel between a tip and a sample surface, allowing atomic-scale imaging and spectroscopy. In the three regions in Figure 2.2, the wave function of the particles can be described by the Schrödinger equation(one-dimensional and time-independent, for simplicity here):

$$-\frac{\hbar^2}{2m}\frac{d^2\Psi}{dz^2} + V(z)\Psi = E\Psi \tag{2.1}$$

where $\hbar$ is the reduced Planck constant and m is the electron mass. As an incoming wave propagating in the positive z-direction (Figure 2.1a, 1→3), the wave function solutions can be written into:

$$\Psi_{1,3} = e^{\pm ikz}, k = \frac{\sqrt{2mE}}{\hbar} \tag{2.2}$$

$$\Psi_2 = e^{-kz}, K = \frac{\sqrt{2m(V_0-E)}}{\hbar} \tag{2.3}$$

From the equations, the transmission probability T of the electron is:

$$T = \frac{16k^2K^2}{(k^2+K^2)^2}e^{-2Kd} \tag{2.4}$$

Based on the above solutions, the barrier width and the energey difference between particles and the potential barrier determine the transmission probability, which contribute the high resolution of STM.

In the context of STM tunneling between the tip and the sample surface, the vacuum gap between them determines the width d of the potential barrier. Under tunneling contact, the Fermi levels of the tip and the sample are aligned. However, when a bias voltage U_{bias} is applied, the Fermi levels shift, creating an energy offset that drives the tunneling current. To accurately describe the tunneling current, Bardeen introduced a theoretical framework based on many-particle interactions.[24] This model was later adapted by Hamann and Tersoff[25], who expressed the tunneling current as follows:

$$I = \frac{2\pi e}{\hbar}\sum_{t,s} f(E_t)[1 - f(E_s + eU)]|M_{ts}|^2\delta(E_t - E_s) \tag{2.5}$$

with $f(E)$ being the Fermi function, U being the applied bias, M_{ts} being the tunneling matrix element, E_t being the energy of the wave function of the tip (Ψ_t) and E_s being wave function of the sample (Ψ_S). The δ function describes the conversion of the energy when elastic tunneling happens. However, considering the low-temperature and the small applied voltage, the equation can be simplified as:

$$I = \frac{2\pi}{\hbar} e^2 U \sum_{t,s} |M_{ts}|^2 \delta(E_s - E_F)\delta(E_t - E_F) \quad (2.6)$$

with E_F being the Fermi level, M_{ts} being the tunneling matrix element. The M_{ts} presents the integral over the surface which is determined by the tip and the sample and can be expressed as:

$$M_{ts} = -\frac{\hbar^2}{2m} \int_S \left(\Psi_t^* \vec{\nabla} \Psi_s - \Psi_s \vec{\nabla} \Psi_t^*\right) dS \quad (2.7)$$

from Equation 2.7, calculating the tunneling matrix element is challenging due to the difficulty in determining the precise shape of the tip, which leads to uncertainties in the wave functions of both the tip and the sample. To address this issue, Tersoff and Hamann proposed a simplified model in which the tip is assumed to be spherical with a radius R and center position of $\overrightarrow{r_0}$. Under this assumption, and by further assuming that the wave functions of the tip and the sample are identical, the tunneling current can be expressed in a more tractable form. This approach provides a practical framework for analyzing tunneling phenomena in STM.:

$$I = \frac{32\pi^3 e^2 V \Phi^2 R^2 e^{2KR}}{\hbar K^4} D_t(E_F) \sum_s |\Psi_s(\overrightarrow{r_0})|^2 \delta(E_s - E_F) \quad (2.8)$$

while the D_t is the density of states per unit volume of the tip. Based on the equations, the local density of state (LDOS) of the surface at Fermi level can be expressed as:

$$\rho_s(\overrightarrow{r_0}, E_F) = \sum_s |\Psi_s(\overrightarrow{r_0})|^2 \delta(E_s - E_F) \quad (2.9)$$

meanwhile, the wave function of surface oriented to the vacuum can be expressed as:

$$\Psi_s(\overrightarrow{r_0}) \propto e^{-Kz}, z = d + R \quad (2.10)$$

from Equations 2.8 and 2.10, it is evident that the tunneling current is strongly dependent on both the distance between the tip and the surface and the LDOS of the surface. This relationship enables STM to simultaneously characterize the surface morphology and the electronic properties, including the behavior of adsorbates on the surface. By measuring variations in the tunneling current, STM provides atomic-scale insights into both the physical and electronic structure of surfaces and adsorbed species.

2.1.2 Scanning tunneling spectroscopy (STS)

In addition to characterizing surface morphology, an extended functionality of the STM, known as scanning tunneling spectroscopy (STS), enables the investigation of the LDOS of adsorbates on the surface.[26] As indicated by equation 2.6, the tunneling current corresponds to an integral over the energy window eV, and spectroscopic information can be resolved through its first derivative. Under the assumptions that the

tip has a constant LDOS, operates within limited voltage ranges, and exhibits negligible variations in transmission probability, the differential conductivity can be expressed as:

$$\frac{dI}{dV} \propto \rho_s(eV) \tag{2.11}$$

where V denotes the applied voltage and ρ_s represents the LDOS of the sample. This relationship explains how STS can be utilized to characterize the LDOS of the sample, providing detailed insights into its electronic properties at the atomic scale.

To improve the signal quality of dI/dV, an advanced method known as the lock-in technique is commonly employed. A small modulation voltage, with a frequency higher than that of the feedback system, is superimposed on the tunneling junction. The lock-in amplifier then extracts the corresponding variation component of the tunneling current, which matches the reference frequency and phase, while simultaneously suppressing noise and other frequency components. This process significantly enhances the signal-to-noise ratio, ensuring more accurate and reliable measurements of the LDOS of the sample.

2.1.3 STM imaging

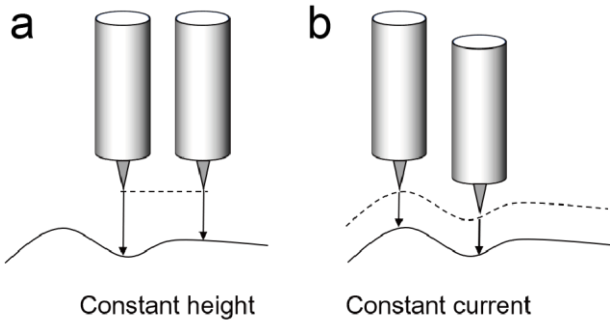

Figure 2.3: Two scanning modes of an STM. (a) The feedback loop is turned off, and the z-position of the tip remains fixed during scanning. In this mode, variations in the tunneling current are measured, reflecting changes in the surface topography and the LDOS. (b) The feedback loop is activated, and the tunneling current is maintained at a fixed value. To achieve this, the z-position of the tip is continuously adjusted based on the surface topography. This mode provides a direct mapping of the surface morphology by recording the vertical movements of the tip. These two modes enable STM to characterize surfaces with atomic precision, offering insights into both topographic and electronic properties.

As illustrated in Figure 2.1, the tip mounted on the scanner can be precisely driven in both lateral and vertical directions by a piezoelectric tube. When the tip is brought sufficiently close to the sample surface and a bias voltage is applied, a tunneling current is generated between the tip and the sample due to the quantum tunneling effect. The

resulting height and current signals are subsequently recorded and analyzed for further processing.

Two scanning modes of STM are employed during the imaging process, as depicted in Figure 2.3. The constant current mode is typically used to characterize the morphology of large surface areas, as the feedback loop ensures the tip maintains a safe distance from the sample, preventing crashes. In this mode, the distance between the tip and the sample is adjusted to keep the tunneling current constant. Consequently, the z-position of the tip varies as a function of the surface topography. On the other hand, the constant height mode is primarily utilized to measure variations in tunneling current, which reflect both the surface morphology and the local density of electronic states. In this mode, the z-position of the tip remains fixed after the feedback loop is turned off. As a result, changes in the tunneling current are directly related to the distance between the tip and the sample, as well as the electronic properties of the surface.

2.2 X-ray photoelectron spectroscopy (XPS)

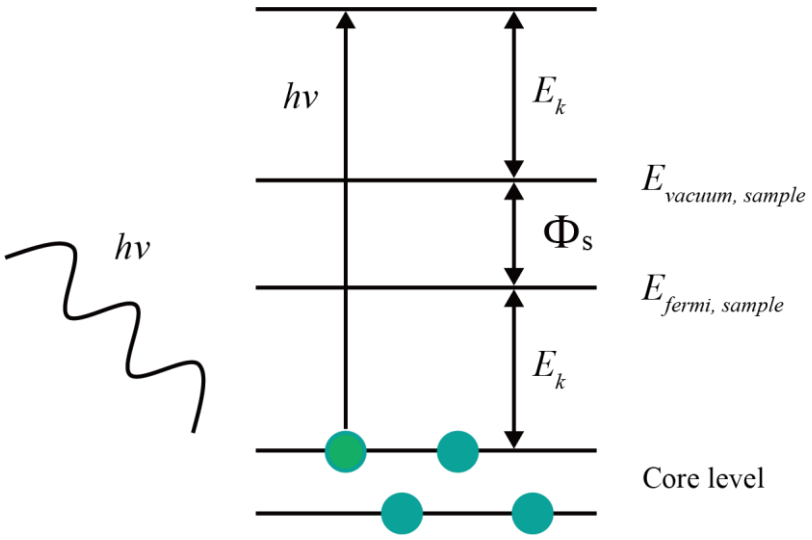

Figrue 2.4: Scheme illustration of the principle for XPS. The photons with energy of *hv* eject the core level electrons of the atoms with a kinetic energy $E_{k,}$ which is related to the binding energy E_b of the electrons. The element component and chemical environment can be investigated via measuring E_k

X-ray photoelectron spectroscopy (XPS) is a surface-sensitive analytical technique used to study the elemental composition, chemical state, and electronic structure of materials. It is based on the photoelectric effect, which describes the emission of electrons from a material when it is irradiated with X-rays.[27, 28] Typically, Al K_α and Mg K_α are used as anode materials for X-ray sources, providing energy in the range of 100

eV to 2000 eV. The inelastic mean free path of electrons in materials typically ranges from 0.5 to 3 nm within the energy range mentioned above.[29] This is the reason why XPS is highly surface-sensitive, as it primarily probes the top few nanometers of the sample. During the irradiation process, X-rays with energy higher than the binding energy of core-level electrons in the sample's atoms cause the ejection of these electrons as photoelectrons. The emitted photoelectrons travel through the material, escape from the surface, and overcome the work function of the material. These photoelectrons are then collected by a hemispherical electron energy analyzer, which measures their kinetic energy E_k (cf. Figure 2.4). The kinetic energy of the photoelectrons depends on several factors, including the energy of the incident X-rays ($h\nu$), the binding energy (E_b) of the core-level electrons with respect to the Fermi level, and the work function Φ of the material. This relationship can be expressed as:

$$E_k = h\nu - E_b - \Phi \tag{2.12}$$

from the equation 2.12, the binding energy E_b of the electrons can be revealed using the measured kinetic energy E_k. The binding energy of core-level electrons is characteristic and specific to each element, providing information about both the elemental composition and the chemical environment. The formation of chemical bonds alters the screening of the positive nuclear charge, leading to shifts in the binding energy. These shifts, known as chemical shifts, offer insights into the oxidation states and bonding configurations of the elements. Furthermore, the intensity of the spectral peaks corresponds to the abundance of the elements, allowing for quantitative analysis of the sample's composition. Thus, XPS not only identifies elements but also reveals their chemical states and relative concentrations.

2.3 Low-energy electron diffraction (LEED)

Low-energy electron diffraction (LEED) is a powerful technique for visualizing the periodic structure of a surface. In this method, an electron beam with an energy range of 5-250 eV is generated and accelerated through an electron gun, directed towards the sample surface along the incidence direction. The interaction of the electrons with the surface produces a diffraction pattern, which is then displayed on a fluorescent screen (see Figure 2.5a). The wavelength of the electrons, ranging from 1 to 5 Å, is comparable to the interatomic distances, making atomic diffraction possible. Furthermore, the mean free path of the electrons is approximately several atomic layers, which renders LEED a highly surface-sensitive technique. The retarding grid system is employed to ensure that only elastically scattered electrons reach the fluorescent screen, operating through the following steps: Initially, the first grid is grounded to create a field-free environment,

allowing the scattered electrons to travel unimpeded. Subsequently, the second grid, biased with a voltage close to the energy of the primary electron beam, filters out inelastically scattered electrons, permitting only the elastically scattered ones to pass. Finally, these elastically scattered electrons are accelerated by a bias applied to the fluorescent screen, where they produce bright spots upon impact, forming the diffraction pattern.

Figure 2.5b illustrates the conditions for elastic scattering using the Ewald sphere construction. In this representation, the incident wave vector and the scattered wave vector have equal magnitudes, satisfying the relationship described by the following equation:

$$k_f - k_i = G \tag{2.13}$$

In the equation 2.13, k_f presents the scattered wave vector, k_i denotes the incident wave vector and G is the reciprocal lattice vector of the sample surface. Additionally, the scattered wave vector must align with the intersection point between the Ewald sphere and the lattice rod. Consequently, the diffraction pattern observed on the fluorescent screen, which is subsequently captured by a camera, provides detailed structural information about the investigated surface.

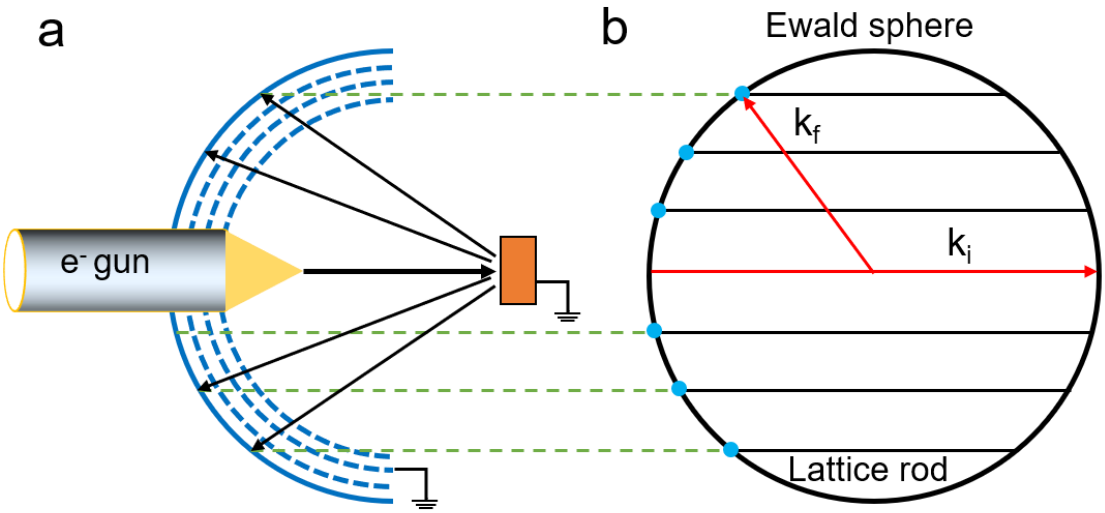

Figure 2.5: (a) Scheme illustration of LEED set-up used in UHV environment. Electrons from the electron gun strike the sample, scattering off the surface. Retarding grids filter out inelastically scattered electrons, allowing only elastic ones to reach the fluorescent screen, forming a diffraction pattern that reveals the surface atomic arrangement. (b) The Ewald sphere describes elastic scattering on a periodic structure. The incident and scattered wave vectors have equal length and must match a reciprocal lattice vector. This condition generates diffraction spots, reflecting the surface's crystal structure and symmetry.

2.4 Instrumentation

This section provides an overview of the experimental setup, including the instruments employed, sample preparation procedures, and data acquisition methods utilized in the experiments conducted at the E20 laboratory within the Department of Physics at the Technical University of Munich.

2.4.1 Joule-Thomson STM

All STM measurements presented in this thesis were performed using a commercial Joule-Thomson STM (JT-STM) set-up (see Figure 2.6). This advanced instrument, capable of reaching a low temperature of 1.2 K through the Joule-Thomson effect combined with a cryostat, comprises two main chambers: a preparation chamber and an STM chamber. Both chambers maintain an UHV environment with a base pressure below 2.0×10^{-10} mbar through a comprehensive pumping system, which are essential for the preparation of molecular samples on clean single-crystal surfaces. To minimize external interference, the instrument is isolated from low-frequency vibrations through a noise reduction system incorporating pneumatic damping feet.

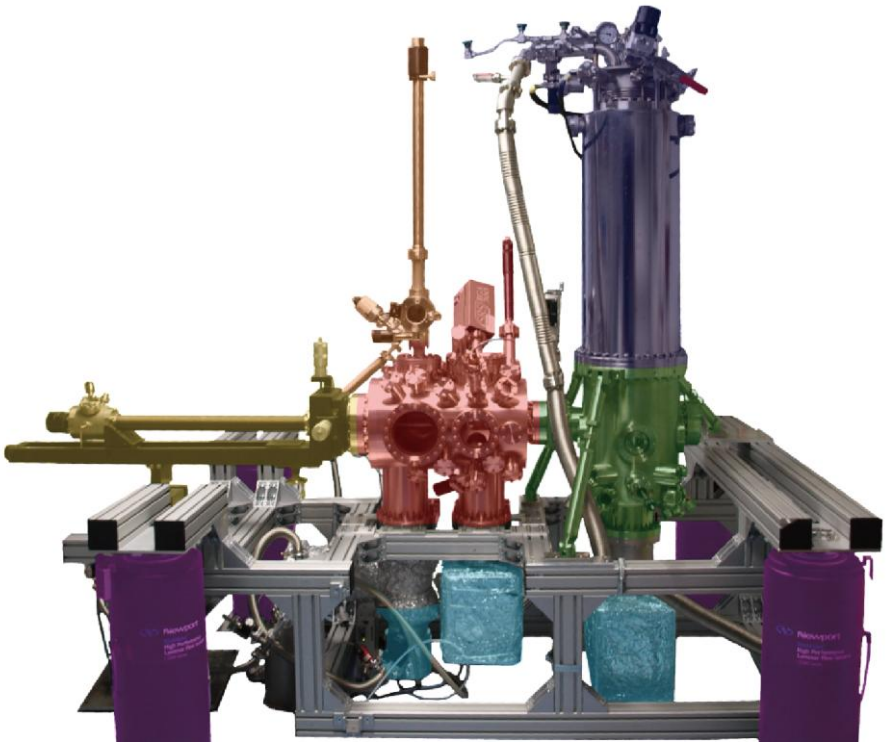

Figure 2.6: Overview image of JT-STM chamber.[30, 31] Load-lock for sample transfer from outside (orange), cryostat (pale purple), STM chamber (green), preparation chamber (red), manipulator (yellow), pneumatic damping feet (purple) and pumping

system (blue).

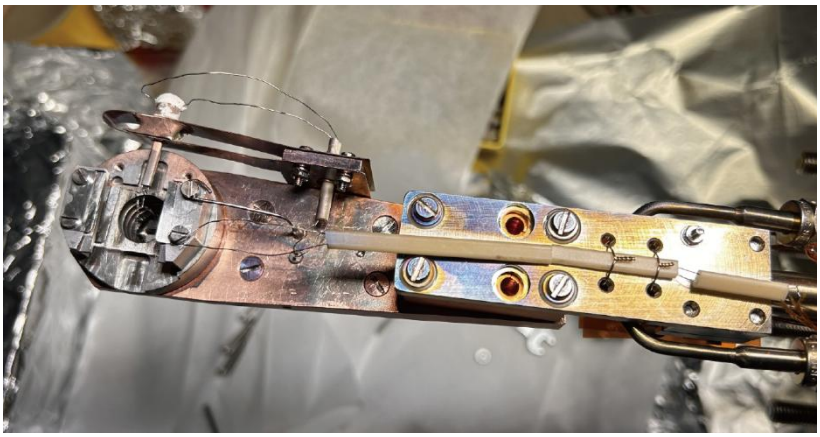

Figure 2.7: Image of manipulator employed in JT-STM preparation chamber.

UHV chamber. The vacuum chamber is divided into two sections, separated by a valve that permits the passage of the manipulator. The preparation chamber (marked in red in Figure 2.6) is equipped with several essential components: a load-lock system, metal evaporators, an organic molecular beam epitaxy (OMBE) apparatus and a mass spectrometer. The load-lock system serves as a transition chamber for transferring crystals, STM tips, and other samples from the external environment into the UHV system. During the transfer process, the load-lock chamber is protected by a nitrogen atmosphere to prevent contamination. A pumping station is employed to pump the load-lock chamber to the required low-pressure conditions. The preparation chamber is further equipped with a manipulator incorporating a heating filament and thermocouple (cf. Figure 2.7), which allows sample preparation procedures as detailed in the following sections.

To achieve and sustain UHV environment, a comprehensive triple-stage pumping system is integrated into the chamber, with pressure inside monitored by cold cathode gauges. The pumping system begins with a diaphragm pump as the first stage, capable of reaching a base pressure of 3 mbar, which establishes the pre-vacuum conditions for the subsequent stages. The second stage employs a small turbo pump, achieving a pressure of 5.0×10^{-9} mbar for the third stage. The final stage consists of a turbomolecular pump with magnetic bearings, directly connected to the preparation chamber to ensure optimal vacuum performance. In addition to the mechanical pumping system, ion pumps are utilized to maintain the UHV conditions in both the preparation and STM chambers, as indicated by the blue components in Figure 2.6. The ion pump operates through an assembly of cylindrical anodes positioned between two

parallel cathodes. Under an applied potential of 7.0 kV, field-emitted electrons ionize residual gas particles within the pump. A uniform magnetic field, generated by permanent magnets, encompasses the entire electrode system, enhancing the ionization efficiency and ensuring stable UHV conditions. Additionally, a titanium sublimation pump (TSP) is installed beneath the preparation chamber to further enhance the ultra-high vacuum conditions. This pump operates by heating a titanium filament to its sublimation temperature, releasing titanium vapor that deposits on the chamber walls. The freshly deposited titanium film acts as a highly effective getter material, chemically adsorbing residual gas particles such as hydrogen, oxygen, and nitrogen within the chamber. This process significantly reduces the partial pressures of reactive gases, thereby optimizing the overall UHV environment. In addition to the above equipment within the UHV chamber system, a suite of techniques is utilized for noise reduction to obtain great conditions for STM and STS measurements. Firstly, four pneumatic damping feet are applied underneath the UHV chamber to isolate vibration from the external environment. Moreover, as shown in Figure 2.8a, the STM stage is isolated by copper beryllium springs. Furthermore, an eddy-current mechanism, utilizing fixed magnets positioned opposite to copper wings, is installed beneath the STM stage. To reduce the affection from capacitive effects and crosstalk within the cables, coaxial wires are employed for the current and voltage lines, while the feed lines for the piezoelectric unit and the temperature sensor are equipped with low-pass filters. Additionally, copper beryllium springs and damping elements are installed between the liquid nitrogen (LN_2) and liquid helium (LHe) tanks to attenuate the resonant frequencies induced by the cryostat's system.

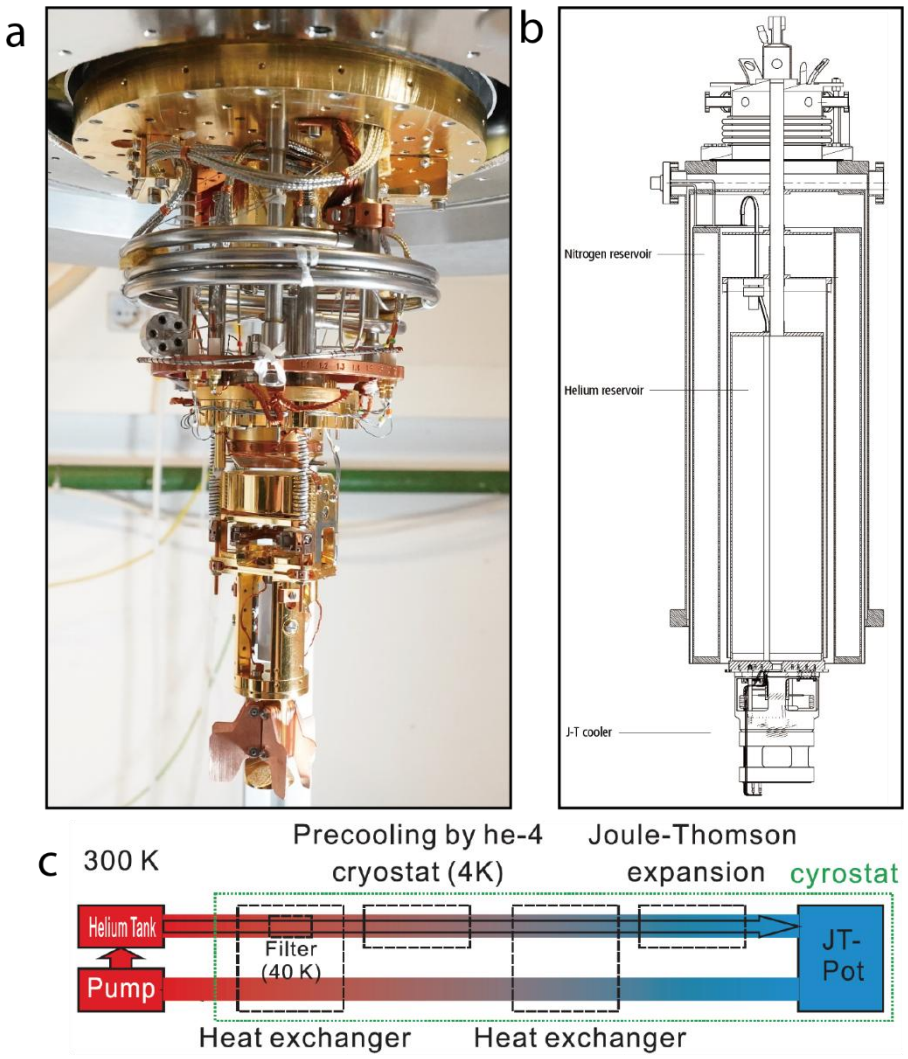

Figure 2.8: (a) Image of STM head hanging on suspension springs combined with cooling stage. (b) Scheme image of JT-STM cryostat, including three cooling stages.[32] (c) Scheme of principle of Joule-Thomson effect applied on JT stage.[33]

Cryostat. Figure 2.8b illustrates the schematic of the JT-STM cryostat. The outer tank serves as a LN_2 reservoir, which minimizes the depletion of the LHe from inner reservoir. By utilizing LHe, the STM head can achieve and maintain a temperature of approximately 4.5 K. In this thesis, all experiments, including STM and STS measurements, are conducted at LHe temperature. However, through the Joule-Thomson effect (Figure 2.8c), a lower temperature of approximately 1.2 K can be achieved using a specialized JT cooler system, providing an optimal condition for STS measurements due to reduced thermal broadening. To activate the JT cooling, the STM stage and JT pot are first pre-cooled to the LHe temperature of 4.5 K. Pure helium gas

is then introduced into the JT pot from an external source at room temperature through a long tube. During this process, the helium gas is pre-cooled and condensed into liquid helium, which is collected in the JT pot. Subsequently, when the JT pump, located in a vibration-isolated decoupled box, is activated, the liquid helium in the JT pot is pumped and expands into vapor through a tiny capillary with a diameter of 90 µm. This Joule-Thomson expansion results in a temperature dropping to approximately 1.2 K. To maintain this low temperature, the JT pot must be thermally decoupled from the LHe tank cooling plate. Both ^{3}He and ^{4}He can be used in this process.

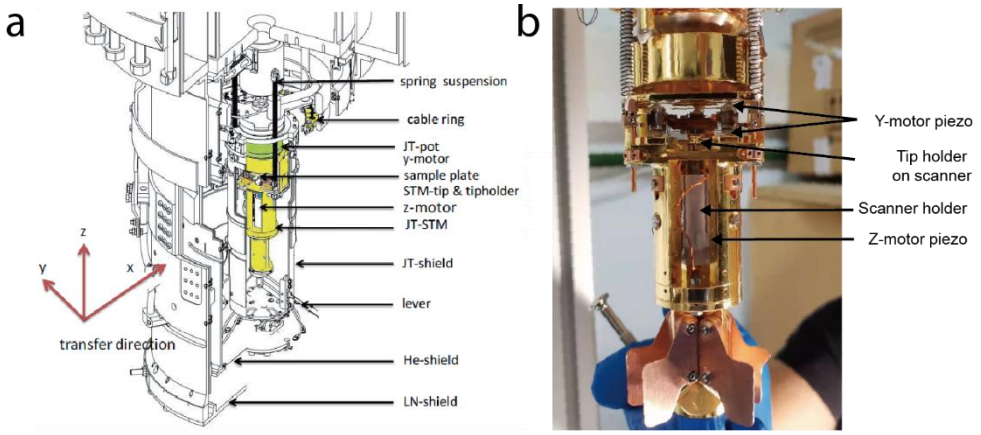

Figure 2.9: (a) Schematic diagram of the STM head, highlighting its key components.[34] (b) Photograph of the actual STM head, with the X and Y motor piezos and the tip holder clearly labeled.

STM head. Figure 2.9a presents a schematic illustration of the STM head, which is positioned inside three radiation shields beneath the cryostat. The STM head is constructed from a stiff material characterized by low eigenfrequency and high thermal conductivity. As depicted in Figure 2.9b, a sample track is positioned above the tip holder, which is mounted on the scanner. The crystal, mounted on a Mo sample holder, can only be inserted into the sample track along one direction (X direction, as indicated in Figure 2.9a) using a wobble stick. Meanwhile, the Y-motor (range: 5 mm) is employed to move the sample track in the Y direction by adjusting the amplitude and frequency of the voltage applied to the piezo. Once the sample is positioned appropriately in the Y direction, the coarse approach of the tip is performed. The lateral position of the tip is adjusted using the Z-motor (range: 10 mm), which is driven by six shear piezo mounted on a sliding sapphire surface. After these adjustments, the radiation shields are closed to cool the sample down to a constant temperature.

2.4.2 XPS and LEED using the “PSD” chamber

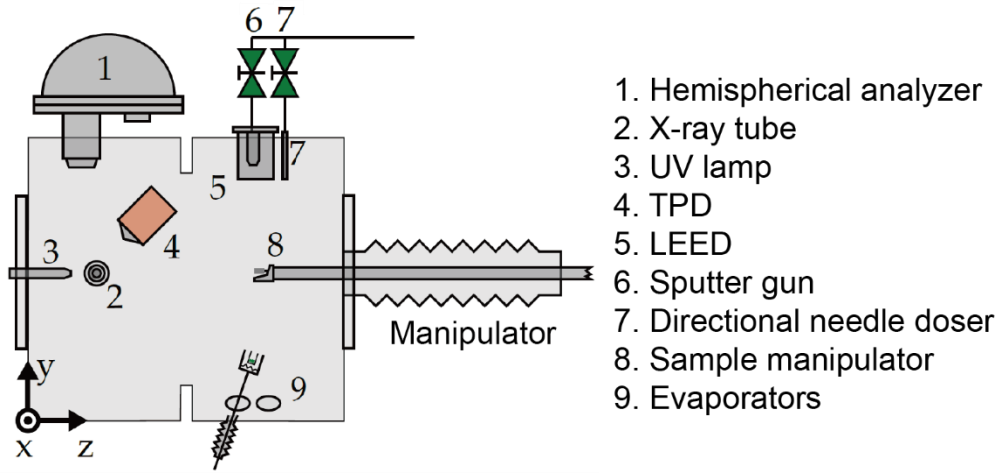

Figure 2.10: Scheme of “PSD” chamber with highlighted main techniques, cited from the thesis of Felix Haag[35].

The PSD (photo-stimulated desorption) chamber is maintained in an UHV environment with a base pressure of approximately 1.0×10^{-10} mbar, achieved using a pump system similar to that of the JT-STM chamber. The chamber is equipped with several surface-sensitive techniques, including XPS, UPS, LEED and TPD, as illustrated in Figure 2.10. In this thesis, we focus on the XPS and LEED setups, which are described in detail below. The manipulator in the chamber is designed for sample preparation and can hold the sample above a filament. It allows for adjustments in the x, y, and z directions, as well as rotation, to align the sample with evaporators and measurement setups. Additionally, liquid nitrogen can flow through the manipulator to cool the sample to 88 K. For XPS analysis, a SPECS Phoibos 100 CCD hemispherical electron analyzer is used. The SpecsLab2 software (version 2.74-r24090) is employed to record the XP spectra. The X-ray source is a home-built X-ray tube featuring two anodes that provide non-monochromatized Al K_α and Mg K_α radiation, with central photon energies of 1486.6 eV and 1253.6 eV, respectively. The X-ray tube is cooled by a water-cooling system and maintained under vacuum by an ion pump. The Al anode operates at 280 W (28 mA, 10 kV), while the Mg anode operates at 200 W (20 mA, 10 kV). A LEED device (model BDL800IRLMX-ISH) from OCI Vacuum Microengineering Inc. is mounted on the front of the chamber. The collimated electron beam is directed onto the sample, and the backscattered electrons produce a diffraction pattern on a fluorescent screen. This pattern is captured and recorded using a camera for further analysis.

2.4.3 Sample preparation

All samples were prepared on a single-crystal Ag(111) surface using a standardized procedure. Initially, an atomically clean surface was achieved through multiple sputtering-annealing cycles in an UHV chamber. Subsequently, organic molecules were deposited onto the pristine surface maintained at room temperature. To initiate the surface reaction, two distinct approaches were employed: a gas-mediated strategy and thermal activation. The gas-mediated process involved the introduction of reactive gases into the preparation chamber, while thermal activation was achieved by precisely heating the sample using a controlled heating system.

In this thesis, four single-crystal substrates - Ag(111), Ag(100), Au(111), and Cu(111) - were employed as platforms for surface reaction. The contamination was effectively removed through Ar^+ ion bombardment, where the Ar^+ ion were generated by an electron beam with a stable emission current of 10 mA under an voltage of 0.9 kV, while maintaining a controlled Argon gas pressure of 3.5×10^{-6} mbar in the preparation chamber. Subsequently, the samples underwent thermal annealing at optimized temperatures: 770 K for Ag(111) and Ag(100), 720 K for Au(111), and 690 K for Cu(111). This annealing process served two purposes: (1) facilitating surface reconstruction through controlled metal atom diffusion to achieve well-defined crystalline surfaces, and (2) ensuring complete removal of residual contamination and argon from the sputtering process.

The applied molecule precursors were deposited on the prepared clean substrate from an organic molecule beam epitaxy (OMBE), which connected to the preparation chamber. Meanwhile the extrinsic Cu atoms were dosed from a home-made evaporator with metal wire. The copper wire was supplied by GoodFellow GmbH and was wound around a central tungsten wire. The power output voltage was adjusted via amplifier to make the wire glowing and obtain a steady flux, such that the Cu deposition could be controllable and reproducible. 4,4′-diamino-p-terphenyl (DATP) with a purity of 98% was purchased from TCI Deutschland GmbH. The precursor molecules of DATP were evaporated from a quartz crucible held at 410 K onto the freshly prepared substrates, followed by exposing to O_2 atmosphere at 200/300 K (~1.33×10^{-6} mbar, 5 mins). The precursor TEB powder was loaded into a glass vial connected to a needle via a flange with attached leak valve in order to finely control the molecule flow. After evaporating the appropriate amount of molecules onto the surface at room temperature, the sample was exposed to O_2 atmosphere (~1.33×10^{-6} mbar, 60 seconds) and subsequently annealed at 375 K. Afterwards, Cu was deposited on the surface at room temperature, followed by annealing at 500 K to obtain an ordered and clean Cu-TEB OMN. 4'-Ethynyl-[1,1'-biphenyl]-4-amine (EABP) was synthesized by Nitika Grover and Mathias O. Senge from 4-iodo-4’nitro-1,1’-biphenyl[36] following the procedure described by Xie and Seto[37]. The molecule precursor EABP was deposited from a quartz

crucible held at 315 K on a freshly cleaned surface, followed by O_2-treatment at room temperature. The Cu atoms are deposited on the former sample, followed by the annealing at 375 K to get a neat EABP-Cu OMN.

2.4.5 Data acquisition and analysis

STM data. All STM images were recorded at constant current mode (unless mentioned otherwise), and the bias voltage was applied to the sample. The STM images were analyzed by Igor software and WSxM[38] programme.

XPS data. All XPS measurements were conducted using the non-monochromatized Mg Kα radiation line ($h\nu$ = 1253.6 eV) from a conventional dualanode source and a SPECS Phoibos 100 CCD hemispherical analyzer within a home-built UHV chamber. The XPS data is analyzed by Igor and CasaXPS[39] software.

LEED data. Experimental LEED patterns were acquired at 90 K using an OCI Vacuum Microengineering (BDL800IRLMX-ISH) apparatus. LEEDpat4 software[40] was applied to analyze LEED patterns.

DFT Calculations. In Chapter 3, density functional theory calculations were performed by Vienna ab-initio Simulation Package (VASP).[41] The electron-ion interactions were described by projector augmented wave method.[42] The exchange-correlation interactions were treated by the van der Waals density functional developed by Hamada, denoted as rev-vdWDF2,[43] which has been shown to describe the adsorption of hydrocarbons on Ag(111) and Au(111) accurately.[44, 45] The cutoff energy for the plane wave basis was set as 400 eV. The Ag(111) and Au(111) surfaces were modeled by four-layered slab with a $p(6\times6)$ supercell. The periodic-image interactions were avoided by employing a 15 Å vacuum layer. A 4×4×1 grid was employed to sample the Brillouin zone. The transition states of dehydrogenations were identified by combining climb image nudge elastic band and the dimer method,[46, 47] where CI-NEB methods was employed to provide an initial guess and the saddle point was further identified by the dimer method. All structures including local minima and saddle points were optimized until the residual force acting on all atoms were below 0.02 eV/Å, except the bottom two layers of metal surfaces which were kept frozen. The STM images were simulated by the Tersoff-Hamman approximation with the implementation by Lorente and Persson.[25, 48] This calculation work is done in cooperation with Kaifeng Niu, Johanna Rosen and Jonas Björk.

In Chapter 4, we employed DFT within the Kohn-Sham formalism using the QuickStep module[49] built in the package CP2K (https://www.CP2K.org/). We utilized the generalized gradient approximation of Perdew, Burke and Ernzerhof[50] as the

approximation to the exchange-correlation term and the empirical potential D3[51] to account for the missing London dispersion forces, Perdew-Burke-Ernzerhof (PBE) +D3. Our calculated lattice constant for Ag is 4.084 Å. We modelled the Ag(111) surface with a slab of five layers of the substrate, with the two top-most layers allowed to relax, and H passivation on the bottom surface. We used an equi-distance mesh of 4x4 k points in the hexagonal cell and of 2x4 k points in the rectangular cells in the integrals over the first Brillouin zone. Pseudo potentials,[52] with a valence of 11 electrons on Cu and Ag, were employed together with Gaussian basis sets DZVP-MOLOPT[53] to expand the wave functions and plane wave sets up to a cut-off energy of 700 Ry to expand the electron density. $E_{\text{binding}} = E_{(\text{network, sub})} - 2E_{(\text{isolated, sub})} - 3E_{(\text{metal, sub})}$, where $E_{(\text{network, sub})}$ is the total energy of the network on the substrate (sub). $E_{(\text{isolated, sub})}$ is the total energy of the isolated molecule on the substrate, and $E_{(\text{metal, sub})}$ is the total energy of the adatom on the substrate. To compare their binding energies, we use a rhombic unit cell, comprising two molecules and three metal adatoms for both networks. This calculation work is done in cooperation with Ari Paavo Seitsonen.

In Chapter 5, the atomic-scale materials simulations in this study were done in the DFT framework by using VASP.[41, 54-58] Electron-ion interactions were taken into account with the Projector-augmented wave [42] potentials with a 500 eV kinetic cut-off energy. The electron-electron interactions were included by using PBE functionals[50] with Generalized Gradient Approximation. van der Waals interactions were described at the DFT-D2 level.[59] The Ag (111) substrate was represented by a four-layered 4×9 supercell with. The vacuum gap between two consecutive slabs in the z-direction is 21Å. The convergence limits for the total energy and the Hellman-Feynman forces during the structural relaxation were set to 10^{-5} eV and 0.01 eVÅ^{-1}, respectively. The Brillouin Zone was sampled according to the Monkhorst-Pack method[60] using a Γ-centered 3×2×1 k-point mesh. The Methfessel-Paxton smearing was employed with a smearing width of 0.2 eV. The adsorption energy of the considered models was calculated according to the following equation:

$$E_{\text{Ads}} = E_{(\text{molecule+substrate})} - [E_{(\text{molecule})} + E_{(\text{substrate})}] \quad (2.14)$$

where $E_{(\text{molecule+substrate})}$, $E_{(\text{molecule})}$, $E_{(\text{substrate})}$ are the total energy values (per cell) of molecule adsorbed substrate, bare substrate, and isolated molecules, respectively. Net charges on atoms were calculated by using the Bader analysis method.[61] The total charge transfer values were calculated according to the following equation:

$$\Delta\rho = \rho_{(\text{molecule+substrate})} - [\rho_{(\text{molecule})} + \rho_{(\text{substrate})}] \quad (2.15)$$

where $\rho_{(x)}$ values are the total charges on the corresponding structures. VESTA software

was used to visualize the 3D geometries and charge transfer data.[62] Theoretical STM plots were generated by applying the Tersoff and Hamann theory via the STMpw code. This calculation work is done in cooperation with Çağil Kaderoğlu and Ethem Aktürk.

2.4.6 Artificial intelligence

The Artificial intelligence tool "DeepSeek-V3" was employed for assisting with grammatical refinement and textual polishing.

3. Substrate-Dependent Reactivity of Aromatic Amines under O_2 Exposure on Metal Surfaces

Aromatic amines are widely used in manufacturing industries, where their oxidation plays a crucial role in direct applications and in the synthesis of nitrogen-containing compounds. Understanding their reactivity is a prerequisite for their use in various fields. While direct dehydrogenation of amino groups in aromatic amines has been realized on copper surfaces through thermal activation, their reactivity on relatively inert substrates remains limited and less understood. Herein, we combine scanning tunneling microscopy and X-ray photoelectron spectroscopy to explore the reactivity of aromatic amines on silver and gold surfaces using a gas-mediated reaction strategy. Our results reveal that oxidative dehydrogenation is readily achieved after O_2-mediated treatment on silver surfaces, leading to formation of organometallic nanopores, while aromatic amines remain unperturbed on Au(111), indicating a substrate-dependent behavior. Density functional theory calculations corroborate the experimental observations, by simulated core-level shifts and microscopy images, and demonstrate how the choice of substrate dictates the thermodynamics of the overall reactions. These findings emphasize the importance of substrate selection in modulating the surface chemistry of aromatic amines, paving the way for more efficient catalytic processes and material design.

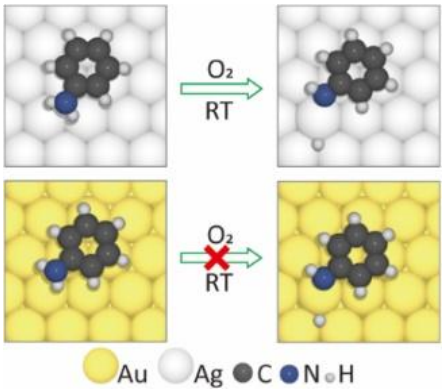

3. Substrate-Dependent Reactivity of Aromatic Amines under O2 Exposure on Metal Surfaces

Introduction

Aromatic amines (AAs), known for their chemical versatility, are widely used as key raw materials in manufacturing of industrial products and intermediates, including pharmaceuticals, rubber chemicals, dyes and pesticides.[63, 64] On-surface synthesis (OSS) has emerged as an appealing strategy for fabricating functional low-dimensional organic materials in the past two decades, with the support of advanced surface techniques such as scanning tunneling microscopy (STM).[65, 66] A range of molecular precursors have been used as building blocks for the construction of two-dimensional (2D) polymers, 2D organometallic networks etc.[67, 68] While molecular cores are expected to be the relevant functional units, the linkers derived from reactive functional groups become essential ties in construction of various nanoarchitectures. Thus, understanding the chemical reactivity of precursors with functional groups is crucial to OSS.[69] For instance, aryl halides have often been employed in the synthesis of graphene nanoribbons,[70] surface covalent polymers[71] and organometallic networks[72] via Ullmann coupling. Aromatic alkyne derivatives are used in fabrication of graphdiyne[73, 74] enyne[75] polycyclic hydrocarbons[76, 77] and 2D organometallic networks[21, 78] via homo-coupling, cycloaddition and dehydrogenation reactions.

Given their chemical diversity and significance, the behavior of AAs on surfaces is of considerable interest for potential applications in 2D organic functional framework preparation.[79-81] Among them, Schiff-base condensation reactions of AAs and aldehyde have been demonstrated on multiple surfaces.[82-85] Amides and imides were also obtained via reactions between amines and carboxylic acid derivatives and acyl chlorides on metal surfaces.[86-88] In addition to these cross-coupling reactions, AAs have also been studied in the formation of organometallic networks on Cu substrates through direct dehydrogenation.[89-92] However, AAs exhibit no reactivity on important inert surfaces such as Au(110)[93] and Ag(111)[94]. This highlights the necessity to systematically investigate the substrate-dependent reactivity of AAs by comparative assessment.

Apart from conventional thermal-activation methods, such as post-annealing, the OSS toolbox has been enriched to include photopocatalysis,[95-97] probe-inducing[98-100] and gas-mediation strategies. In particular, gas-mediation has been widely adopted to facilitate OSS due to the ingenious operation of gases, such as CO_2,[101] H_2,[102-104] CO[105] and O_2[78, 106]. For instance, Zhang et al.[21] employed O_2 to promote the deprotonation of terminal alkynes, enabling the formation of large-scale organometallic networks on Ag(111). Ji et al.[107] realized the transformation of 1D organometallic chains into 2D

networks on Cu(111) under O2 atmosphere.

In this work, we systematically investigate the reactivity of AAs on relatively inert metal substrates, focusing on the effects of crystal plane orientation and intrinsic substrate activity. By introducing O_2, we effectively activate the dehydrogenation reaction of 4,4″-diamino-p-terphenyl (DATP) molecules. Through comprehensive characterizations using scanning tunneling microscopy (STM) and X-ray photoelectron spectroscopy (XPS), we observe that DATP molecules undergo oxidative dehydrogenation and form uniform organometallic nanopores on the Ag(111) and Ag(100) surfaces while such reactions do not occur on Au(111). Density functional theory (DFT) calculations reveal that the reaction energy barriers were significantly lowered by the easier adsorption of O_2 on Ag(111) and Ag(100), as compared to Au(111). This study presents an efficient method to promote the reactivity of AAs on relatively inert surfaces under gentle conditions and elucidates the underlying mechanisms of oxidative dehydro-genation reactions of amines. These findings broaden the vision for applications of AAs in the synthesis of low-dimensional organic materials *via* OSS.

Results and discussion

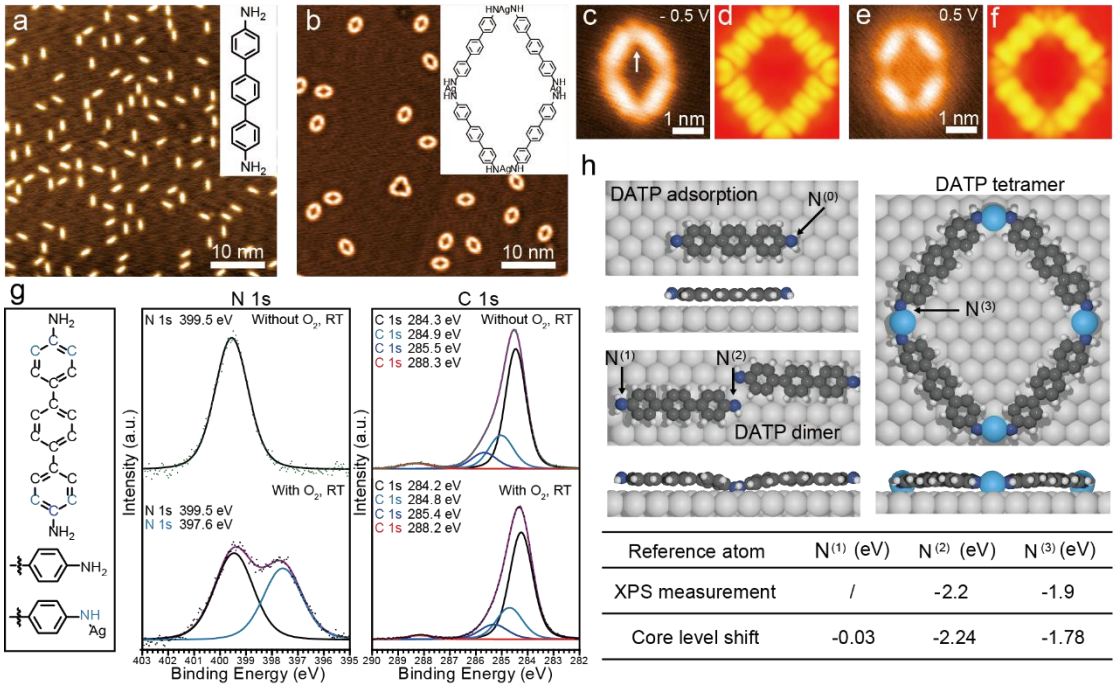

Figure 3.1: O_2-mediated dehydrogenation reactions of DATP on Ag(111) surfaces. (a) and (b) STM images of DATP deposited on Ag(111) at RT: (a) after deposition, (b)

following exposure in an O_2 atmosphere. The insets in (a) and (b) show the chemical structures of DATP monomer and tetramer. (c) and (e) STM images of the DATP tetramer nanopores structure, measured at a bias of - 0.5 V and 0.5 V, respectively. (d) and (f) DFT simulated STM images corresponding to (c) and (e). (g) XP core-level spectra of the N 1s and C 1s lines measured after DATP deposition at RT (top) and O_2 exposure at RT (bottom). (h) Optimized adsorption configurations of an individual DATP molecule, a DATP dimer and a tetramer structure on the Ag(111) surface, and the calculated core-level shifts of N 1s in different chemical environments with the chemical shift calculated as $E_{CLS} = E_{CL[N^{(m)}]} - E_{CL[N^{(0)}]}$. Scanning parameters: V_b = -1 V, I_t = 100 pA for (a); V_b = - 500 mV, I_t = 1 nA for (b); V_b = -500 mV, I_t = 1 nA for (c); V_b = 500 mV, I_t = 1 nA for (e); Data obtained at 4.5 K.

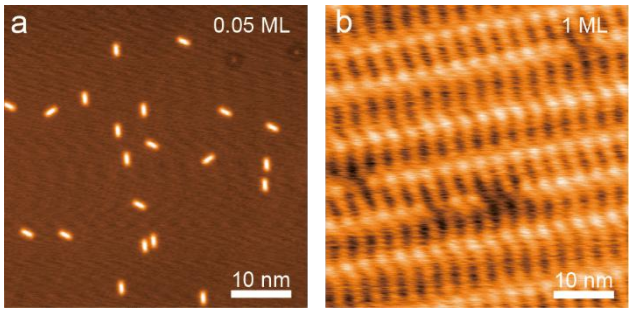

Figure 3.2: STM images for low-coverage (a) and high-coverage (b) depositions of DATP on Ag(111). Scanning parameters: V_b = -1 V, I_t = 100 pA for (a); V_b = -100 mV, I_t = 20 pA for (b).

DATP molecules were initially deposited on a Ag(111) surface at 300 K with a coverage of 0.1 monolayer (ML) (Figure 3.1a). At this low coverage, DATP monomers are randomly distributed on the surface, presumably due to substrate-mediated repulsive interactions.[108] Only upon increasing the coverage to a full monolayer (1 ML), a close-packed self-assembly pattern evolved (see Figure 3.2). Following exposure of the sample in Figure 3.1a to O_2 atmosphere (300 L; 1 L = 1.33×10^{-6} mbar • sec) at 300 K, discrete cyclic open arrangements emerge, mostly exhibiting a rhombic shape (Figure 3.1b). This newly formed structure, identified as a DATP tetramer (with its chemical structure shown as an inset in Figure 3.1b), is stabilized by imine-Ag-imine (NH-Ag-NH) linkages. It results from the oxidative dehydrogenation-upon O_2 treatment of amino groups, which subsequently bond with intrinsic Ag adatoms on the substrate. STM images of an individual DATP tetramer display distinct appearance at negative and positive bias voltages. At -0.5 V, the NH-Ag-NH linkage (pointed by a white arrow in Figure 3.1c) displays brightness similar to that of aromatic benzene rings,

while at 0.5 V, it becomes dimmer compared to the adjacent phenyl rings. These features are consistent with our dedicated DFT simulations (Figure 3.1d, f) and corroborate the proposed organometallic origin for the DATP tetramer.

XPS measurements were conducted to gain further chemical insight into the dehydrogenation reaction of AAs. Figure 3.1g presents XP spectra for the core-level of N 1s and C 1s of DATP deposited on the Ag(111) surface at RT before (top) and after O_2 treatment (bottom). The chemical structure on the left highlights the inequivalent carbon and nitrogen species with colors, according to their distinct chemical environments. Following the deposition of DATP molecules on Ag(111) with coverage of ~1 ML, we investigate the sample without O_2 treatment. The N 1s spectra exhibit a single peak centered at a binding energy of 399.5 eV, associated with the amino nitrogen, indicating that amino groups remain intact at RT. In the C 1s spectrum, two distinct features are observed at binding energies of 284.8 eV and 288.3 eV. Closer inspection of the former reveals three components at 284.3 eV, 284.9 eV and 285.5 eV, respectively; They represent contributions from the carbon atoms in the different chemical environments shown in Figure 3.1g. The signal at the binding energy of 288.3 eV is attributed to carbon contamination in the chamber. After O_2 exposition of the sample at RT, the peaks in C 1s spectra slightly shift to 284.2 eV, 284.8 eV, 285.40 eV and 288.2 eV from lower to higher binding energies. This indicates that the chemical environment of the carbon atoms in the molecule remains largely unchanged. As to the N 1s spectrum, the previously observed single peak of 399.5 eV becomes much broader, with a new component appearing at the binding energy of 397.6 eV. The peak fitting reveals that the intensity of the peak at 399.5 eV is pronounced reduced, whereas the new peak at 397.6 eV significantly contributes to the overall N 1s signal. This energy shift by 1.9 eV to lower binding energy is associated with the chemical transformation from -NH2 to -NH, leading to the formation of NH-Ag-NH linkages.[89, 109, 110] Quantitative analysis suggests that the total intensity of these peaks is comparable to that of the single peak before O_2 treatment. This result indicates that almost half of the amino groups undergo dehydrogenation reactions, confirming the oxygen assisted dehydrogenation of amino groups. The remaining intrinsic amino signal is ascribed to excess DATP from the deposition in these experiments.

DFT calculations were performed to identify the chemical states of carbon and nitrogen atoms in different chemical environments. As shown in Figure 3.1h, the adsorbed DATP on Au(111), the dehydrogenated DATP dimer, and the organometallic tetramer are simulated models of experimental products of depositing DATP on Ag(111), O_2 exposure at 200 K, O_2 exposure at RT, respectively. The calculated core-

level shifts of the nitrogen atoms under these conditions are consistent with our experimental results, with values of -2.24 eV vs -2.2 eV and -1.78 eV vs -1.9 eV. These results substantiate the proposed organo-metallic structure with NH-Ag-NH linkages.

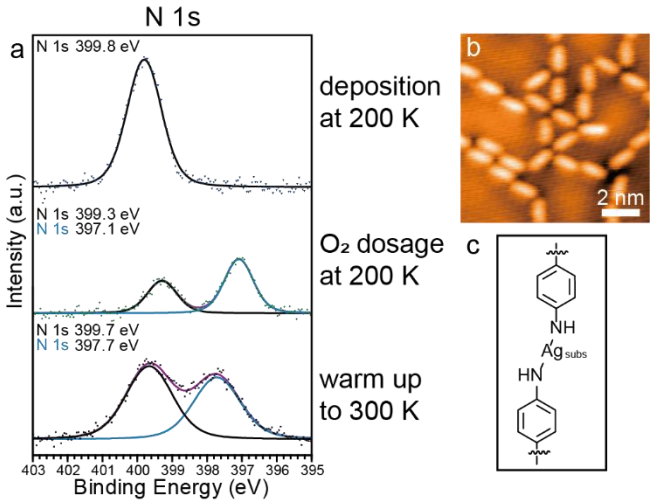

Figure 3.3: (a) XP spectra of N 1s for DATP deposition on the Ag(111) surface at 200 K (top), followed by O_2 treatment at 200 K (middle) and annealing to 300 K (bottom). (b) shows the STM image for DATP organometallic chain structure after O_2 treatment at low temperature of 200 K, and the chemical structure for *NH-Ag$_{subs}$-NH* linkage is given in (c). Scanning parameters: V_b = 100 mV, I_t = 1 nA for (b)

To further explore the O_2-mediation strategy in enhancing the reactivity of amines, we introduce O_2 to the DATP adsorbed Ag(111) surface at a low temperature of 200 K. This experiment demonstrated that the dehydrogenation reaction of amino groups facilitated by O_2 is achievable even at a substrate temperature of 200 K (Figure 3.3a). The -NH signal of nitrogen atoms after dehydrogenation is observed in the N 1s spectra, however, the Ag atoms are not visible in the STM image (Figure 3.3b, c). This indicates that the dehydrogenated -NH moiety is anchoring at the surface atomic lattice,[21] which would cause them to appear as a dimmer feature between two molecules. In addition, we investigated the chemical states of DATP molecules on Ag(111) without O_2 exposure in a procedure of progressive increase of annealing temperatures (Figure 3.4). STM imaging of the sample after annealing at 525 K shows that most DATP molecules remain as monomers and are dispersed individually on the surface (Figure 3.4a, b), within very scarce trimers. The proposed chemical structure is drawn in Figure 3.4c, which also reveals the chirality of the trimer. Despite some desorption of molecules, XPS measurements show that the characteristic signal of the -NH2 group in N 1s and

the different C components in the C 1s spectra remain constant at the investigated annealing temperatures up to 525 K (Figure 3.4d), which implies that the post-annealing hardly activated the amino species on the Ag(111) surface (partial dehydrogenation becomes visible at 475 K / 525 K in the N 1s spectrum in form of a shoulder centered at 398.2 eV). These investigations reveal that almost all DATP molecules did not undergo chemical reactions, further supporting the critical role of the O_2-exposure strategy in facilitating dehydrogenation reactions.

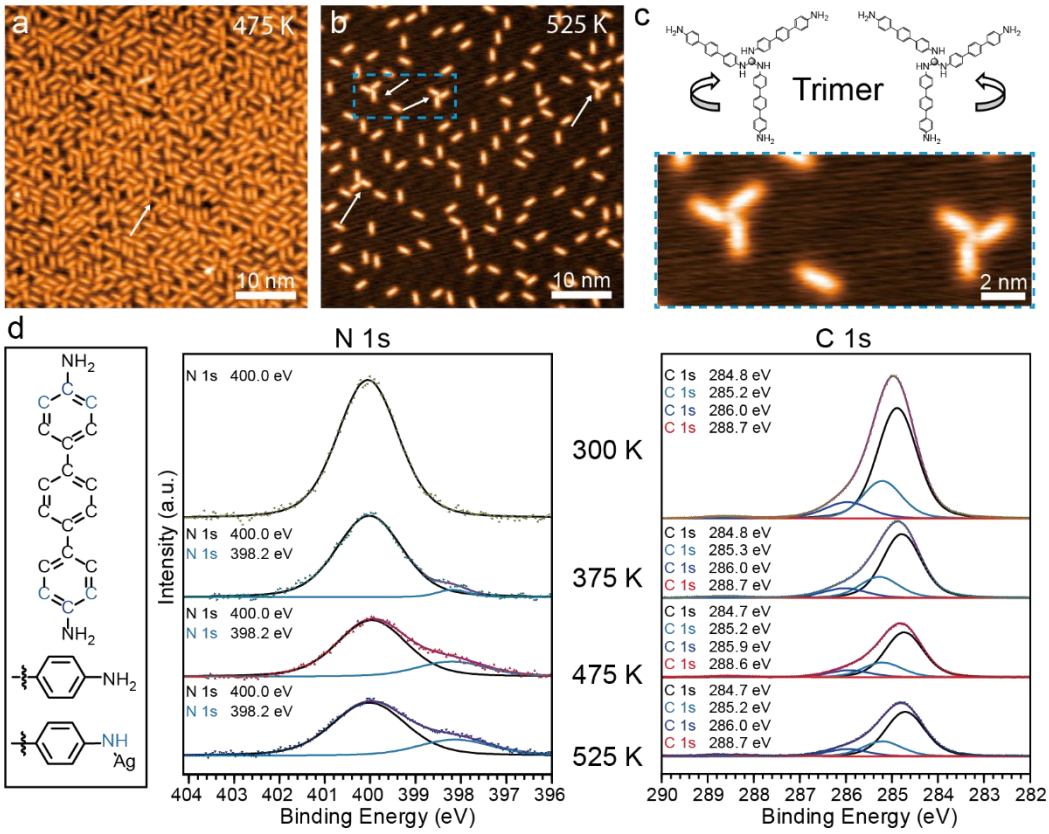

Figure 3.4: STM images depict DATP deposition on Ag(111) followed by annealing at 475 K (a) and 525 K (b). (c) presents the zoom-in STM images for DATP-Ag trimer (pointed by white arrows) in and proposed chemical structure. (d) shows the corresponding XP spectrum for N 1s and C 1s of DATP deposition on Ag(111) and followed by step annealing. Scanning parameters: V_b = -100 mV, I_t = 1 nA for (a); V_b = -1 V, I_t = 100 pA for (b).

To explore the wider applicability of the O_2-mediation strategy, we performed experiments using Ag(100). Without the O_2 treatment, there is dehydrogenation of adsorbed DATP up to 525 K, as evidenced by STM observations (Figure 3.5a, b). This behavior is consistent with the results observed on the Ag(111). While the Ag(100) surface is generally more reactive than Ag(111) due to its open structure, its catalytic effect was insufficient for inducing chemical reactions of DATP molecules. However, upon

O_2-dosing to the DATP/Ag(100) at RT, nanoporous networks with a square unit cell evolve (Figure 3.6a). The high-resolution STM image in Figure 3.6b demonstrates that these are composed of DATP molecules connected through N-Ag linkages, as exemplified by the chemical structure in Figure 3.6c. These observations indicate that O_2-mediation facilitates dehydrogenation reactions of DATP also on Ag(100).

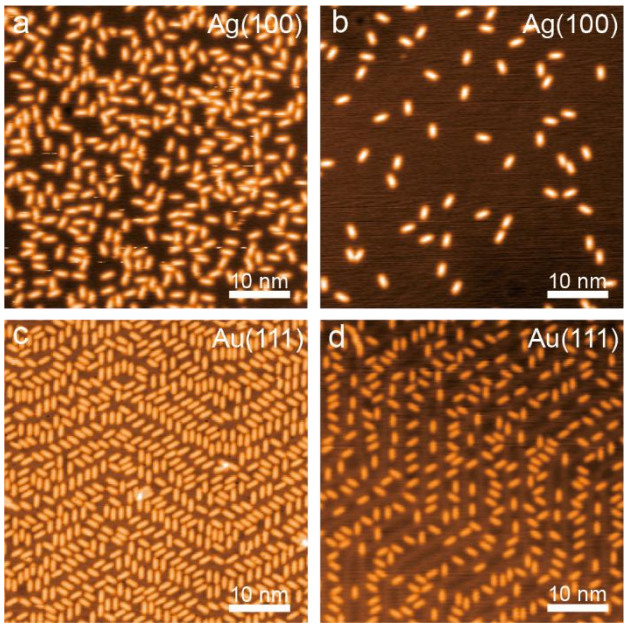

Figure 3.5: STM images for (a) DATP deposition on Ag(100) at 260 K and (b) post-annealed at 525 K along with desorption. (c) DATP deposition on Au(111) at 300 K and (d) post annealed at 575 K. Scanning parameters: V_b = -300 mV, I_t = 20 pA for (a); V_b = -100 mV, I_t = 100 pA for (b); V_b = -1 V, I_t = 100 pA for (c); V_b = -1 V, I_t = 100 pA for (d).

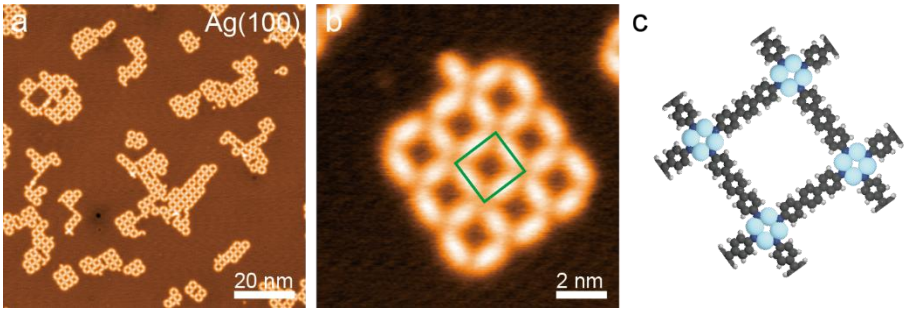

Figure 3.6: O_2-mediated dehydrogenation reactions of DATP on Ag(100) surfaces. Large-area (a) and high-resolution (b) STM images of DATP molecules on Ag(100) surfaces after O_2 treatment. STM images of O_2 exposed DATP/Ag(100) after the deposition of DATP molecules on the Ag(100) surface kept at RT. (c) Chemical structure of the proposed organometallic structure connected by N-Ag-N linkages,

corresponding to an outlined pore in (b). Scanning parameters: V_b = -1 V, I_t = 100 pA for (a); V_b = -500 mV, I_t = 100 pA for (b). Data obtained at 4.5K. C, N, H, and Ag atoms are represented by black, blue, white, and pale blue spheres, respectively.

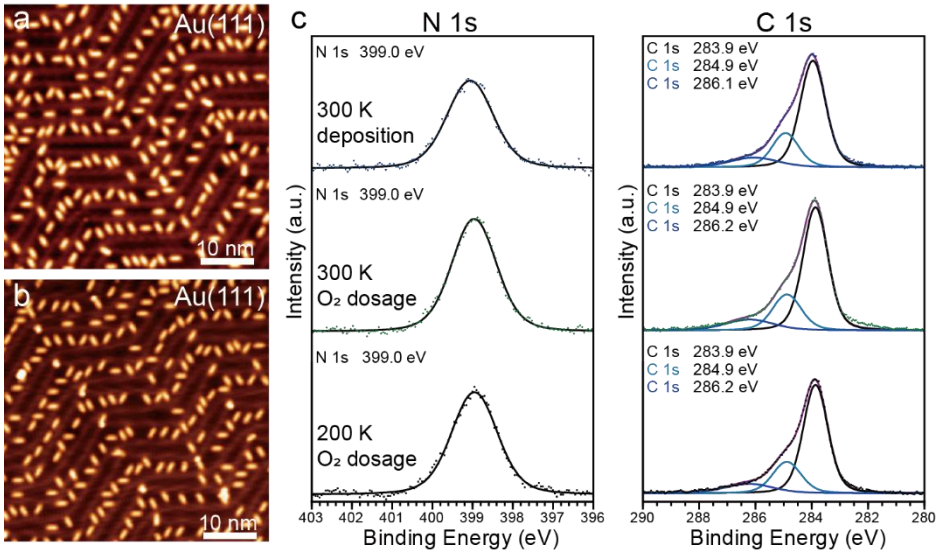

Figure 3.7: O_2 treatment of DATP on Au(111) surfaces. (a) STM images for DATP deposition on the Au(111) surface at room temperature. (b) STM images of DATP on Au(111) after exposure in O_2 atmosphere. (c) XP core-level spectra of the N 1s and C 1s lines for DATP deposition on Au(111) at RT (top) and O_2 treatment at 300 K (middle) and 200 K (bottom). Scanning parameters: V_b = -500 mV, I_t =50 pA for (a); V_b = -1 V, I_t = 100 pA for (b). Data recorded at 4.5 K.

For comparison, we investigated the O_2-mediation with DATP adsorbed on Au(111). DATP molecules were deposited at 300 K and subsequently annealed at 575 K (Figure 3.5c, d). Analogous to the observations on Ag(111) and Ag(100) surfaces, DATP molecules retain initially their structural integrity (Figure 3.5c and Figure 3.7a). Intriguingly, also following O_2 treatment, DATP molecules are preserved as intact monomers (Figure 3.7b), in contrast to the observations on Ag(111) and Ag(100). XPS measurements were performed to assess the chemical state of DATP (as shown in Figure 3.7c). Core-level spectra of N 1s and C 1s presented no changes under three conditions: after DATP deposition on Au(111) at 300 K (top), following O_2 treatment at 300 K (middle), and after DATP deposition on Au(111) at 200 K (bottom). The same XPS features confirm the STM observations with unperturbed DATP species on Au(111).

To understand the differing effects of O_2-mediation on the reaction of DATP on Ag

and Au surfaces, we study the reaction pathways on both substrates with DFT calculations. As shown in Figure 3.8a-c, the dehydrogenation of amino under influence of dioxygen is endothermic on both Ag(111) and Au(111) with potential energy barriers of 0.25 eV and 0.35 eV, respectively. Notably, the low energy barrier on Au(111) indicates that AAs could, in principle, be principally activated by O_2. However, this cannot be reconciled with our experimental observations, where no reactions occurred following DATP exposure to O_2 even at 300 K.

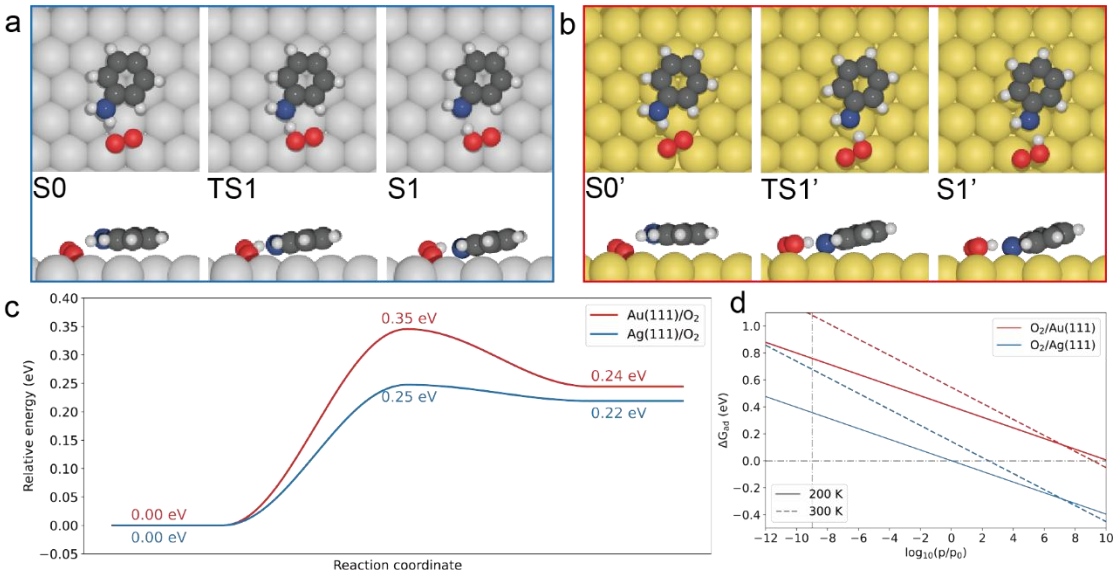

Figure 3.8: DFT calculations of reaction pathways and adsorption behavior. O_2 induced dehydrogenation of DATP on (a) Ag(111) and (b) Au(111), with corresponding energy profiles (c). (d) Adsorption free energy change for molecular adsorption of O_2 on Ag(111) and Au(111) as a function of O_2 pressure at 200 K and 300 K. C, N, H, O, Ag, and Au atoms are represented by black, blue, gray, red, white, and yellow spheres, respectively.

This apparent discrepancy can be attributed to the adsorption behavior of O_2. At 0 K, O_2 adsorption on Ag(111) is exothermic with an adsorption energy of -0.35 eV, whereas it is less favored on Au(111) with an adsorption energy of -0.16 eV (negative values indicate energetically favorable adsorption, see definitions in SI). However, these adsorption energies do not account for temperature and pressure effects. To address this, we calculate the adsorption free energy (ΔG_{ad}) of O_2 under experimental conditions (Figure 3.8d). At the low pressure of our experiments (~10^{-6} mbar during O_2 exposure), the O_2 adsorption is endergonic for both surfaces, but is distinctly more favorable on Ag(111) than Au(111). For instance, at 200 K and a pressure of 10^{-6} mbar,

the adsorption free energy of O_2 on Ag(111) is calculated as 0.27 eV, significantly lower than the 0.46 eV on Au(111).

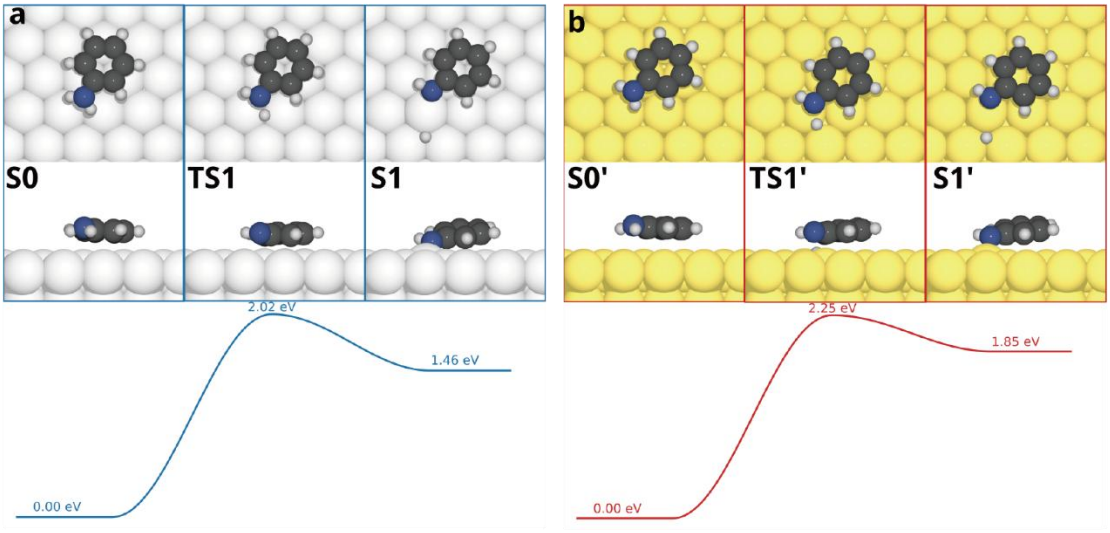

Figure 3.9: DFT calculation dehydrogenation pathways of DATP on Ag(111) (a) and Au(111) (b) along with energy profile. The C, N, H, Ag, and Au atoms are represented by the black, blue, gray, white, and yellow spheres, respectively.

When these adsorption free energies are considered, the effective barrier for surface attachment, with respect to gas phase O_2, amounts to 0.52 eV on Ag(111) and 0.81 eV on Au(111) (at 200 K and 10^{-6} mbar). The Boltzmann factor of the reaction between the two surfaces is 1.4×10^7, explaining why the reaction occurs on Ag(111) but not on Au(111). Notably, increasing the temperature does not facilitate oxidative dehydrogenation on Au(111) as it further increases the endergonicity of O_2 adsorption and shifts the activation energy to higher values. Without the assistance of O_2, the activation energies for dehydrogenation are significantly higher: 2.02 eV and 2.25 eV, on Ag(111) and Au(111), respectively (Figure 3.9). These results emphasize the critical role of O_2 in lowering the activation energy and facilitating dehydrogenation.

Conclusion

In conclusion, the O_2-mediated treatment effectively induces the oxidative dehydrogenation of amino groups in aromatic amines, resulting in the formation of organometallic nanopore structures on Ag(111) and Ag(100) surfaces, while the process is hindered on Au(111). Systematic STM and XPS experiments, combined with complementary DFT calculations, reveal that the O_2-treatment significantly enhances the

reactivity of aromatic amines by lowering the energy barrier compared to activation in absence of O_2. Our finding identifies that the chemisorption of O_2 is the ratelimiting step in the dehydrogenation reaction, which is thermodynamically much less favorable on Au(111) than on Ag(111). These studies unveil the synergistic catalytic role of metal substrates and oxygen in the oxidative dehydrogenation of amines, providing valuable insights into their surface chemistry and a promising strategy for on-surface synthesis of functional low-dimensional organic materials on metal surfaces.

4. Transmetalation in Surface-Confined Single-Layer Organometallic Networks with Alkynyl-Metal-Alkynyl Linkages

---

This Chapter includes content that has been published in

Wenchao Zhao, Felix Haag, Ignacio Piquero-Zulaica, Zakaria M. Abd El-Fattah, Prashanth Pendem, Pablo Vezzoni Vicente, Yi-Qi Zhang, Nan Cao, Ari Paavo Seitsonen, Francesco Allegretti, Biao Yang, Johannes V. Barth, **Transmetalation in Surface-Confined Single-Layer Organometallic Networks with Alkynyl-Metal-Alkynyl Linkages,** ACS Nano, 2024, 18, 20157-20166. Copyright 2024 American Chemical Society.

STM measurements were performed by *Wenchao Zhao* and *Biao Yang*

LEED and XPS measurements were performed by *Felix Haag*, *Pablo Vezzoni Vicente* and *Francesco Allegretti, more details regarding to the LEED and XPS results could be found in Felix Haag's and Pablo Vezzoni Vicente's thesis.*

DFT calculations were performed by *Ari Paavo Seitsonen*

Transmetalation represents an appealing strategy towards fabricating and tuning of functional metal-organic polymers and frameworks for diverse applications. In particular, building two-dimensional (2D) metal-organic and organometallic networks affords versatile nanoarchitectures of potential interest for nanodevices and quantum technology. The controlled replacement of embedded metal centers holds promise for exploring new material varieties by serial modification and different functionalization. Herein, we introduce a protocol for the modification of a single-layer carbon-metal based organometallic network via transmetalation. By integrating external Cu atoms into the alkynyl-Ag organometallic network constructed with 1,3,5-triethynylbenzene (TEB) precursors, we successfully realized in situ its highly regular alkynyl-Cu counterpart on the Ag(111) surface. While maintaining a similar lattice periodicity and pore morphology as the original alkynyl-Ag sheet, the Cu-based network exhibits increased thermal stability, guaranteeing improved robustness for practical

implementation.

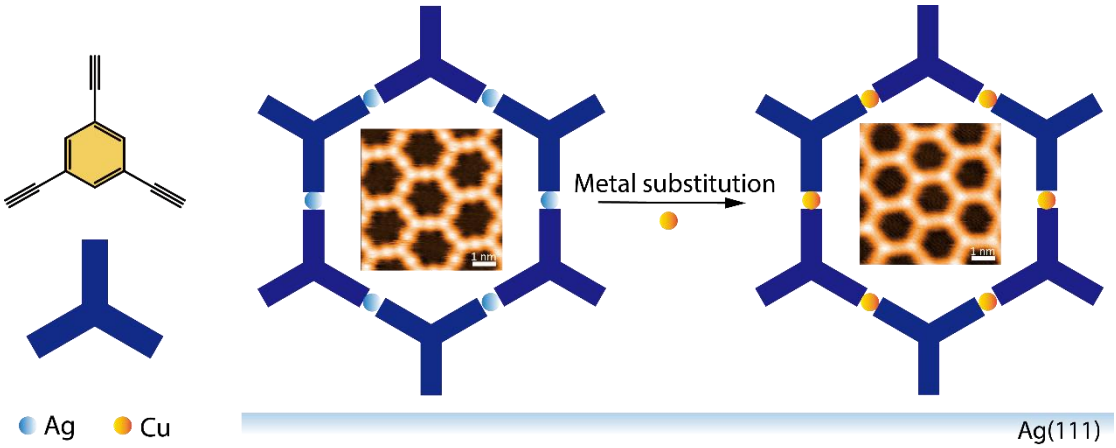

Introduction

In recent years, the systematic development of 2D molecule-based materials has become the focus of intense research owing to their unique physical and chemical properties.[111, 112] Supramolecular self-assembly and coordination engineering with organic molecules on surfaces represent powerful bottom-up strategies for the efficient construction of 2D molecular materials suitable for catalysis, magnetism, semiconducting electronic devices and so forth,[111, 113-117] which can be for instance tailored to incorporate functional magnetic metal centers,[118] such as Co,[119, 120] Ho,[121] Dy,[122] etc. A major challenge in this field is to increase the system stability by designing 2D materials via covalent on-surface synthesis. Covalent linkages are advantageous because they can afford single-layer organic structures with delocalized electronic conduction and excellent robustness.[67, 95, 123] The on-surface synthesis of 2D covalent nano-architectures is typically performed in vacuum on atomically well-defined metal surfaces.[68, 124, 125] However, this approach commonly faces the problem of limited extension of the ordered domains[126-128] due to the occurrence of undesired reaction channels and the irreversibility of the covalent bond formation in vacuum, which prevents the healing of defects.[66]

Organometallic bonding, mostly involving carbon-metal linkages, due to its generally covalent nature[20] and the reversibility associated with the binding characteristics,[19] may provide a powerful strategy for engineering surface-confined organic networks with appreciable robustness as well as impressive mesoscale regularity.[21, 129] 2D organometallic networks (OMNs) feature functional 2D materials with significant promise. The often higher flexibility relative to purely covalent linking, and the reversibility during the formation process in the low-dimensional environment

of a surface offers the possibility of self-healing of defects, potentially affording higher order and tailored packing motifs and symmetry. Although various organometallic networks have been constructed with selected molecular building blocks via consuming surface adatoms provided by the substrate underneath, the success rate for their realization is often unforeseeable and strongly substrate-dependent, limiting the general applicability of such functional organometallic materials. In particular, it has recently been shown that extended graphdiyne-like, alkynyl-silver-alkynyl and alkynyl-gold-alkynyl honeycomb OMNs can be prepared successfully by applying on-surface synthesis strategies.[21, 129-132] Yet, the large spectrum of metal centers and possible organic linkers call for the identification of efficient routes to bestow the desired variety and versatility to the structural and electronic properties of such films.

Recently, there has been considerable interest in synthesizing, modifying, or functionalizing metal-organic frameworks (MOFs) by transmetalation via solution chemistry, with the aim to tailor their structures and performances for various applications.[133-135] For instance, Li. J et al. utilized transmetalation methods to for the synthesis of an isomer MOF enhancing the catalysis performances.[136] In-vacuum surface-adsorbed macrocycles, e.g., metalloporphyrins, have been reported to undergo transmetalation, facilitating the creation of macrocycles and the tuning of their properties for heterogenous catalysis.[137-139] Accordingly, in the context of surface-supported 2D OMNs, transmetalation appears as an appealing route for customizing the structure-property relationship of such attractive 2D materials in a controlled way. Surprisingly, this option has been rarely studied within the field of metallosupramolecular surface networks, with the exception of a nitrogen-metal linked 2D conjugated system.[18] In particular, successful post-synthetic transformation of surface-confined 2D-OMNs with carbon-metal bonding, bearing significant prospects for appealing 2D graphyne- or graphdiyne-like materials with interesting electronic properties has not been reported so far.

Herein, combining a suite of surface science techniques, including scanning tunneling microscopy (STM), low-energy electron diffraction (LEED), and X-ray photoelectron spectroscopy (XPS), as well as density functional theory (DFT) calculations, we address the deliberate modification of single-layer OMNs from an alkynyl-Ag-alkynyl to an alkynyl-Cu-alkynyl linking platform via post-synthetic transmetalation. Using a simple TEB precursor, extended organometallic honeycomb Ag-TEB networks are first synthesized on a Ag(111) surface under ultrahigh vacuum (UHV) conditions, by means of a previously reported gas-mediated surface reaction protocol.[21] The subsequent deposition of Cu adatoms followed by thermal annealing to

appropriate temperatures triggers the transformation of Ag-TEB to Cu-TEB OMN (Scheme 4.1). The latter 2D OMN, being not directly achievable on a Cu(111) substrate, possesses higher thermal stability, while retaining a similar lattice periodicity and pore symmetry as the original Ag-TEB. This finding provides a simple route to the engineering of a larger variety of single-layer robust carbon-based nanomaterials at well-defined conditions.

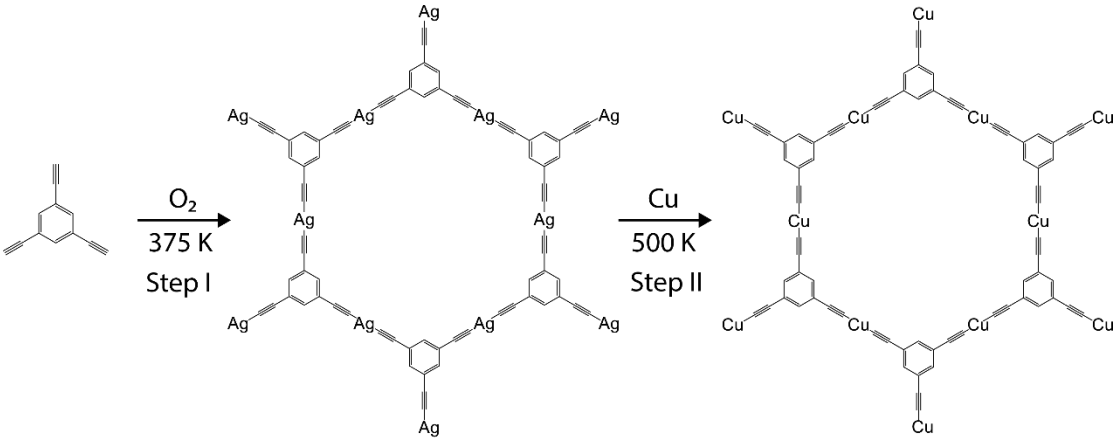

Scheme 4.1: Schematic of the Ag-TEB OMN preparation and its transformation into Cu-TEB OMN. Step I: Exposure to O_2 at 300 K and post-annealing at 375 K. Step II: Cu deposition at 300 K and post-annealing at 500 K.

Results and discussion

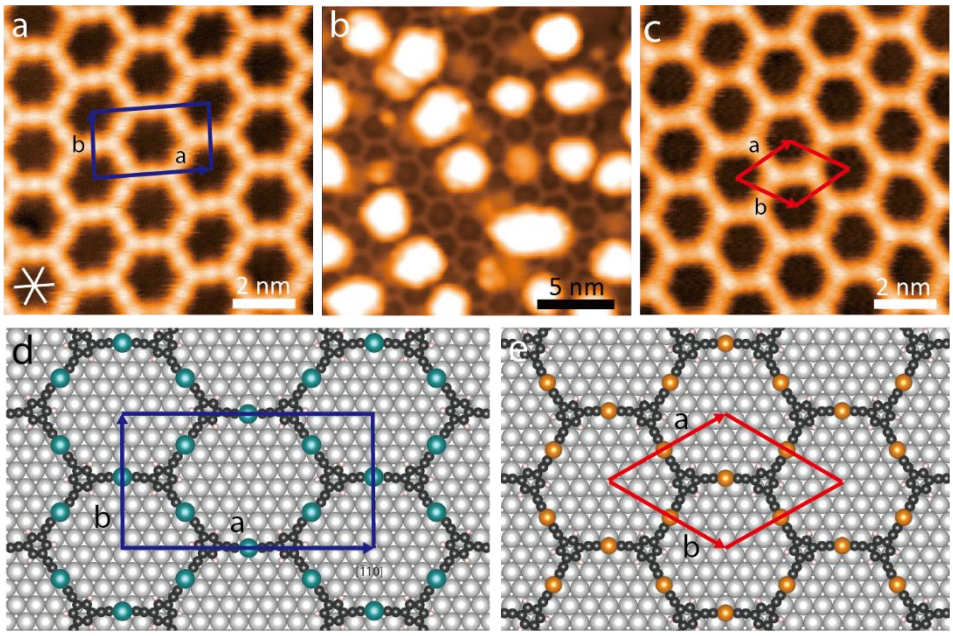

Figure 4.1: STM topography images of (a) Ag-TEB OMN formed after dosing O_2 on TEB organic assembly on Ag(111) at 300 K and annealing at 375 K, (b) Cu clusters on Ag-TEB OMN before post-annealing and (c) Cu-TEB OMN obtained by dosing Cu atoms on Ag-TEB OMN and then post-annealing to 500 K, inducing transmetalation. The surface unit cells are highlighted by blue and red frames, respectively. DFT simulated model of Ag-TEB OMN (d) and Cu-TEB OMN (e) on a silver slab (see method). The images in (a) and (c) were taken with tunneling parameters of V_b = -100 mV, I_t = 1 nA, while the image in (b) was scanned at V_b = 380 mV, I_t = 300 pA. The closed-packed crystallographic directions of the substrate are denoted as white lines in panel (a).

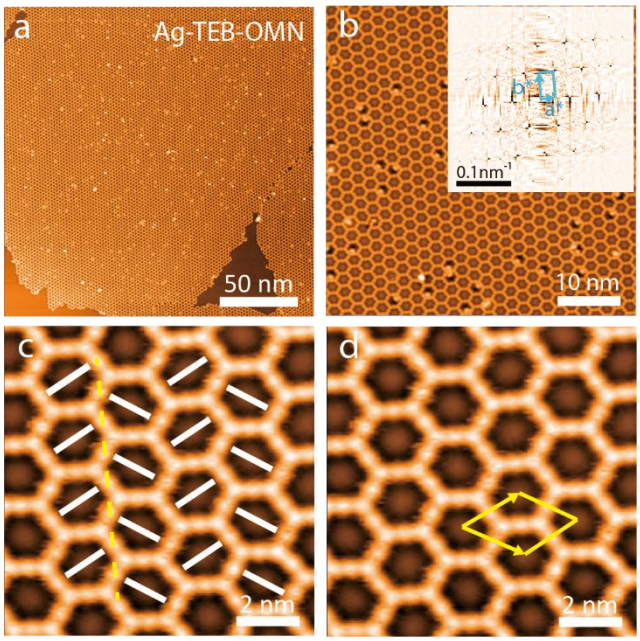

Figure 4.2: Large-area STM images of Ag-TEB OMN with 0.2 μm-size (a) and 50 nm-size (b); the inset presents the 2D-FFT of the 50 nm × 50 nm area shown in panel (b). Panel (c) emphasizes the glide symmetry of neighboring distorted hexagons. In panel (d) we outline a rhombic unit cell (in yellow) similar to the Cu-TEB network of Figure 4.1c, as a comparison to the rectangle unit cell assumed in Figure 4.1a. The tunneling parameters are V_b = -500 mV, I_t = 100 pA (a); V_b = 400 mV, I_t = 1 nA (b); and V_b = 350 mV, I_t = 300 pA (c) and (d).

Modification of Ag-TEB OMN by transmetalation protocol to fabricate Cu-TEB OMN. The self-assembly of the TEB precursor on Ag(111) was previously characterized by Kepčija et al[127]. Here, we initially exposed a TEB sub-monolayer assembly to O_2 (600 L; 1 L = 1.33×10^{-6} mbar • sec) at 300 K, followed by annealing at

375 K. This preparation strategy (summarized in Scheme 4.1, step I) was successfully used in reference[21] to create a highly regular OMN with alkynyl-Ag-alkynyl linkages, using the more extended, 1,3,5-tris(4-ethynylphenyl)benzene (referred to as Ext-TEB) precursor.

As illustrated in Figure 4.1a, an ordered, porous Ag-TEB OMN readily evolves. Moreover, Figure 4.2a, b show that the OMN grows into large domains extending up to the micrometer size, similarly to Ext-TEB on Ag(111)[21]. The blue frame in Figure 4.1a outlines the 2D centered unit cell of the Ag-TEB OMN, with lattice constant measured as a = 37.6 ± 0.2 Å, b = 20.7 ± 0.2 Å and an angle of $\gamma \approx 90.2^{o} \pm 1^{o}$. More precisely, the Ag-TEB OMN structure displays two adjacent columns of neighboring, distorted hexagonal motifs, corresponding to a p2gg plane group with glide symmetry (cf. Figure 4.2c), which is also similar to Ext-TEB[21]. This renders the description of the periodicity through a quasi-rectangle unit cell more precise than using a smaller quasi-hexagonal rhombic primitive cell (indicated in Figure 4.2d, yellow rhombus) with primitive vectors (a = b ≈ 21.5 Å and $\gamma \approx 57.7^{o}$) joining the centers of adjacent (but distorted) hexagonal pores. Moreover, the 2D fast Fourier transform (2D-FFT), inset of Figure 4.2b, of a neat large-area patch also shows rectangle-like unit cell. Panel b in Figure 4.1 characterizes the intermediate preparation step, after depositing Cu on Ag TEB OMN at 300 K. The bright appearing clusters are identified as agglomerates of Cu atoms adsorbed on top of the networks. After subsequently annealing this system at 500 K (Scheme 1, step II), a regular porous network with honeycomb symmetry and no superimposing clusters is restored, as illustrated in Figure 4.1c. The structure is similar to the original, pristine Ag-TEB OMN, however, it features differences in several details, whence we interpret the new network as Cu-TEB OMN formed by the establishment of alkynyl-Cu-alkynyl linkages (*vide infra*). The corresponding unit cell, depicted in Figure 4.1c, is marked by the red rhombus, whereby the lattice parameters are similar to each other in length, a = 20.1 ± 0.2 Å, b = 20.3 ± 0.2 Å, and the angle γ between unit cell vectors a and b amounts to $59.2^{o} \pm 1.0^{o}$. Consequently, the pores of Cu-TEB OMN come closer to the perfect hexagonal symmetry than Ag-TEB OMN, while exhibiting slightly smaller pore size.

To elucidate the origin of the slight structural and morphological differences, herein, we performed DFT calculation. Specifically, gas phase DFT optimization for unit cell representation of the alkynyl-Ag-alkynyl and alkynyl-Cu-alkynyl linkages, which reveals that the length of Ag-TEB is larger than for the Cu-TEB linkage, as shown in Figure 4.3a and 4.3e. Moreover, Figure 4.1d and 4.1e depict the DFT calculated structures for Ag-TEB and Cu-TEB OMN on Ag(111). The rectangular unit cell of Ag-

TEB OMN in Figure 4.1d was outline in blue, and the constants of the Ag-TEB model were a ≈ 37.6 Å and b ≈ 20.0 Å, which were close to experimental unit cell constants a = 37.6 ± 0.2 Å, b = 20.7 ± 0.2 Å. The rhombic unit cell of Cu-TEB OMN in Figure 4.1e was marked in red. The unit cell constants of the Cu-TEB model are a = b ≈ 20.0 Å, which are close to experimental results (a = 20.1 ± 0.2 Å, b = 20.3 ± 0.2 Å). While Cu-TEB OMN can place all Cu atoms and the benzene rings at hollow sites of the Ag(111) surface well, Ag-TEB OMN needs to be stretched along the $[\bar{1}10]$ direction due to the mismatch with the substrate. Besides, the binding energy for both OMNs were calculated (see method), the $E_{bind(Cu\text{-}TEB\ OMN)}$ = -6.90 eV being lower than $E_{bind(Ag\text{-}TEB\ OMN)}$ =-3.88 eV by about 3.0 eV, which in turn implies that the alkynyl-Cu-alkynyl linkage is significantly more stable than the alkynyl-Ag-alkynyl counterpart, and thus offers a possible driving force for the transmetalation from C-Ag-C to C-Cu-C connections, which is elucidated detailly below.

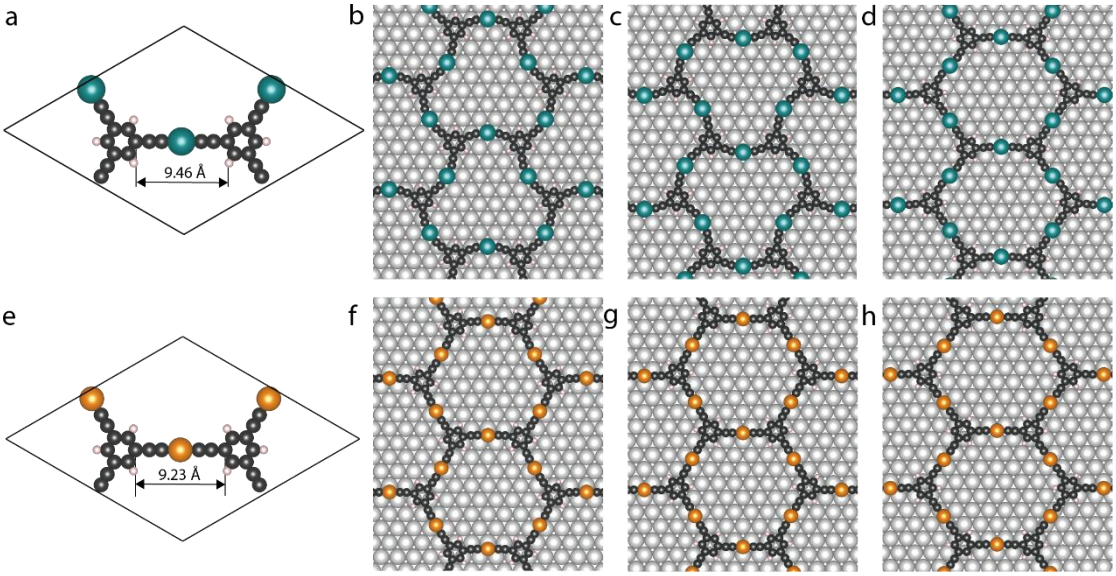

Figure 4.3: Gas phase optimized structure for unit cell representation of Ag-TEB (a). DFT simulated models of Ag-TEB OMN with possible hexagonal, rectangular-12 and rectangular-13 unit cells (b) (c) (d) on the Ag(111) surface. Gas phase optimized structure for unit cell representation of Cu-TEB (e), and DFT simulated models of Cu-TEB OMN with possible hexagonal, rectangular-12 and rectangular-13 unit cells (f) (g) (h) on the Ag(111) surface. In the OMNs, the silver, copper, carbon and hydrogen atoms are marked by green, orange, black and pink spheres, respectively.

Firstly, the gas phase DFT optimization for unit cell representation of the alkynyl-Ag-alkynyl and alkynyl-Cu-alkynyl linkage reveals that the length of Ag-TEB is longer than the Cu-TEB linkage, as shown in Figure 4.3a and 4.3e. Secondly, we proposed and

built calculated models as shown in Figure 4.3, with possible unit cells: hexagonal unit cells with vectors $4 \times \sqrt{3}$ in Figure 4.3c and 4.3g (rectangular-12) and rectangular unit cells with vectors $13 \times \sqrt{3}$ in Figure 4.3d and 4.3h (rectangular-13), to simulate both networks adsorbed on the Ag(111) substrate by DFT. The rectangular-12 is in principle the same as the hexagonal one with two unit cells of the hexagonal cell inserted into the rectangular cell. The rectangular-13 has one more row of Ag substrate to be extended. Additionally, the formation energy for all network modes was calculated per two molecules and three metal atoms. The Ag atoms are coded in green and the Cu atoms are marked in orange.

In the case of Ag-TEB OMN, Figure 4.3b-d reveal the calculated hexagonal, rectangular-12 and rectangular-13 models for Ag-TEB OMN with $E_{bind(Ag/hexagonal)}$ = -3.66 eV, $E_{bind(Ag/rectangular\text{-}12)}$ = -3.69 eV, and $E_{bind(Ag/rectangular\text{-}13)}$ = -3.88 eV, which implies rectangular-13 model the lower energy for Ag-TEB OMN and therein the most stable structure as shown in Figure 4.3d. Additionally, as shown in the hexagonal (Figure 4.3b) and the rectangle-12 (Figure 4.3c) structure, the Ag-TEB is fully distorted and doesn`t match our experimental topology images. Moreover, the lattice constants for Ag-TEB rectangular-13 model are a ≈ 37.6 Å and b ≈ 20.0 Å, which are also reasonably close to the average experimental results (a = 37.6 ± 0.2 Å; b = 20.7 ± 0.2 Å).

In the case of the Cu-TEB OMN model, the hexagonal, rectangular-12 and rectangular-13 models are presented in Figure 4.3f-h, respectively. The corresponding $E_{bind(Cu/hexagonal)}$ = -6.90 eV, $E_{bind(Cu/rectangular\text{-}12)}$ = -6.91 eV and $E_{bind(Cu/rectangular\text{-}13)}$ = -6.68 eV are found, which implies Figure 4.3f to be the most stable structure for Cu-TEB OMN. As we discussed before, hexagonal and rectangle-12 model are in principle similar, hence the formation energy for both are close, while also implies no distortions and nice matching between Cu-TEB OMN and Ag(111) substrate. The lattice constants for hexagonal one of Cu-TEB (Figure 4.3f-g) are a = b ≈ 20.0 Å, which are close to the average experimental results (a = 20.1 ± 0.2 Å, b = 20.3 ± 0.2 Å).

Comparing the rectangular-13 structure of Ag-TEB with the hexagonal one and rectangular-12 ones of Cu-TEB OMN, all the Cu atoms can be located at the hollow position (we show the case of hcp hollow sites for hexagonal one in Figure 4.3f, but fcc hollow sites for rectangular-12 in Figure 4.3g). Moreover, the benzene ring centers also seat at hollow positions. This reveals an excellent matching between the Cu-TEB OMN and the Ag(111) substrate. However, in the case of the Ag-TEB OMN (cf. Figure 4.3g) one cannot place all metal atoms at the same substrate sites in an extended ordered hexagonal network. The simulated model thus gives proof of a mismatch between the Ag-TEB OMN and the Ag(111) substrate, which causes some distortion in the network, and leads to the rectangular unit cell rather than the rhombic counterpart of the hexagonal structure. Besides, the alkynyl-Ag-alkynyl structure is flexible as described in previous study.[21, 75, 140] Therefore, the Ag-TEB OMN may be distorted due to this

mismatch, whereas the Cu-TEB tends remain hexagonal.

In the following, we proceed to explain the principle driving force inside of the transmetalation on the surface focusing formation energy for the alkynyl-M-alkynyl structures. The DFT calculated formation energy for Ag-TEB and Cu-TEB OMN was apparently different. $E_{bind(Ag/rectangular\text{-}13)}$ = -3.88 eV for Ag-TEB OMN, and $E_{bind(Cu/hexagonal)}$ = -6.90 eV for Cu-TEB OMN. Thus, one can clearly see that the formation energy for alkynyl-Cu-alkynyl is lower than for alkynyl-Ag-alkynyl by 3.0 eV, which emphasizes that alkynyl-Cu-alkynyl is significantly more stable than alkynyl-Ag-alkynyl linkage.

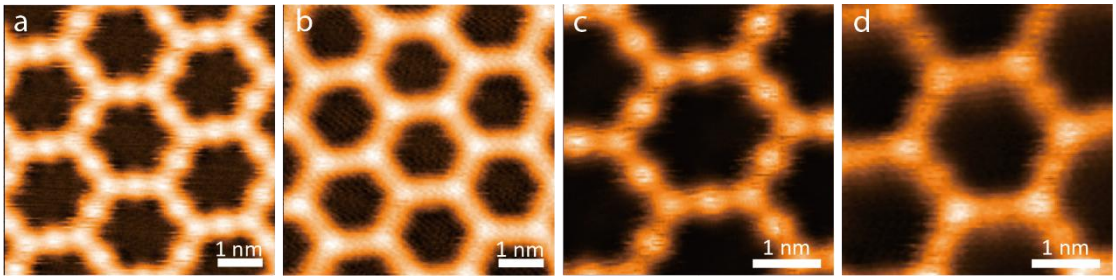

Figure 4.4: High-resolution STM images of (a) Ag-TEB and (b) Cu-TEB OMN with constant current scanning mode. Scanning parameter for (a) and (b): V_b = -10 mV, I_t = 1 nA. Zoom-in STM images of a single pore of Ag-TEB (c) and Cu-TEB OMN (d) recorded at constant height scanning mode at V_b = 10 mV.

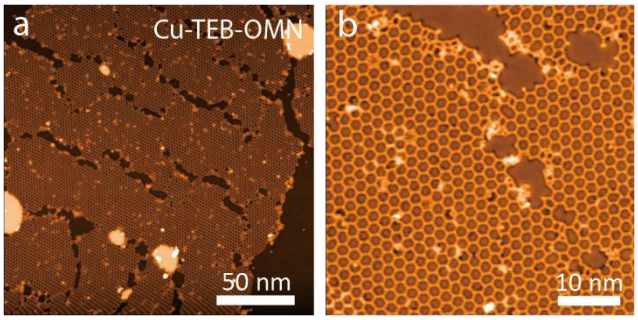

Figure 4.5: Large-area STM images of Cu-TEB OMN with 0.2 µm-size (a) and 50 nm-size (b). The tunneling parameters are V_b = -1 V, I_t = 300 pA (a); V_b = 380 mV, I_t = 100 pA (b).

Notably, in Figure 4.1c the midpoints on each side of the hexagonal outline, identified as embedded metal adatoms, display different contrast with respect to the surroundings as compared to Figure 4.1a. Ag atoms appear distinctly brighter than Cu at the same scanning bias. Figure 4.4a, b presents high resolution STM images of the Ag-TEB and Cu-TEB OMN, respectively. As observed, with the same scanning parameters, on the edges of the honeycomb pore in Ag-TEB OMN, three bright dots are visible. The dots located at the two ends of an edge (thus at the hexagon's corners)

are attributed to the benzene rings of each TEB molecule, whereas midpoint dots are identified as the Ag atoms. As for the Cu-TEB OMN, instead, the central dot of each single hexagon side is much dimmer than the adjacent benzene rings. These same appearances are revealed in close-up constant-height STM images of the single pore (Figure 4.4c, d). Accordingly, comparing the lattice parameters as well as the general appearance of both OMNs before and after Cu addition, a smooth transformation from Ag-TEB to Cu-TEB OMN is inferred. As shown in Figure 4.5, the presence of large-area domains characteristic for Ag-TEB OMNs is retained upon transmetalation. Furthermore, excess Cu atoms gathered and grew into small Cu islands (Figure 4.5a) due to increased diffusion in the annealing process, promoting the organization into a neat OMN at 500 K.

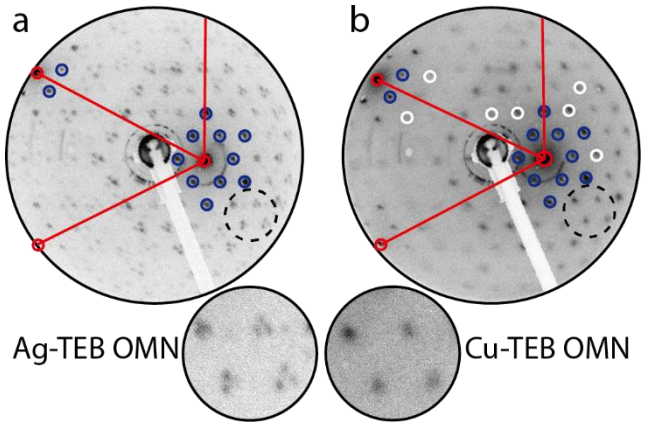

Figure 4.6: LEED patterns for Ag-TEB OMN (a) and Cu-TEB OMN formed after Cu deposition on deprotonated TEB and annealing at 500 K (b); the zero- and first-order diffraction spots are encircled in red and the $< \bar{1}\bar{1}2 >$direction of real-space are marked by red lines. The insets show the magnification of partial pattern spots circled by the black dashed lines. The LEED patterns were acquired at a primary electron energy of 30 eV.

Additional LEED measurements were performed to characterize the long-range order and superstructure periodicity on the surface preparations to further substantiate the transition from Ag-TEB to Cu-TEB OMNs. Figure 4.6 depicts the experimental LEED pattern acquired at 90 K for the pristine Ag-TEB OMN corresponding to the structure shown in Figure 4.1a. The LEED pattern in Figure 4.6b reflects the structure obtained after Cu deposition and annealing to 500 K. The spots highlighted by blue circles appear equally sharp for both OMNs, moreover, in the immediate vicinity of the zero-order spot they outline a hexagon, in agreement with the quasi-hexagonal porous networks of Figure 4.1a, c. However, the spots marked by white circles in Figure 4.6b

emphasize single spots which split into three distinct reflexes in the Ag-TEB OMN (Figure 4.6a), regardless of the primary electron energy (cf. Figure 4.7 and Figure 4.8), which can also be observed clearly from the magnification of partial patterns. These characteristic triplets from hexagonal symmetry denote multiple domains with slight distortion present in the Ag-TEB OMN, in agreement with the glide symmetry relation for adjacent distorted hexagonal columns, which is absent for the Cu-TEB OMN. The subtle change in lattice periodicity is thus reflected in a clear difference of LEED characteristics for the two distinct OMNs, as evidenced in Figure 4.6 and further summarized in Figure 4.9 and Figure 4.10. Besides, the LEED patterns of the two OMNs after annealing at the same temperature of 450 K are reported in Figure 4.11.

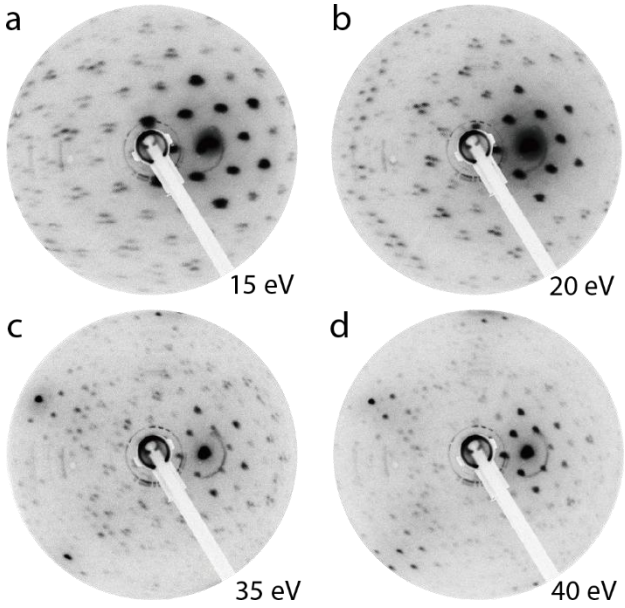

Figure 4.7: LEED patterns of Ag-TEB OMN acquired at 90 K with primary electron energy of 15 eV (a), 20 eV (b), 35 eV (c) and 40 eV (d).

Specifically, herein we propose an superstructure matrix $\begin{pmatrix} 13 & 0 \\ 4 & 8 \end{pmatrix}$ for the Ag-TEB OMN periodicity according to models' parameters from Figure 4.3, as shown in Figure 4.9a, whose reciprocal-space pattern was simulated via the LEEDpat simulator software (https://www.fhi.mpg.de/958975/LEEDpat4). The real-space structure encompasses three inequivalent symmetry domains and the resulting reciprocal-space pattern matches well the experimental LEED pattern of Ag-TEB OMN (Figure 4.6a and Figure 4.7) with characteristic triplet motifs. Additionally, this matrix is consistent with the rectangle unit cell in Figure 4.1a and Figure 4.9c with $a = 37.6 \pm 0.2$ Å, $b = 20.7$ Å $\pm$ 0.2 Å, $\gamma \approx 90.2 \pm 1°$. The agreements emphasize the reasonability of the Ag-TEB OMN model shown in Figure 4.3. Conversely, the LEED pattern of Cu-TEB OMN shown in

Figure 4.9b can be assigned to the superstructure matrix $\begin{pmatrix} 8 & -4 \\ -4 & 8 \end{pmatrix}$, corresponding to a well-defined $\left(4\sqrt{3} \times 4\sqrt{3}\right)$R30° periodicity relative to the underlying substrate. This assignment is in excellent agreement with the rhombus primitive cell of Figure 4.9d for Cu-TEB OMN with lattice parameters a = 20.1 ± 0.2 Å, b = 20.3 ± 0.2 Å, $\gamma \approx 59.2° \pm 1.0°$, and is corroborated by the absence of spot splitting in the LEED patterns of the Cu-TEB OMN at different primary electron energies (cf. Figure 4.8).

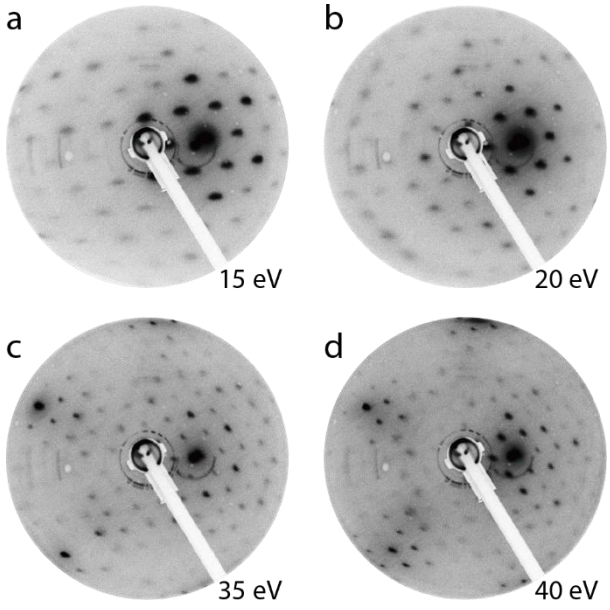

Figure 4.8: LEED patterns of Cu-TEB OMN acquired at 90 K with primary electron energy of 15 eV (a), 20 eV (b), 35 eV (c) and 40 eV (d).

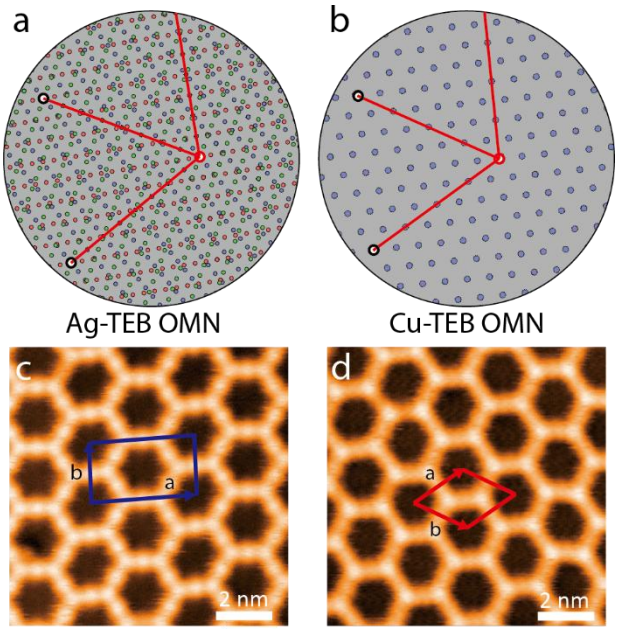

Figure 4.9: (a) Simulated LEED pattern for a real-space superstructure matrix $\begin{pmatrix} 13 & 0 \\ 4 & 8 \end{pmatrix}$ of Ag-TEB OMN. (b) Simulated LEED pattern corresponding to the real-space superstructure matrix $\begin{pmatrix} 8 & -4 \\ -4 & 8 \end{pmatrix}$ for Cu-TEB OMN. (c) STM image of Ag-TEB OMN, with the unit cell marked in blue. (d) STM image of Cu-TEB OMN with red-marked rhombic primitive cell. Tunneling parameters for (c) and (d) are V_b = 100 mV, I_t = 1 nA.

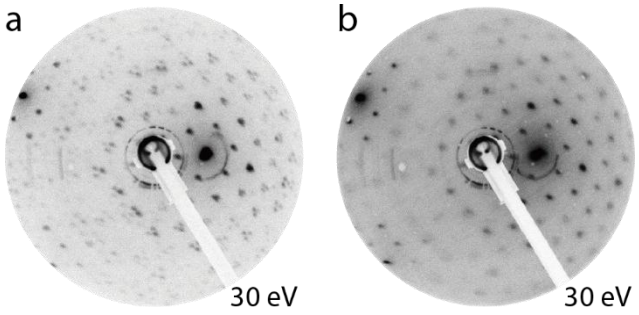

Figure 4.10: As-recorded LEED patterns extracted from Figure 4.6 without any overlapping drawing. (a) Ag-TEB OMN and (b) Cu-TEB OMN with the same primary electron energy of 30 eV. The disappearance of the triple (split) diffraction spots going from a to b is evident.

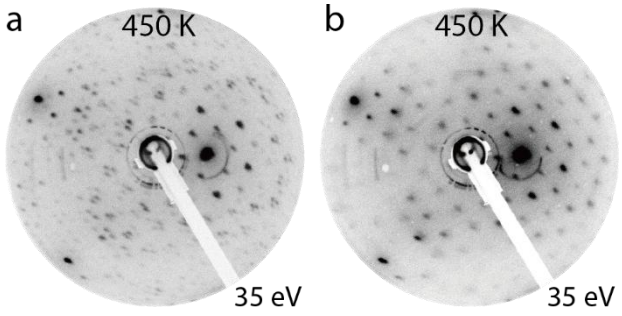

Figure 4.11: LEED patterns for (a) Ag-TEB OMN and (b) Cu-TEB OMN after annealing at 450 K, both taken with the same primary electron energy of 35 eV.

The LEED pattern for Ag-TEB at 450 K is shown in Figure 4.11a, which maintains the same pattern as Ag-TEB at 375 K (cf. Figure 4.6a and Figure 4.10a). The ordered LEED pattern for Ag-TEB could not be obtained at 500 K, since the network decomposed at such temperature. However, the LEED pattern for Cu deposition on Ag-TEB followed by annealing at 450 K is compared in Figure 4.11b, which shows the same lattice periodicity as Cu-TEB OMN at 500 K (cf. Figure 4.6b and Figure 4.10b). The disappearance of triple dot motifs indicative of transmetalation from Ag-TEB to

Cu-TEB can still be recognized clearly.

Chemical insight supporting the transmetalation was obtained by XPS. Figure 4.12 depicts the Cu 2p3/2 core-level spectrum of the Cu-TEB OMN (top), recorded after annealing at 500 K, which is compared to the spectrum of metallic copper upon Cu deposition onto pristine Ag(111) (bottom). These spectra reveal that the Cu 2p3/2 peak position undergoes a binding energy shift of 0.5 eV, attributed to the organometallic linkages expressed. In addition, a weak component attributed to residual metallic Cu (unreacted) is found after peak fitting (cf. Figure 4.13a). For reference, note that the Cu 2p3/2 binding energy position does not change for Cu deposited on pristine Ag(111) after annealing at 450 K and 500 K (cf. Figure 4.13b). This advocates the conclusion that the chemical state of deposited Cu atoms has changed due to the interaction with TEB molecules, leading to alkynyl-Cu-alkynyl linkages, and not simply due to the thermal evolution of the Cu atomic environment on Ag(111).

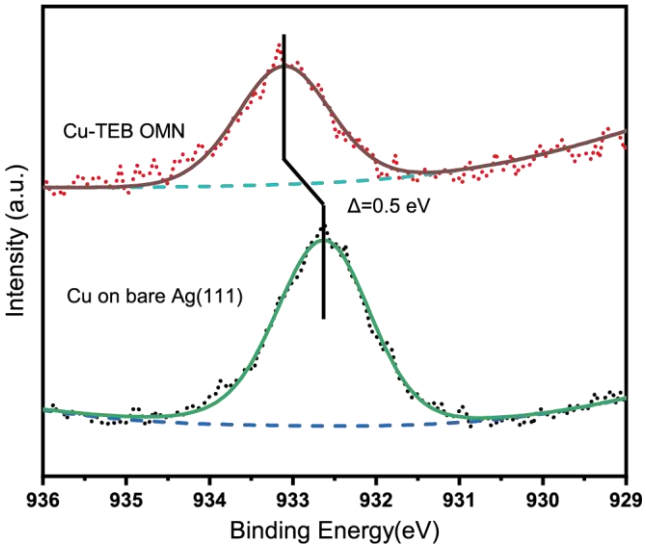

Figure 4.12: XPS measurements of the Cu 2p3/2 core level for the Cu-TEB OMN after annealing at 500 K (top) and for Cu deposited onto pristine Ag(111) at 300 K (bottom).The experimental data are shown as dots, the black and green lines denote fitted curves, and the dashed blue lines represent the secondary electron background. The chemical shift of 0.5 eV upon Cu incorporation into the OMN is highlighted by the vertical lines.

Furthermore, we also assessed for comparison an alternative method to form the Cu-TEB OMN without the initial preparation of the Ag-TEB OMN (see Figure 4.14). Pristine TEB molecules self-assembled on Ag(111) were exposed to O_2 gas at an amount of 600 L at 200 K, forming deprotonated TEB. Subsequently, an appropriate

amount of Cu atoms was dispersed onto the deprotonated TEB self-assembly at 200 K, followed by stepwise annealing up to a final temperature of 450 K. In the real-space STM images of Figure 4.14 the three subsequent stages of this preparation protocol used to form a Cu-TEB OMN are shown. The final structure of panel c matches the Cu-TEB OMN obtained through transmetalation. Strikingly, a smaller yield of Cu-TEB OMN occurred compared to Figure 4.1c, which observations signal that the transmetalation approach (using the protocol shown in Scheme 4.1) is more effective and flexible.

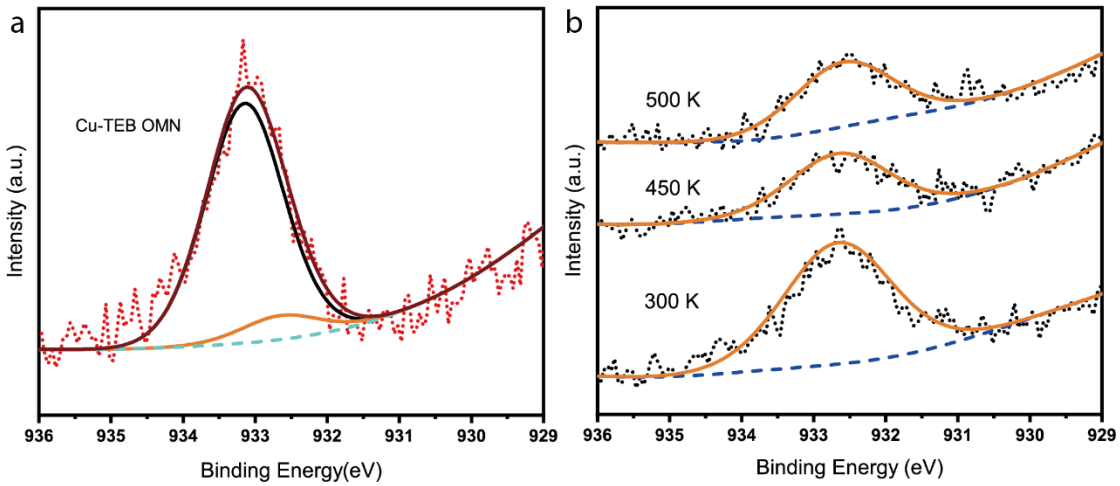

Figure 4.13: (a) Peak fit for the XP spectrum of the Cu $2p_{3/2}$ core level of the Cu-TEB OMN after annealing at 500 K. (b) Cu $2p_{3/2}$ XP spectra and fitting analysis for Cu deposited onto the pristine Ag(111) surface after annealing at 300 K (bottom), 450 K (middle) and 500 K (top), respectively.

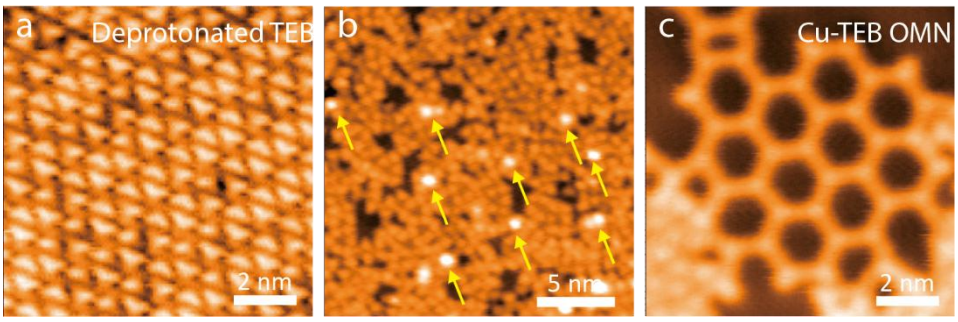

Figure 4.14: STM images of (a) deprotonated TEB self-assembly, and of Cu addition onto deprotonated TEB self-assembly at 200 K (b) before and (c) after annealing at 450 K. In (b) Cu clusters are pointed out by yellow arrows. Tunneling parameters: (a) V_b = -100 mV, I_t = 1 nA; (b) V_b = -100 mV, I_t = 300 pA; and (c) V_b = 100 mV, I_t = 1 nA.

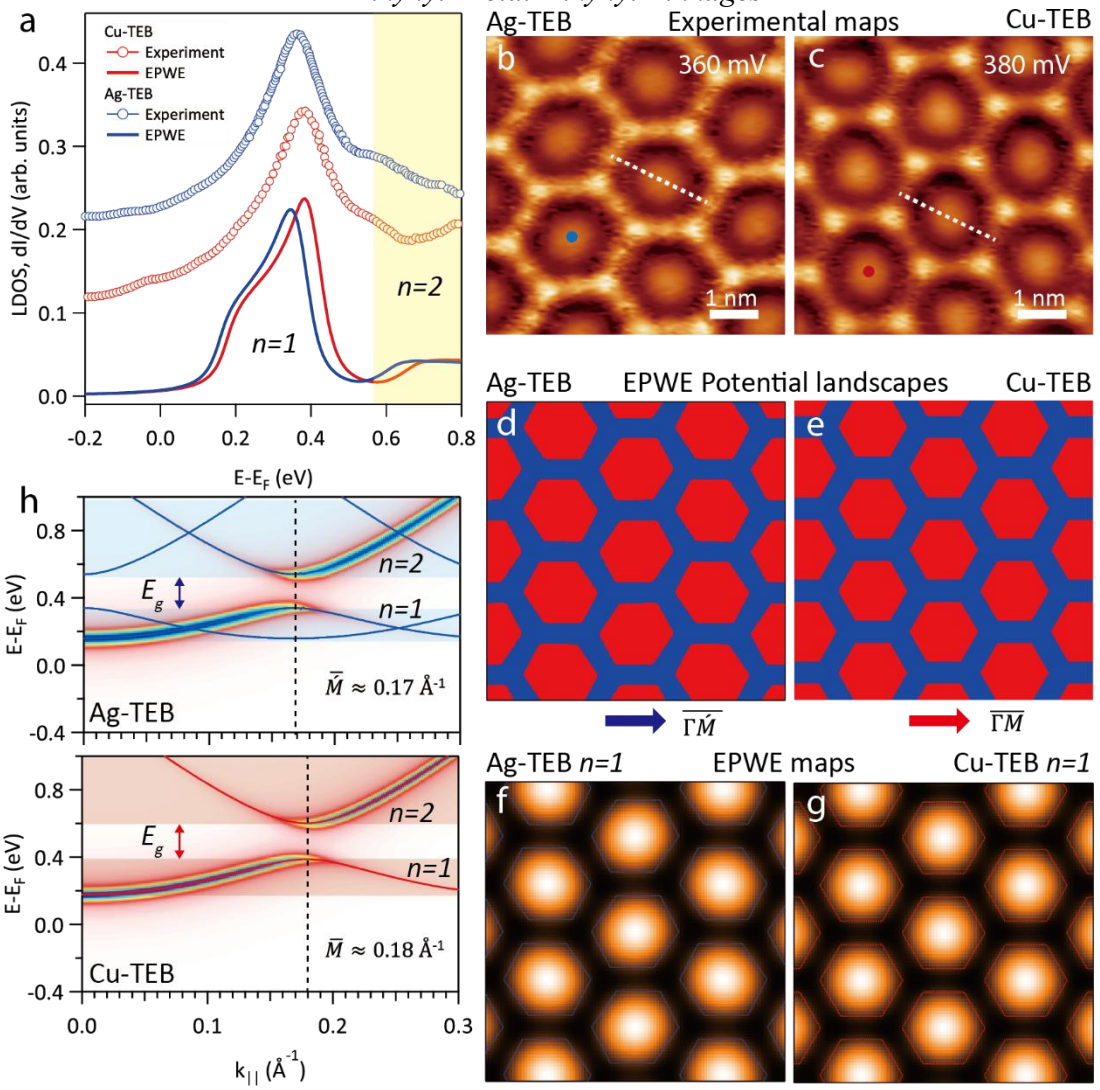

Figure 4.15: Surface state confinement in Ag-TEB and Cu-TEB OMNs. Panel (a) compares the calculated LDOS from EPWE (electron plane wave expansion) simulations with the experimental dI/dV spectra. (b) and (c) present the dI/dV mapping of Ag-TEB and Cu-TEB OMN at 360 mV and 380 mV, respectively. The tip positions for STS spectra are marked by blue and red dots in (b) and (c). EPWE simulation potential geometry for Ag-TEB (d) and Cu-TEB OMN (e). LDOS maps of (f) Ag-TEB OMN at 360 mV and (g) Cu-TEB OMN at 380 mV. (h) EPWE surface state band structure (blue and red) and photoemission spectral weight of Ag-TEB and Cu-TEB OMN. Panel (b) was scanned at V_b = 360 mV, and (c) at V_b = 380 mV.

Confinement of electronic surface states in Ag-TEB and Cu-TEB OMNs. Adsorbed nanoporous networks are known to mediate quantum confinement phenomena, notably with surface state electrons at fcc(111) coinage metal surfaces. Since these electrons are

sensitive to the pore size and shape, we study their confinement to get further insights into the electronic characteristics of the two systems. Scanning tunneling spectra (STS) were measured at the pore centers of both networks with biases between -200 and 800 mV. These results are depicted in Figure 4.15a, which presents the respective experimental dI/dV conductance curves for Ag-TEB (blue data) and Cu-TEB (red data). For the Ag-TEB OMN one discerns a peak centered at about 362 mV reflecting a resonance at the pore center, while for the Cu-TEB OMN, the maximum is distinctly blue-shifted to 386 mV, i.e. by more than 20 mV (see Figure 4.16 for long-range STS spectra from -1.0 V to 1.5 V). Moreover, constant-height dI/dV maps at 360 mV and 380 mV offer distinctly identifiable confinement states in the pores of Ag-TEB and Cu-TEB OMNs, respectively, as shown in Figure 4.15b, c (the original, constant-height STM topographic images are shown for reference in Figure 4.17a, b).

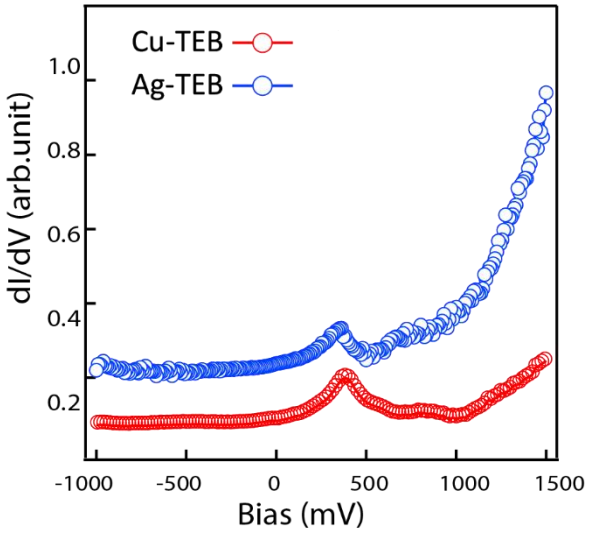

Figure 4.16: Long-range dI/dV spectra from -1.0 V to 1.5 V of the Ag-TEB (blue curve) and Cu-TEB (red curve) OMN at the pore centers**.**

To better understand the origin of the electronic differences, we focus on the slightly different pore sizes upon transmetalation. Accordingly, semi-empirical electron plane wave expansion (EPWE) simulations of both OMNs are utilized to unravel the origin of the observed blue shift. The potential landscapes for EPWE modeling were constructed according to the topographic images and are shown in Figure 4.15d, e. The red regions stand for the Ag(111) substrate with zero potential and the blue areas correspond to potential barriers (V) set at the position of the metal-organic backbone in Ag-TEB (Figure 4.15d) and Cu-TEB OMN (Figure 4.15e). The barrier width at the sides of the honeycomb OMN is fixed to 5.0 Å, which is estimated from experimental

high-resolution STM images, and the OMNs structure are considered to exert a repulsive potential to surface electrons. We define the surface state reference E_{ref} = -0.058 eV, V = 0.6 eV and the effective mass meff = 0.39 me, as the calculation parameters.[141] For the sake of simplicity, the simulation method neglects the contribution originating from the two different kinds of metal atoms, keeping the focus on the size and deformation of the two pores. As a result, the calculated local density of states (LDOS) spectral features agree well with the experimental dI/dV curves, where the experimental shift is well reproduced by the EPWE simulations, as proven in the bottom of Figure 4.15a. Meanwhile, Figure 4.15f, g provide the calculated LDOS maps with corresponding energy at 360 mV for Ag-TEB OMN, and 380 mV for Cu-TEB OMN, which are in good agreement with Figure 4.15b, c, respectively.

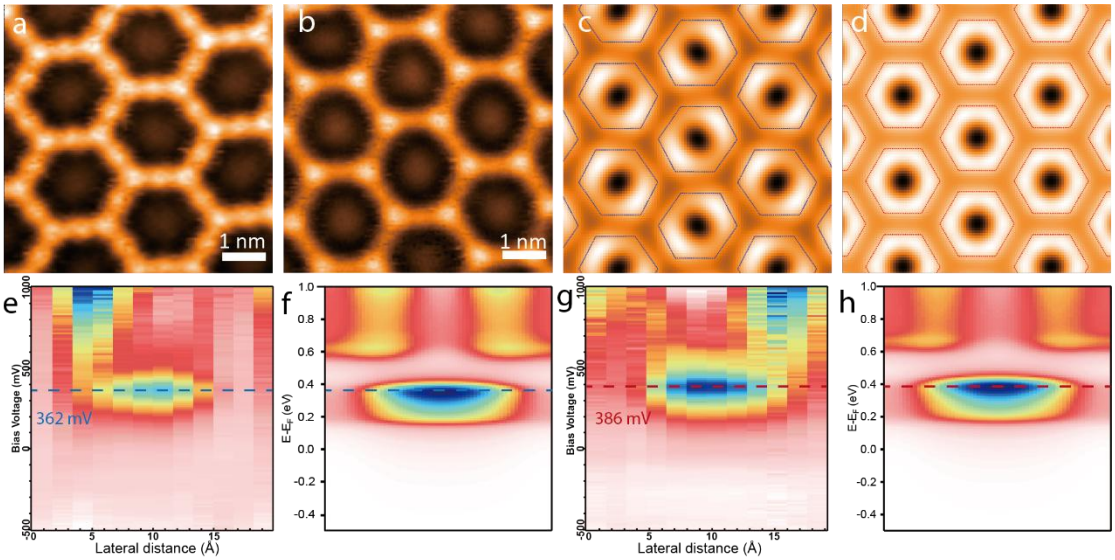

Figure 4.17: Constant-height STM images of (a) Ag-TEB OMN at the bias V_b = 360 mV and (b) Cu-TEB OMN at the bias V_b = 380 mV, corresponding to Figure 4.15b and 4.15c of the main manuscript, respectively. Theory LDOS map for Ag-TEB at 660 mV (c), and for Cu-TEB OMN at 680 mV (d). Panel (e) and (g) depict STS line spectra across the pore centers of Ag-TEB and Cu-TEB OMN along the white dash line marked in Figure 4.15b and c. Then simulated LDOS line spectra for Ag-TEB and Cu-TEB OMN are presented in panel (f) and (h), respectively.

In addition, according to the calculation by EPWE, we obtained the surface state band structures of Ag-TEB OMN and Cu-TEB OMN as indicated in Figure 4.15h. The band structures consist of two main bands separated by an energy gap for the two types of OMNs. The additional bands for Ag-TEB originate from the conventional centered rectangular unit cell enclosing two pores, but they carry no spectral weight as

demonstrated from the simulated photoemission intensity.[142-144] Therefore, consistent with LEED observation, the photoemission spectral weight follows a quasi-hexagonal lattice with slightly different M' and M-point for Ag-TEB and Cu-TEB. The low energy bands (n = 1) correspond to a bound state with some coupling corresponding to 360 mV and 380 mV, while the bands above the energy gap (n = 2), represent the scattering state above the barrier energy corresponding to 660 mV and 680 mV respectively. The EPWE simulation LDOS map at 660 eV for Ag-TEB OMN and 680 eV for Cu-TEB OMN are shown in Figure 4.17c, d, respectively, revealing weak donut-like shapes typical for n = 2 states.

In order to gain more detailed electronic information on the pores, line STS were acquired across the pores along a line through the pore center crossing two metal atoms (white dashed lines drawn in Figure 4.15b, c). From the STS color-coded contour plots, as shown in Figure 4.17e, g, the strong central maxima located at 362 mV and 386 mV are observed, whereby EPWE simulations for Ag-TEB and Cu-TEB OMN (cf. Figure 4.17f, h) agree well with the experimental results. Therefore the STS peak shift of the confined state further supports the formation of a Cu-TEB OMN from the original Ag-TEB OMN.

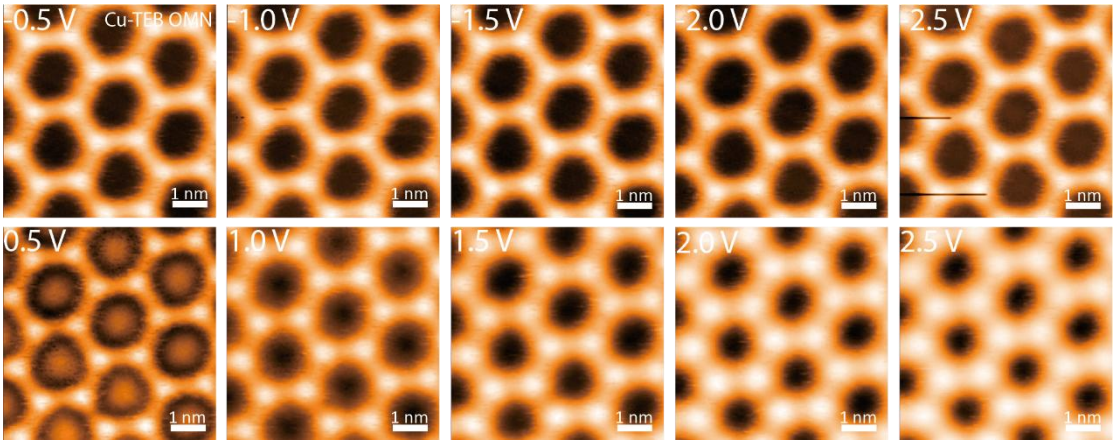

Figure 4.18: Bias-dependent STM images for Cu-TEB OMN at I_t = 300 pA.

The bias-dependent STM images of both OMNs are also compared in Figure 4.18 and Figure 4.19. TEB benzene ring parts located at the vertex of both OMNs and Ag atoms at midpoint of pores sides are imaged as bright protrusions, with brightness varying with the bias voltage changes. However, Cu metal atoms were imaged darker than benzene rings. In both OMNs, the n = 1 confined surface state of substrate in the pores can be apparently imaged at 0.5 V which is consistent with the dI/dV curves.

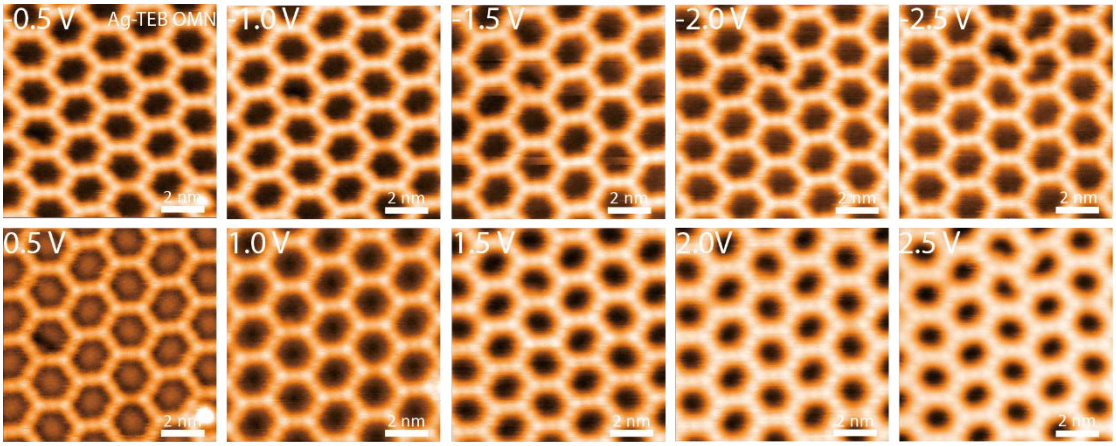

Figure 4.19: Bias-dependent STM images for Ag-TEB OMN at I_t = 1 nA.

Thermal stability and induction of alkynyl-alkynyl homocoupling. Besides the electronic differences, the Cu-TEB OMN exhibits a distinctly higher thermal stability than the Ag-TEB counterpart. Figure 4.20a shows that the Ag-TEB OMN decomposes after annealing at or below 500 K. Conversely, the Cu-TEB OMN is preserved intact even after annealing at 600 K, as demonstrated in Figure 4.20b. This enhanced stability further corroborates the successful transformation from the Ag-TEB OMN to the distinctly more robust Cu-TEB OMN. Based on the higher stability of Cu-TEB network, the possible covalent homocoupling of alkynyl groups can be explored by further thermal treatment. This may open a potential route to the engineering of single-layer graphdiyne materials under controlled conditions, since the debate of (non-)dehydrogenative alkyne coupling scenario on noble metal surfaces signals potential difficulties when targeting alkynyl-alkynyl connections obtained from terminal alkynes.

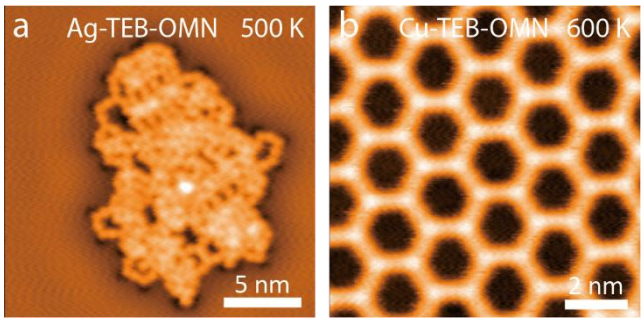

Figure 4.20: (a) STM images for the structure of Ag-TEB OMN emerging after annealing at 500 K and for (b) Cu-TEB OMN after annealing at 600 K. Tunneling parameters are V_b = -100 mV, I_t = 500 pA in (a) and V_b = -100 mV, I_t = 200 pA in (b).

4. Transmetalation in Surface-Confined Single-Layer Organometallic Networks with Alkynyl-Metal-Alkynyl Linkages

Indeed, upon annealing the Cu-TEB network up to 500 K, the STM image of Figure 4.21a shows that some edges of hexagonal pores in the Cu-TEB OMN (inside the dashed yellow region) are occasionally imaged brighter than others. The zoom-in STM image of Figure 4.21b acquired coincidentally with a special tip reveals the missing central bright dot at lower bias (indicated by arrows), at variance with the typical appearance of the alkynyl-Cu-alkynyl bridges. This structure is associated with alkynyl-alkynyl homocoupling schematically depicted in Figure 4.21c, where the DFT optimized model of alkynyl-Cu-alkynyl linkage and the alkynyl-alkynyl coupling structure in the gas phase are compared. As the length of the former is 11.81 Å and that of the latter 9.43 Å, the alkynyl-alkynyl distance is shortened by 2.38 Å. As indicated in Figure 4.21d, also in the STM data the length of the two structures across their line profile (dashed red and black lines) differs. Referring to the maxima, the red (11.9 ± 0.3 Å) is about 2.6 Å longer than the black connection (9.3 ± 0.5 Å), signaling a modified bonding motif, tentatively assigned to alkynyl homocoupling.

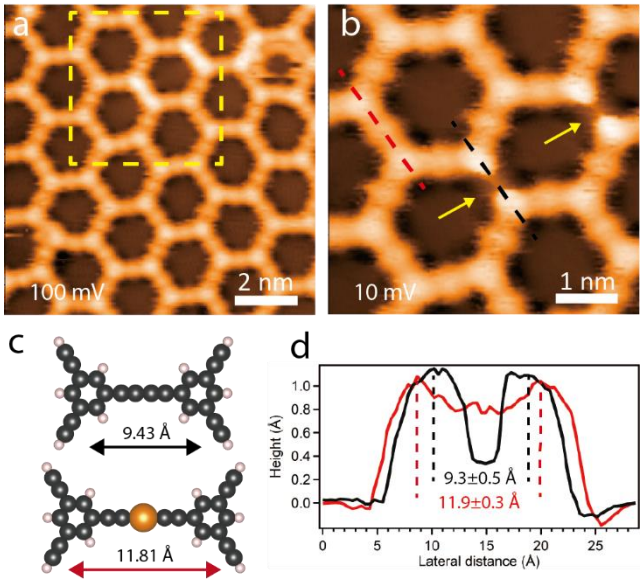

Figure 4.21: (a) Large-area and (b) zoom-in STM images of a Cu-TEB OMN with alkynyl-alkynyl coupling structures, scanned at V_b = 100 mV, I_t = 100 pA (a) and V_b = 10 mV, I_t = 100 pA (b), respectively. (c) DFT Optimized model of alkynyl-alkynyl (top) and alkynyl-Cu-alkynyl (bottom) coupling of TEB dimers in the gas phase. (d) Experimental profiles measured along alkynyl-alkynyl (black) and alkynyl-Cu-alkynyl coupling (red) direction.

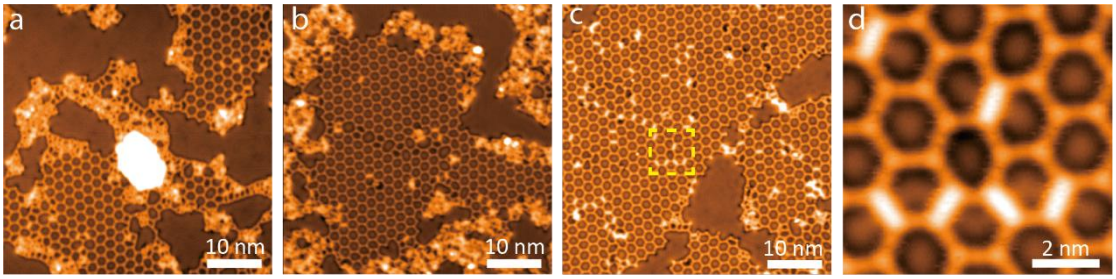

Figure 4.22: STM images of Cu-TEB OMN (a) after annealing at 500 K for 1 h and (b) at 600 K for 10 mins. (c) Large-area and (d) zoom-in STM images of Cu-TEB OMN containing alkynyl-alkynyl coupling linkages. (a) (c) and (d) were scanned at $V_b = 380$ mV and $I_t = 300$ pA, (b) was scanned at $V_b = 370$ mV and $I_t = 200$ pA.

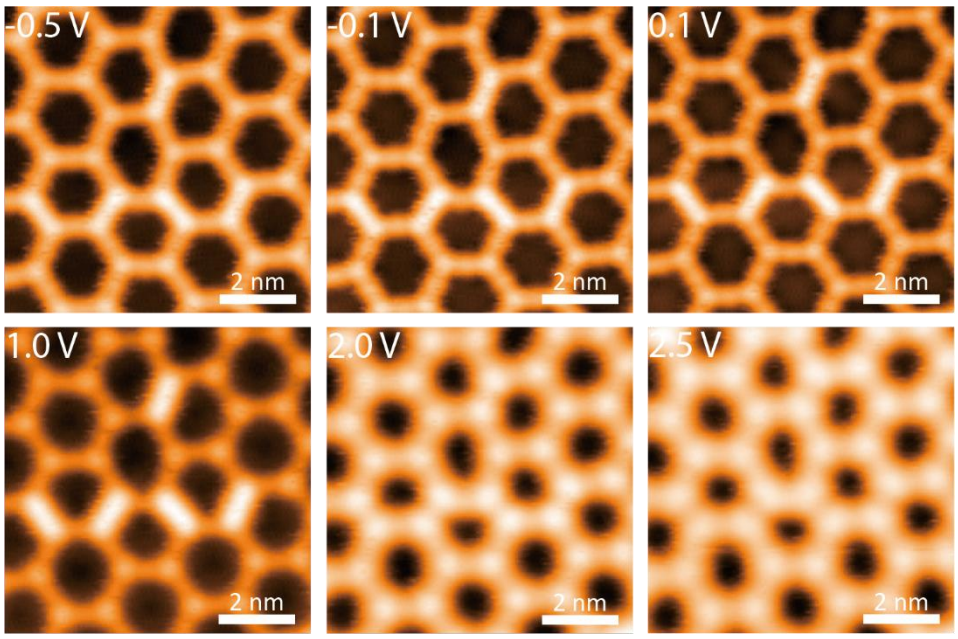

Figure 4.23: Bias-dependent STM images of alkynyl coupling structures at $I_t = 300$ pA. The alkynyl-alkynyl linkage has different appearances and contrast with respect to the alkynyl-Cu-alkynyl linkage at 1 V bias, but turns to equal brightness after rising the bias to 2 V.

The increased thermal stability of the Cu-TEB OMNs facilitates the initiation of the alkynyl-alkynyl homocoupling at elevated conditions. However, either extending the annealing time to 1 hour at 500 K or increasing the annealing temperature to 600 K (Figure 4.22a-b) does not yet promote the large structure of diacetylene linkages. Moreover, the network started decomposing with long annealing time or higher annealing temperature. One promising strategy might be the introduction of gas

atmosphere as reducing agents during thermal treatment. Figure 4.22c reports a larger-area image where more bright segments attributed to alkynyl-alkynyl coupling appeared after annealing at 500 K in ammonia atmosphere. The latter was used deliberately as a reducing agent. In Figure 4.22d, even hexagons with two modified linkages could be observed, *i.e.* without the typical protrusions encountered for alkynyl-Cu-alkynyl linkages. Bias-dependent images for the structure of Figure 4.22d are shown in Figure 4.23, the alkynyl coupling part being resolved as a bright rod, while other hexagonal sides were "normal" when imaged at voltages below 1.0 V. In contrast, the alkynyl coupling segment splits into two protrusions which are located at the benzene positions, and coupling bond sites turn dark for bias above 2.0 V. Thus, the successful occurrence of alkynyl-alkynyl homocoupling is likely, in marked contrast to the case of the Ag-TEB OMN for which disruption of the network prevails at elevated temperatures over the covalent homocoupling (cf. Figure 4.20a). Thus the OMN transmetalation bears promise as viable approach towards obtaining in a multi-step reaction scheme regular all-carbon graphdiyne networks on surfaces. Nevertheless, there may be deeper factors deserving further systematic investigation in order to explore a rationale regarding transmetalation protocols for surface-confined organometallic networks, such as the accessible oxidation states of the metal atoms, the diverse ability of multifold coordination in the preexisting structural motif as well as different carbon-metal interaction strengths (cf. Figure 4.24).

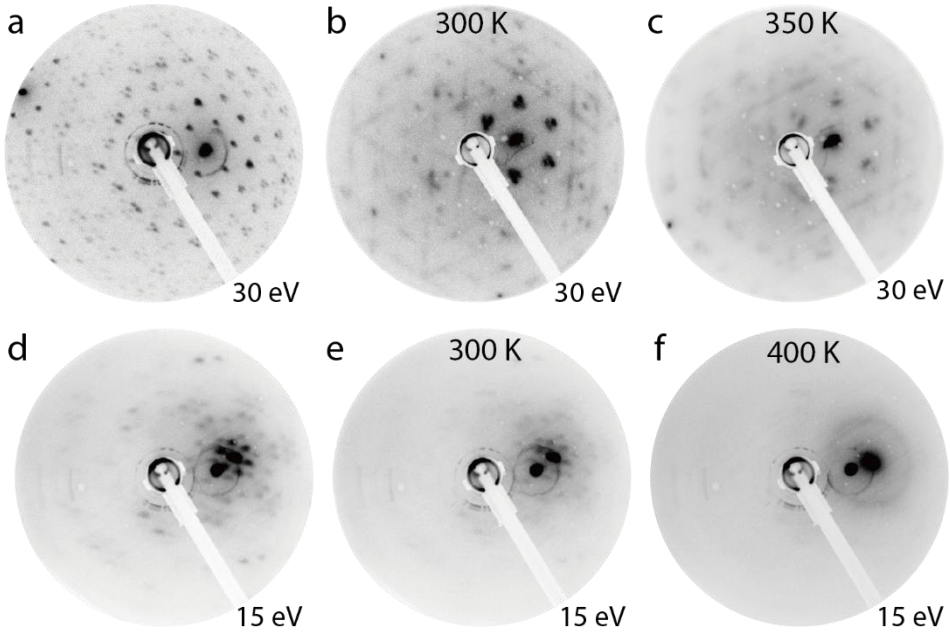

Figure 4.24: Top line: LEED patterns for Ag-TEB OMN (a), Bi on Ag-TEB OMN at

300 K (b) and followed by annealing at 350 K (c), acquired at 90 K with primary electron energy of 30 eV. Bottom line: LEED patterns for Ext-TEB OMN (d), Ni deposition on Ext-TEB OMN at 300 K (e) and followed by annealing at 400 K (f), acquired at 90 K with primary electron energy of 15 eV.

We also tried Bi to replace Ag in the Ag-TEB system by LEED. As shown in Figure 4.24a, b and c, the addition of Bi still maintains rotational domains leading to some dot triplets reminiscent of the Ag-TEB OMN pattern, but new features indicative of a weaker, new ordered periodic structure appeared, suggesting that Bi may modify the Ag-TEB network. However, the LEED pattern turned into much weaker after annealing at 350 K, proving lower as well as weaker structural order than the Ag-TEB OMN. Therefore, it is unlikely that Bi simply replaces Ag in the networks. Additionally, in the system of Ni combined with the Ext-TEB molecule (which also has terminal alkynyl groups), LEED measurements did not support the successful replacement of Ag with Ni atoms. Figure 4.24d-f shows the LEED pattern of the Ext-TEB network and its structure worsening upon Ni deposition. in particular, the long-range order is totally disrupted following followed annealing at 400 K (cf. Figure 4.24f). Thus, these metals could not demonstrate their ability to replace Ag in the pre-existing organometallic system, but instead the observed findings suggest that there may be deeper factors deserving further investigation.

Conclusion

We have explored the modification of a surface-confined single-layer OMN by transmetalation, specifically generating from an alkynyl-Ag-alkynyl to an alkynyl-Cu-alkynyl linking platform via post-synthetic reaction. Specifically, the deposition of Cu adatoms on extended organometallic honeycomb Ag-TEB networks followed by thermal annealing to appropriate temperature induces the distinct transformation of Ag-TEB into Cu-TEB OMN. The latter structure is proven to possess higher thermal stability, while maintaining a similar lattice periodicity and pore symmetry as the Ag-TEB OMN. Our work demonstrates an effective strategy to systematically prepare OMNs incorporating selected metal species and providing increased thermal stability, maintaining higher robustness for prospective applications.

5. On-Surface Synthesis and Modification of Dinuclear Organometallic Networks Combining Transmetalation Strategy

Engineering organometallic networks (OMNs) is promising in view of their potential applications in catalysis, optoelectronic devices, etc. Dinuclear metal complexes have multifunctional properties with their tunable structure and, hence, various applications in the field of OLEDs, chemosensors, and smart materials. The relatively complex structure makes it challenging to form thin films for advanced devices application. Therefore, on-surface synthesis of dinuclear organometallic networks serves as a powerful strategy to directly obtain the thin functional layers. Herein, with a designed bi-component precursor and O_2-mediated treatment, we manage to construct ordered Ag-Ag dinuclear OMNs containing C-Ag-N bridging linkers. Moreover, it is feasible to tune the electronic property and thermal stability by replacing the dinuclear metal centers via post metal-exchange method, affording C-Cu-N linkages.

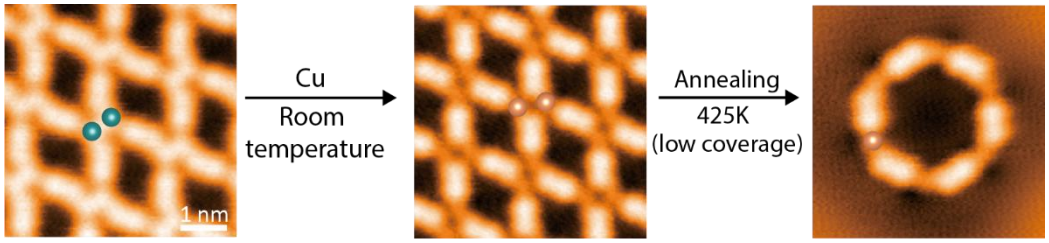

Introduction

Two-dimensional molecule-based frameworks, renowned for their tunable physical and chemical properties, have garnered significant attention over the past two decades owing to their broad applications in scientific and technological domains.[145-147] The advancement of on-surface synthesis techniques, coupled with the development of advanced surface-sensitive characterization tools, has enabled precise fabrication of single-layer molecule-based frameworks (SMFs), such as MOFs and OMNs, at the

molecular level.[129, 148, 149] Metal nodes, serving as pivotal structural components, play a crucial role in determining and modulating the functionality of SMFs. To date, a wide range of metallic elements, encompassing transition metals,[150-152] alkali metals,[153-155] and lanthanide metals,[118, 156, 157] have been successfully integrated into SMFs architectures across diverse substrate platforms. Notably, embedding metal clusters (rather than single atoms) into SMFs often enhances functionality and broadens potential applications, especially in catalysis and magnetism areas, due to magnetic and electronic interaction between metal atoms within immediate reach and multiple active sites.[156, 158-161]

However, conventional multinuclear single-layer MOFs primarily depend on coordination bonding between metal centers and organic linkers, which are inherently constrained by their relatively weak interaction strength and compromised structural stability. In contrast, OMNs constructed through organometallic bonds, which involve the direct sharing of unpaired electrons between unsaturated carbons and metal atoms, exhibit enhanced structural stability while having self-correction capabilities.[19, 20, 162] This underscores the significant potential of multinuclear OMNs as a versatile and robust platform for developing advanced functional materials with tailored properties.

The transmetalation strategy has emerged as a powerful approach for in-situ modification and functionalization of 2D-MOFs, particularly in conventional coordination chemistry, offering effective means to tune properties and enhance performance.[134, 135, 163] Recently, this methodology has gained significant attention as a promising route for precisely tailoring structure-property relationships in surface-supported macrocycle construction and modification.[136, 138, 139, 164] Notably, successful implementation of transmetalation in single-layer MOF systems has been demonstrated. For instance, Wang et al. achieved the synthesis of a 2D conjugated complex using nitrogen-chromium linkages through the substitution of nickel with chromium in a nitrogen-nickel framework.[18] In our previous work, we utilized transmetallation strategy to transform the carbon-silver structure connected organometallic system with extrinsic Cu atoms into carbon-copper OMNs.[78] Despite these advancements, the in-situ simultaneous modification of metal atom pairs in multinuclear OMNs remains unexplored, representing a significant gap in the field. Additionally, heterogeneous linkage structure in OMNs is proposed endowing the supramolecular architecture outstanding performance for potential application in catalysis and optoelectronics, due to that the heterogenous nodes may induced dipolar and spin polarization originating from dissymmetric electron distribution on metal centers.[162, 165-167]

In this regards, combined with scanning tunneling microscopy (STM), scanning

tunneling spectroscopy (STS) and support by density functional theory (DFT), we employed a designed unimolecular precursor 4'-ethynyl-[1,1'-biphenyl]-4-amine (EABP) terminated with amino and alkynyl groups, enabling the formation of carbon-silver-nitrogen (C-Ag-N) and argentophilic interactions between Ag-Ag pairs linked dinuclear OMN on Ag(111) after O_2 treatment. Subsequently, we successfully substitute Ag with Cu atoms by depositing extrinsic Cu atoms on the EABP-Ag OMN sample at room temperature while preserving similar periodicity. The electronic properties of obtained OMNs were characterized by STS, showing surface state confinement feature peaks located at different position. Intriguingly, after further annealing at 425 K, the EABP-Cu OMN transferred into chiral organometallic rings (OMRs) when the molecule coverage is low. This work paves the way for diversifying the design and applications of multinuclear organometallic supramaterials.

Results and discussion

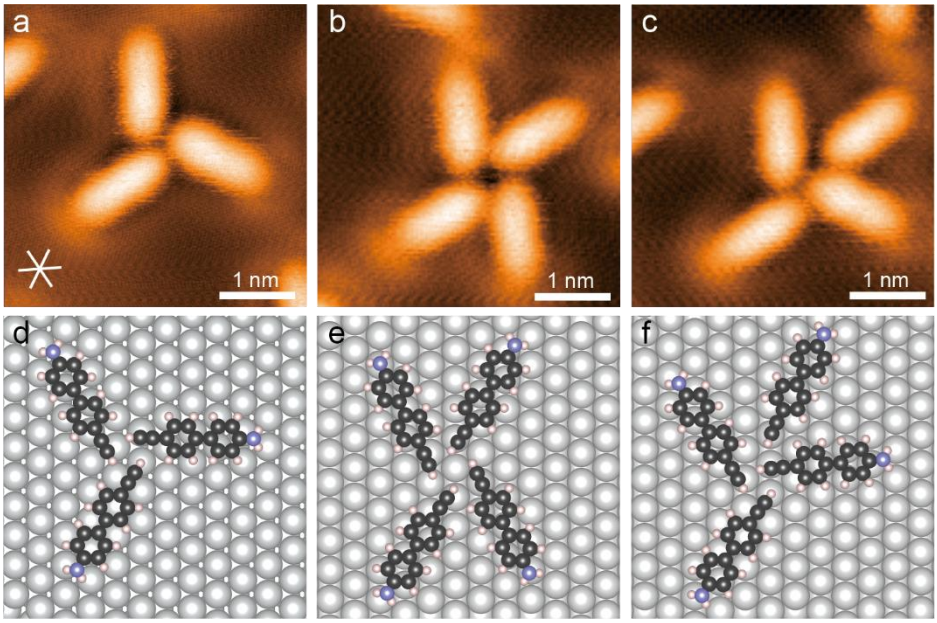

Figure 5.1: STM images for self-assembly configuration of EABP 2D-chiral trimer (a), tetramer 1(b) and tetramer 2 (c) on the Ag(111) surface. Corresponding DFT-optimized structures by DFT modeling are shown in (d), (e), and (f). Scanning parameters: V_b = -60 mV, I_t = 50 pA for (a); V_b = -100 mV, I_t = 20 pA for (b) and (c).

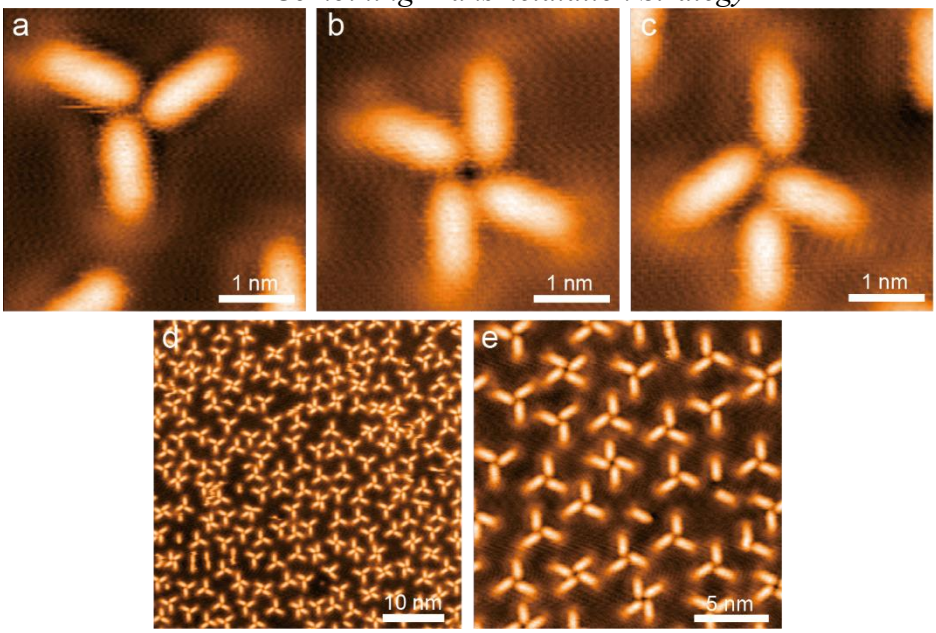

Figure 5.2: STM images of EABP Tri' (a), Te2' (b) and Te 2' (c), which are mirror-symmetry to structure in Figure 5.1a, b and c, respectively. (d) and (e) present large-area STM images for EABP self-assembly structure on Ag(111) surface. Scanning parameters: V_b = -70 mV, I_t = 50 pA for (a); V_b = -100 mV, I_t = 20 pA for (b) and (c); V_b = -300 mV, I_t = 20 pA for (d); V_b = -100 mV, I_t = 20 pA for (e).

Initially, EABP molecules are deposited on Ag(111) held at ambient temperature. As shown in Figure 5.1a,b and c, trimer (Tri), tetramer 1 (Te1) and tetramer 2 (Te2) self-assembly structure of EABP molecules were formed through the C-H···π interaction between alkynyl groups.[140, 168] However, no intermolecular communication was observed between amino groups under these low-coverage conditions, which is consistent with previous experimental findings.[94] Moreover, all types of multimer self-assembly exhibit chirality, despite the linear precursor EABP being achiral. The corresponding structures of Tri, Te1 and Te2 with mirror symmetry are illustrated in Figure 5.2a, b, and c, respectively. The supplementary large-area images for EABP behavior on Ag(111) are presented in Figure 5.2d and e, in which several dispersed absorbed sole molecules are also observed. Intriguingly, the adsorption direction of the sole molecules has a 30° offset to the close-packed direction of the Ag(111) substrate (as indicated by the crystal direction mark in Figure 5.1a). Thus, the possible configurations for single molecule adsorbed on the Ag(111) surface was modeled by DFT calculation, which suggested the most stable geometry features the benzene rings preferentially occupying hollow positions, while the amino and alkynyl groups are located at the top of substrate Ag atoms (cf. Figure 5.3). For all multimeric structure (encompassing both chiral configurations), the spiral arms also exhibiting a 30°

orientation offset relative to the close-packed direction of the Ag(111) substrate were contributed by single EABP molecules. Based on this, self-assembly structures were optimized by DFT calculation (see Figure 5.1d, e and f), which is in good agreement with the experimental results.

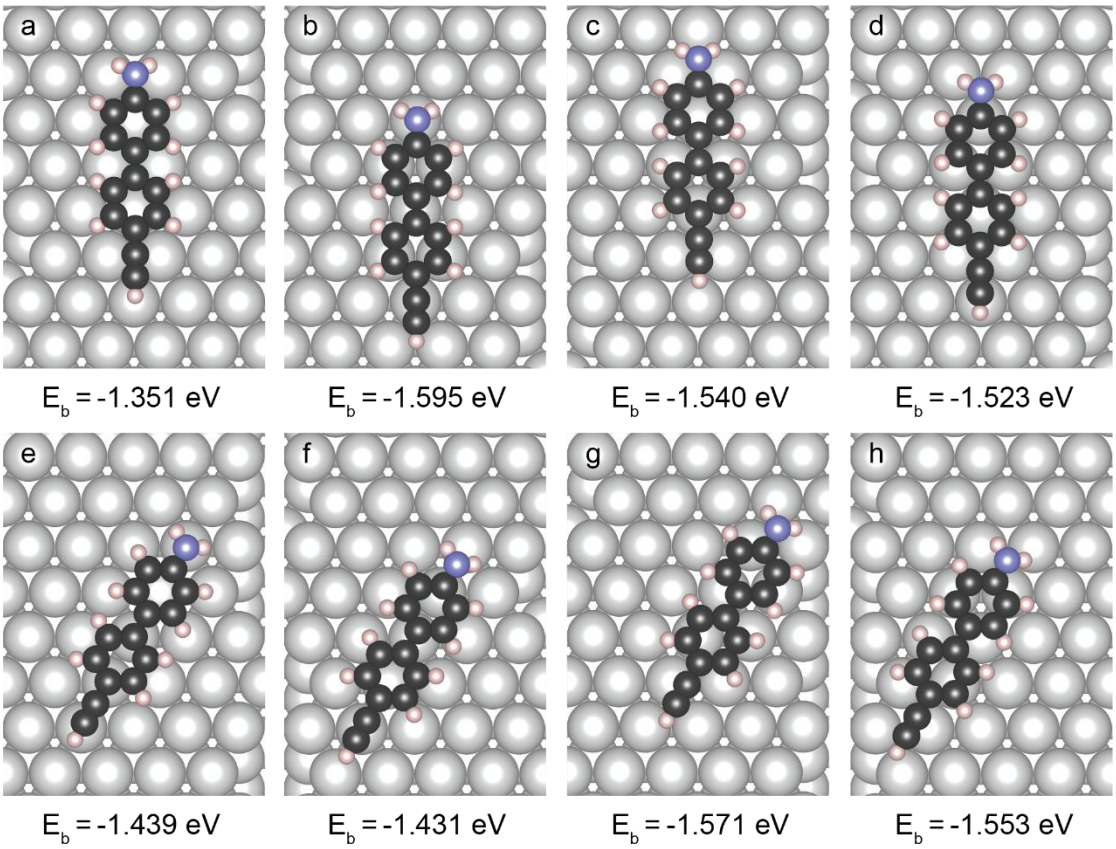

Figure 5.3: DFT-optimized geometry for single EABP molecule adsorbed on the Ag(111) surface, including its corresponding adsorption energy.

The O_2-mediated strategy serves as an effective and facile approach to facilitate dehydrogenation reactions to both alkynyl and amino functional groups, enabling the formation of well-defined organometallic molecular architectures on the Ag(111) surface, based on previous study.[21, 78] Herein, we directly exposed EABP self-assembly sample to O_2 atmosphere (60 L; 1L=1.33× 10^{-6} mbar·s) on Ag(111) held at room temperature. Figure 5.4a depicts the topography of obtained fishnet-like EABP-Ag OMN after O_2 treatment, while the corresponding large-area STM images illustrate three orientations reflecting the inherent symmetry of (111) substrate (cf. Figure 5.5). The network features parallelogram-shaped pores, each delineated by four EABP molecules interconnected through C-Ag-N linkages, as shown in Figure 5.4a. To analyze the structure of the fishnet-like OMNs, we recognize that the EABP-Ag OMN composed of EABP-Ag OMCs, as marked by black polyline in Figuer 5.4a. Moreover,

Figure 5.6 recorded a single OMC between two OMN phase providing the intuitive presentation of the EABP-Ag OMC.

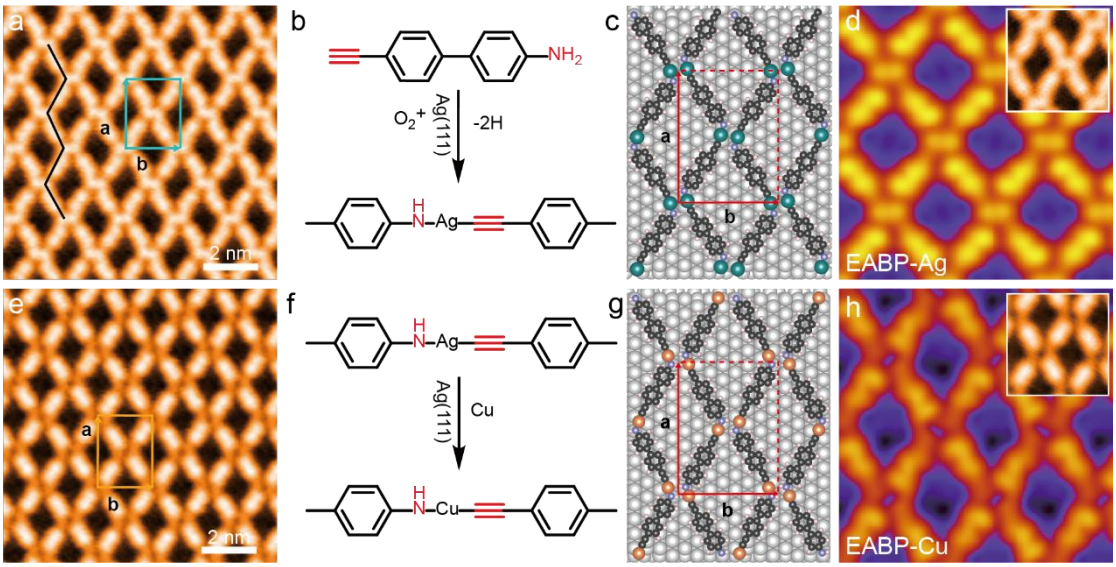

Figure 5.4: Structural characterization of EABP-Ag and EABP-Cu OMNs. (a) High-resolution STM topographic images of EABP-Ag OMN with scanning bias of -10 mV. (b) Schematic illustration of the O_2-induced dehydrogenation reaction of EABP molecules, leading to the formation of a heterogeneous C-Ag-N linkage structure. (c) depicts the DFT-optimized EABP-Ag OMN on Ag(111). (d) shows the simulated STM images with the bias of 100 mV based on DFT calculation, with the inset of corresponding experimental image captured at same bias. After conducting transmetalation strategy by deposition of extrinsic Cu atoms, the high-resolution STM image of resulted EABP-Cu OMN with scanning bias of -10 mV is given in (e), the scheme of replacing Ag metal center with Cu is shown in (f), the DFT-optimized EABP-Cu OMN structure is shown in (g). The simulated STM images with the bias of 100 mV by DFT calculation is shown in (h), with the inset of corresponding experimental images scanned by same bias. Carbon, hydrogen, nitrogen, silver and copper atoms are denoted as black, pink, blue, green and orange, respectively.

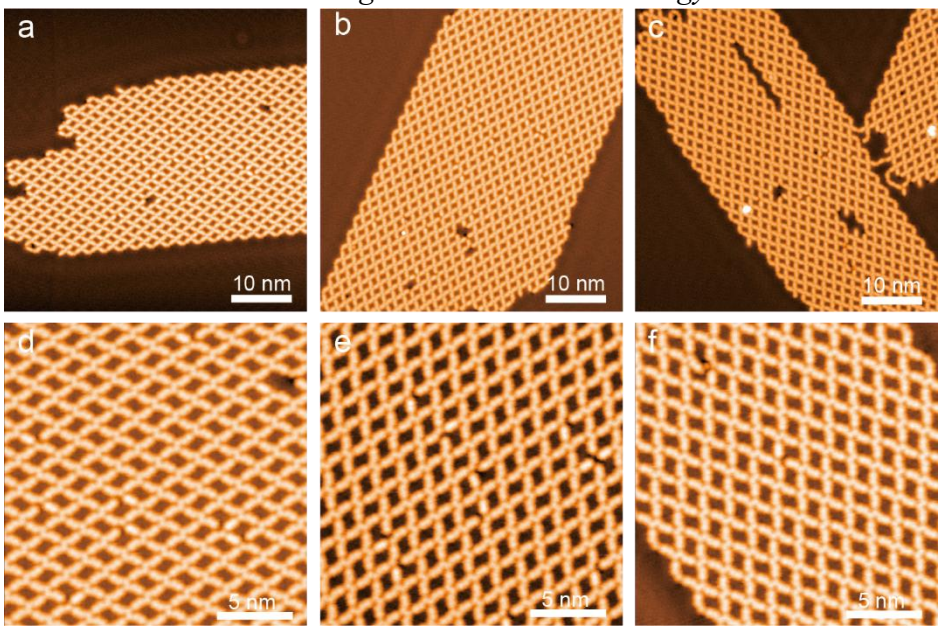

Figure 5.5: Large-area STM images of EABP-Ag OMN patches with three orientations. The corresponding zoom-in pictures are shown in bottom panel. Scanning parameters for (a), (b) and (c): V_b = -500 mV I_t = 300 pA. Scanning parameters for (d), (e) and (f): V_b = -100 mV I_t = 1 nA.

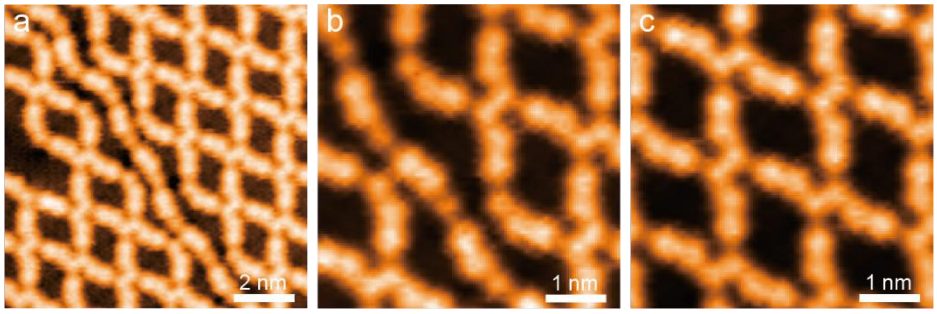

Figure 5.6: (a) High-resolution STM images of EABP-Ag OMN and OMC. (b) and (c) give constant height STM pictures for EABP-Ag OMC and OMN. Scanning parameters: V_b = 10 mV, I_t = 1 nA for (a); V_b = 2 mV for (b) and (c).

For a more detailed structural analysis, the unit cell is outlined by green rectangle exhibiting lattice parameters of a = 27.3 ± 0.2 Å, b=21.0 ± 0.2 Å, while the inner angle is 90 ± 1°. At the center of the outlined unit cell, the two protrusions are recognized as Ag-Ag pair originated from metal centers of two C-Ag-N linkages within adjacent EABP-Ag OMCs. The statistically measured interatomic distance between the Ag-Ag pair was 3.7 ± 0.4 Å. The left two connected molecules belong to same EABP-Ag OMC, while the right two molecules come from another OMC. The dehydrogenation reaction occurring at one hydrogen atom of the amino group results in a characteristic deviation

angle of the N-Ag bond from the central molecular axis of the EABP molecule.[90] Thus, it is easy to distinguish that the part above Ag-Ag pair for left OMC belongs to amino-Ag. On the other hand, the alkynyl-Ag component is positioned beneath the protrusion. Moreover, reverse arrangement is observed in the other OMC. The scheme for the formation of the C-Ag-N linkage is given in Figure 5.4b. Figure 5.4c depicts the DFT-optimized EABP-Ag OMN on the Ag(111) surface, with the unit cell marked by a red rectangle presenting lattice parameters of a = 27.96 Å, b=19.96 Å, and the inner angle of 90 °, which is consistent with experimental observations. Additionally, the simulated STM image calculated at bias of 100 mV shows the same morphology with the inset of experimental results which is also recorded at same bias, as shown in Figure 5.4d.

To explore the universality, the behavior of EABP molecule on Au(111) and Ag(100) substrate was also studied. The self-assembly structure on both substrates mostly appears as tetramer (cf. Figure 5.7 a, c), which perhaps results from a reduced reactivity of Au(111) and inherent four-fold symmetry of Ag(100). However, after O_2 treatment with same conditions (60 L at room temperature; 1L=1.33× 10^{-6} mbar·s) as on Ag(111), no dehydrogenation reaction happens on Au(111) and the EABP self-assembly structure remained intact (see Figure 5.7b). However, a disordered organometallic system is observed on Ag(100), ascribed to the dehydrogenative abstraction of the second H of amino groups and random connection with Ag atoms by deprotonated amino and alkynyl groups, as shown in Figure 5.7 d.

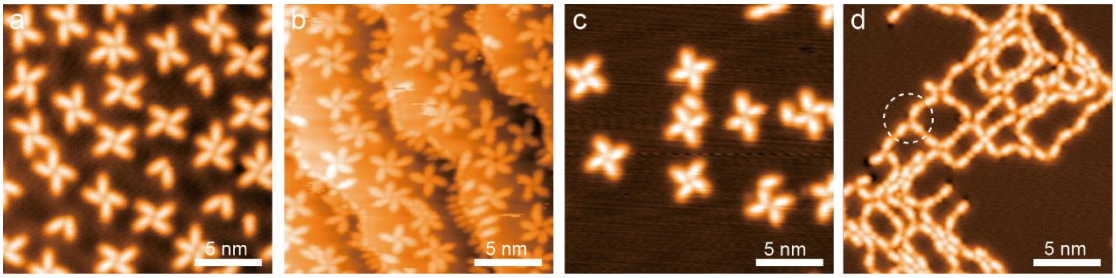

Figure 5.7: Molecule behavior on Au(111) and Ag(100) surface. (a) shows the EABP star-like self-assembly on Au(111). (b) reveals the similar assembly after exposing (a) in O_2 atmosphere at room temperature. (c) shows the similar EABP self-assembly structure on Ag(100) surface. (d) depicts the chain conformation after exposing (c) into O_2 atmosphere. Scanning parameters: V_b = 100 mV, I_t = 100 pA for (a); V_b = -1 V, I_t = 100 pA for (b); V_b = -100 mV, I_t = 1 nA (c) and (d).

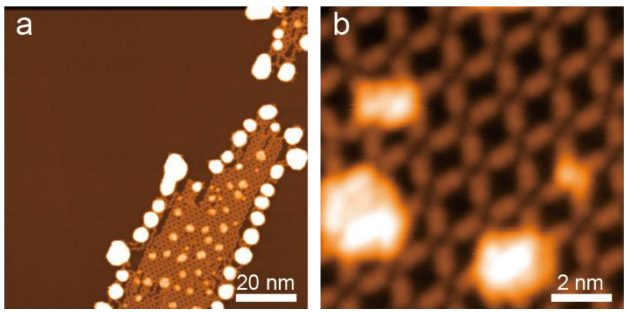

Figure 5.8: Large-area (a) and zoom-in (b) STM images of Cu deposition on EABP-Ag OMN. Scanning parameters: V_b = -500 mV, I_t = 1 nA for (a); V_b = -100 mV, I_t = 500 pA for (b).

For in-situ modifying the obtained EABP-Ag OMN on Ag(111), a transmetalation treatment was employed by dosing extrinsic copper atoms on EABP-Ag OMN held at room temperature, as shown in the large-area morphology images in Figure 5.8a. The bright islands are identified as the clusters of excessive Cu atoms. Despite this, the zoom-in images in Figure 5.8b reveals that the porous network already changed showing dim spots instead of bright protrusions at the position of metal center in C-M-N linkage. To achieve a more homogeneous distribution of Cu atoms, the initial phase was subjected to post-annealing treatment at 375 K.

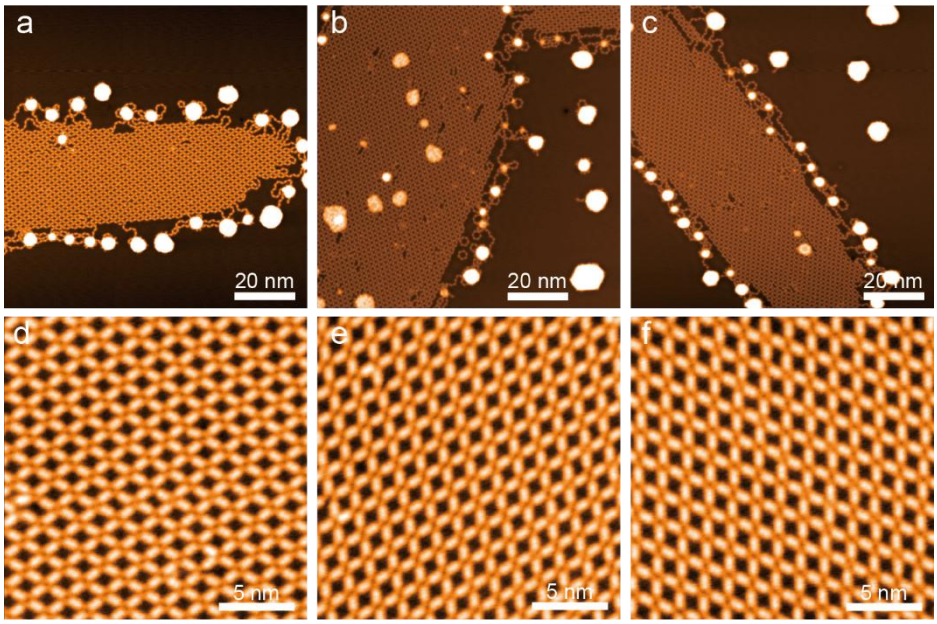

Figure 5.9: Large-area STM images (a), (b) and (c) of EABP-Cu OMN patches along with three orientations after annealing at 375 K. Corresponding zoom-in picture (d), (e) and (f) are in bottom row. Scanning parameters: V_b = -1 V, I_t = 100 pA for (a); V_b = -

500 mV, I_t = 100 pA for (b) and (c); V_b = -100 mV, I_t = 1 nA for (d), (e) and (f).

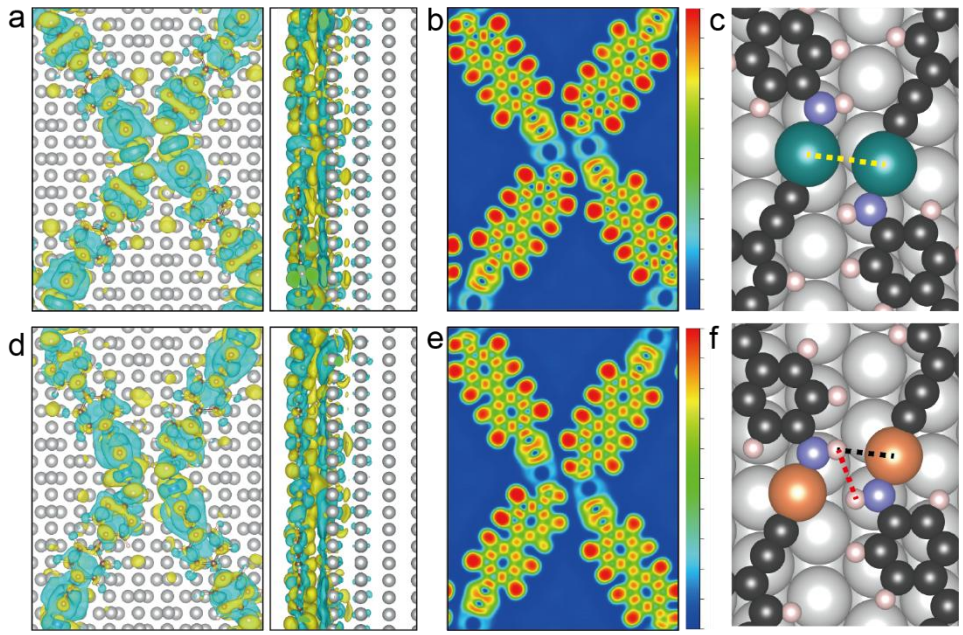

Figure 5.10: Top and side views of the charge transfer difference for (a) EABP-Ag OMN and (d) EABP-Cu OMN. Yellow and blue denotes the charge accumulation and depletion. Electron localization functions (ELF) mapping for (b) EABP-Ag OMN and (e) EABP-Cu OMN. (c) depicts the DFT-optimized unit cell of EABP-Ag OMN on Ag(111), within the length of Ag-Ag is marked by yellow dashline. (f) shows the DFT-optimized unit cell of EABP-Cu OMN on Ag(111), within the lengths of Cu···H and H···H are marked by black and red dashline, respectively.

As shown in Figure 5.9, a phenomenon was observed where excess Cu atoms preferentially diffused and accumulated at the periphery of the newly formed EABP-Cu OMN domains. This diffusion process resulted in a significantly cleaner internal structure of the OMN patches while maintaining the same orientation as observed in the original EABP-Ag OMN system. The high-resolution STM morphological image for EABP-Cu OMN is shown in Figure 5.4e. Following the transmetalation process, as previously discussed, the metal centers within the C-M-N linkage structure exhibit reduced contrast compared to the surrounding molecular moiety, in contrast to the observations made in the EABP-Ag OMN system. On the other hand, the distance of the Cu-Cu becomes larger. The unit cell of the EABP-Cu OMN, outlined by an orange rectangular frame in Figure 5.4e, exhibits lattice parameters of a = 26.4 ± 0.2 Å and b = 20.3 ± 0.2 Å, with an internal angle of 90 ± 1°. These structural parameters demonstrate that the transmetalation process preserves the overall periodic architecture

of the porous network with minimal structural alterations. The scheme of the transmetalation method from C-Ag-N to C-Cu-N linkage at room temperature on Ag(111) surface is shown in Figure 5.4f. The DFT-optimized structure, presented in Figure 5.4g, features a unit cell marked by red lines with lattice parameters of a = 26.13 Å and b = 19.93 Å, and an inner angle of 90°, demonstrating excellent agreement with experimental results. Moreover, the simulation of STM data with 100 mV bias is shown in Figure 5.4h, nicely matching experimental STM images as shown in the inset.

Crucially, the nature of interactions in both EABP-Ag and EABP-Cu OMNs need further detailed investigation. For the EABP-Ag system, the DFT-calculated Ag-Ag distance of 3.39 Å shows excellent agreement with experimental measurements (3.7 ± 0.4 Å), suggesting the existence of significant argentophilic interactions between adjacent OMCs.[169-171] Charge density difference analysis of the EABP-Ag OMN, performed using Bader charge analysis, indicates a charge transfer of 0.396 e from the Ag metal center to the surrounding carbon and nitrogen atoms, as illustrated in Figure 5.10a. Moreover, electron localization function (ELF) mapping analysis reveals that the transferred charge is primarily localized at the deprotonated alkynyl and amino functional groups, while exhibiting negligible charge localization at both the C-Ag and Ag-N bonding regions. This electronic distribution pattern aligns well with the characteristic features of organometallic bonding.[20, 162, 172]

Furthermore, the experimentally measured Cu-Cu distance of 5.8 ± 0.4 Å is larger than that of Ag-Ag pairs. This observation is supported by DFT calculations, which suggest a Cu-Cu separation of 4.5 Å - notably longer than the sum of the van der Waals radii of two Cu atoms (3.92 Å). These findings collectively demonstrate the absence of cuprophilic interactions in the system. In this context, the interaction between adjacent EABP-Cu OMCs originates from alternative mechanisms. Charge density difference analysis of the EABP-Cu OMN, combined with Bader charge analysis, reveals a significant charge transfer of 0.504 e from Cu atoms to the surrounding carbon and nitrogen atoms. Electron localization function (ELF) analysis further reveal that the charge is primarily localized on the molecular moieties rather than the metal centers. Notably, the remaining hydrogen atom of the amino groups accumulates substantial charge density, as illustrated in Figure 5.10f. The measured distances of 2.50 Å between the H atom and adjacent Cu atom, and 2.30 Å between two H atoms from neighboring amino groups, suggest that the assembly of EABP-Cu OMCs is governed by a combination of Cu···H electrostatic interactions and H···H bonding

Besides, the EABP molecule was also evaporated on Cu(111) surface directly, the self-

assembly structure is shown in Figure 5.11a and b. However, the disordered chain structure was obtained after post annealing at 375 K, without forming ordered and periodic porous network.

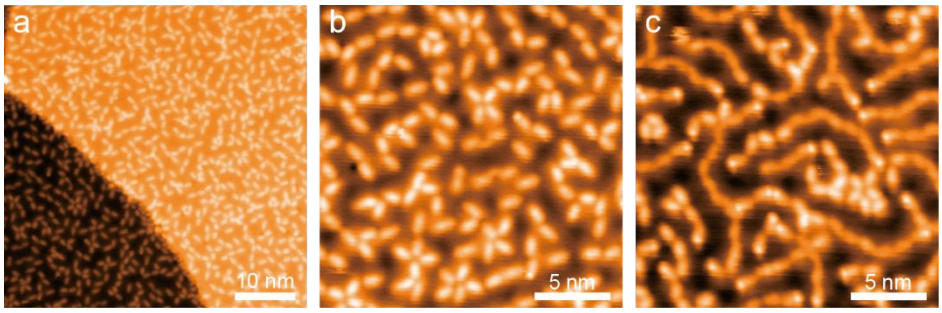

Figure 5.11: (a) and (b) STM images presenting the EABP self-assembly on Cu(111) surface. (c) depicts structure formation after subsequent annealing treatment. Scanning parameters: V_b = -1 V, I_t = 100 pA for (a); V_b = -100 mV, I_t = 50 pA for (b); V_b = -100 mV, I_t = 1 nA for (c).

The tip-manipulation was conducted to assess the interaction between the EABP-Ag and EABP-Cu OMCs, for characterizing the stability of OMNs. As shown in Figure 5.12, the EABP-Ag OMC are difficult to be separate using tip indicating a strong interaction within the adjacent OMCs. In contrast, adjacent EABP-Cu OMCs could be successfully separated through tip manipulation (cf. Figure 5.13), demonstrating weaker interactions than EABP-Ag counterparts. Besides, as evidenced in Figures 5.13e, f, the intramolecular connectivity within the EABP-Cu OMC remains intact following tip manipulation. Furthermore, the thermal stability of both OMNs was characterized via post-annealing at 425 K. As depicted in Figure 5.14, both porous networks started being decomposed. However, when the coverage is low, the EABP-Cu OMRs were obtained (cf. Figure 5.14c), which keep intact after annealing at 475 K, exhibiting higher thermal stability (cf. Figure 5.14d).

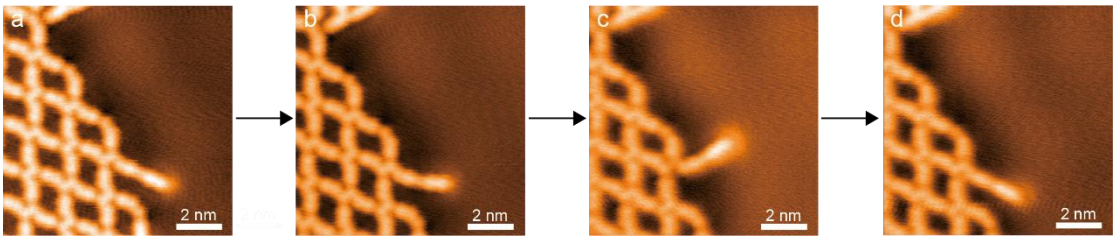

Figure 5.12: Tip-manipulation process performed on EABP-Ag OMC reveals strong interaction within adjacent chains. Scanning parameters: V_b = -100 mV, I_t = 500 pA for all STM images.

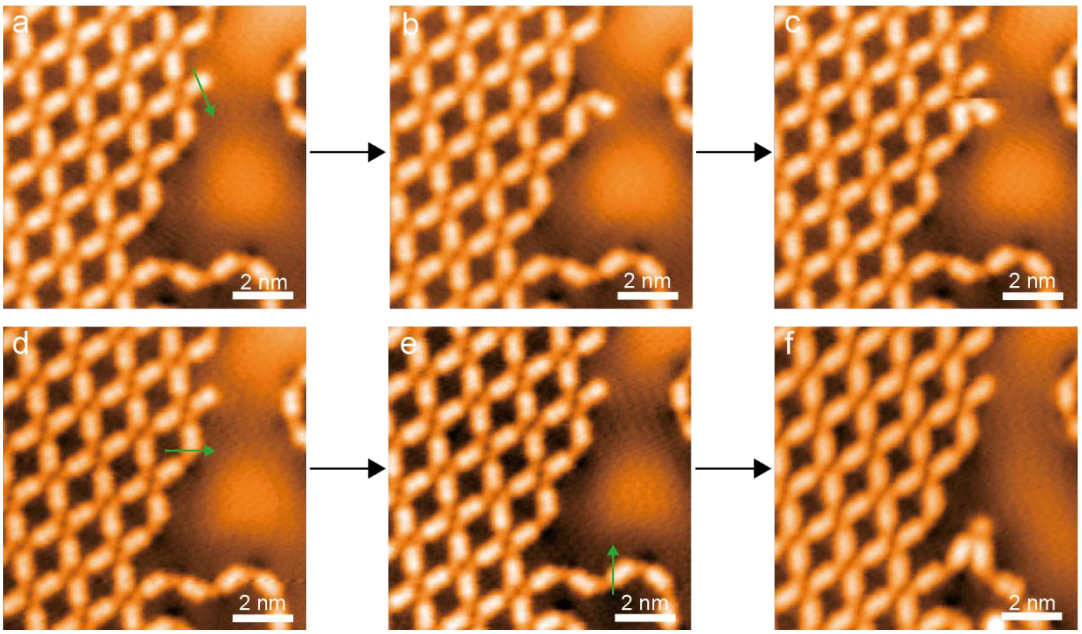

Figure 5.13: Tip-manipulation for EABP-Cu OMC. Scanning parameters: V_b = -10 mV, I_t = 1 nA for all STM images.

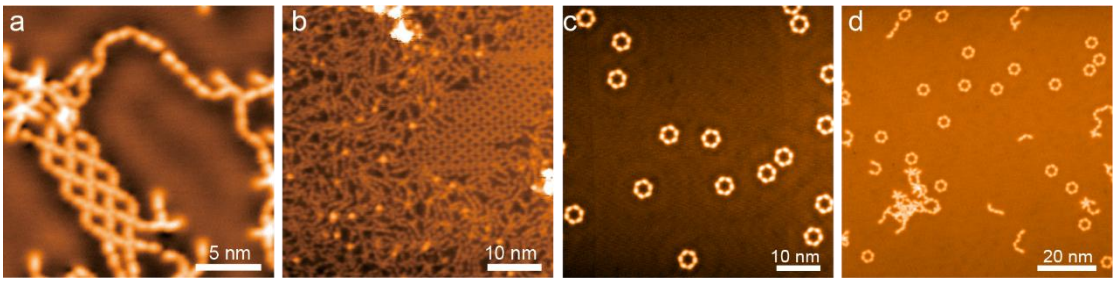

Figure 5.14: STM images for EABP-Ag (a) and EABP-Cu OMN (b) after annealing at 425 K for thermal stability characterization. (c) presents the STM images of EABP-Cu OMRs after annealing EABP-Cu OMN at 425 K when the coverage is low. (d) shows the OMRs keep intact after annealing at 475 K. Scanning parameters: V_b = -100 mV, I_t = 1 nA for (a); V_b = -1V, I_t = 20 pA for (b); *V_b = -500 mV, I_t = 100 pA for (c);* V_b = -1 V, I_t = 100 pA for (d);

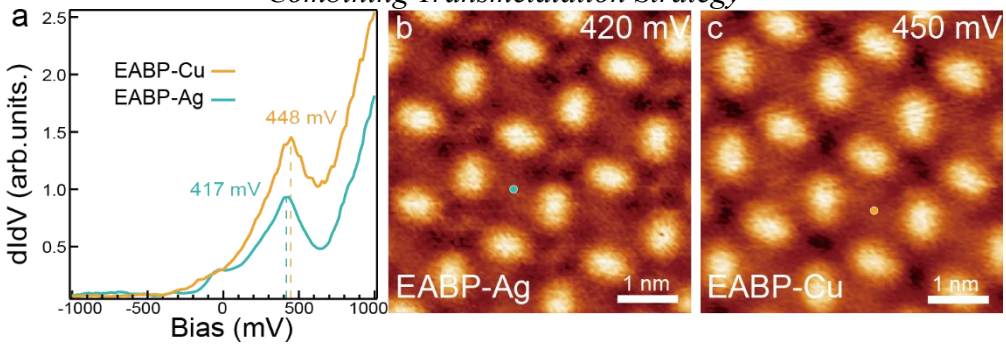

Figure 5.15: Surface state confinement in EABP-Ag and EABP-Cu OMN. (a) shows the experimental d*I*/d*V* spectra. (b) and (c) presents the dI/dV mapping of EABP-Ag and EABP-Cu OMN at 420 mV and 450 mV, respectively. The blue and yellow dots marked the tip position for STS spectra.

To further investigate the electronic properties of the synthesized EABP-Ag and EABP-Cu OMNs, we conducted STS measurements at the center of the pores (as marked in Figure 5.15b, c). As shown in Figure 5.15a, both networks exhibit characteristic quantum confinement states. Notably, the EABP-Cu OMN displays an upward shift of approximately 30 mV in its feature peak compared to the EABP-Ag OMN, which can be attributed to subtle variations in pore geometry.[78] This energy shift in the STS spectra provides additional proof supporting the successful transmetalation from C-Ag-N to C-Cu-N linkages. Figures 5.15b, c present d*I*/d*V* mappings acquired at 420 mV and 450 mV, respectively, in constant-height mode, corresponding to the characteristic STS peaks of both OMNs. These mappings reveal distinct spatial distributions of the electron density associated with the quantum confinement states. The corresponding current images are provided in Figures 5.16a, b, respectively. Additional bias-dependent STM images are documented in Figures 5.17 and 5.18, respectively, which show apparent confinement state geometry at 0.5 V for both OMNs. Moreover, as shown in Figure 5.17 and 5.18, the aromatic moiety of the molecule indicats a conspicuous state with the bias of 0.5V.

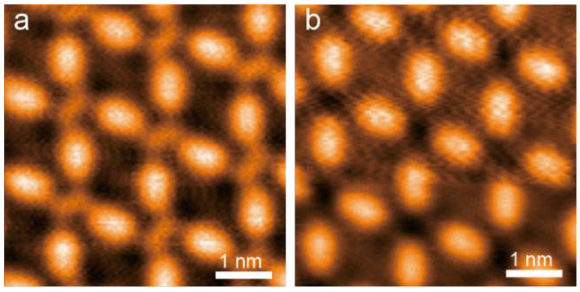

Figure 5.16: STM images with constant height mode for EABP-Ag (a) and EABP-Cu

OMN (b) by scanned with 420 mV and 450 mV.

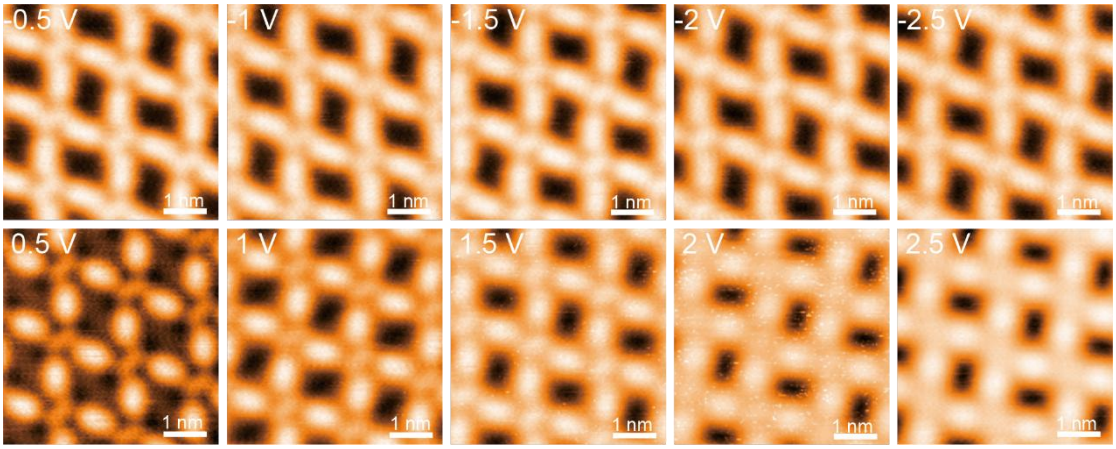

Figure 5.17: Bias-dependent STM images for EABP-Ag OMN. I_t = 1 nA

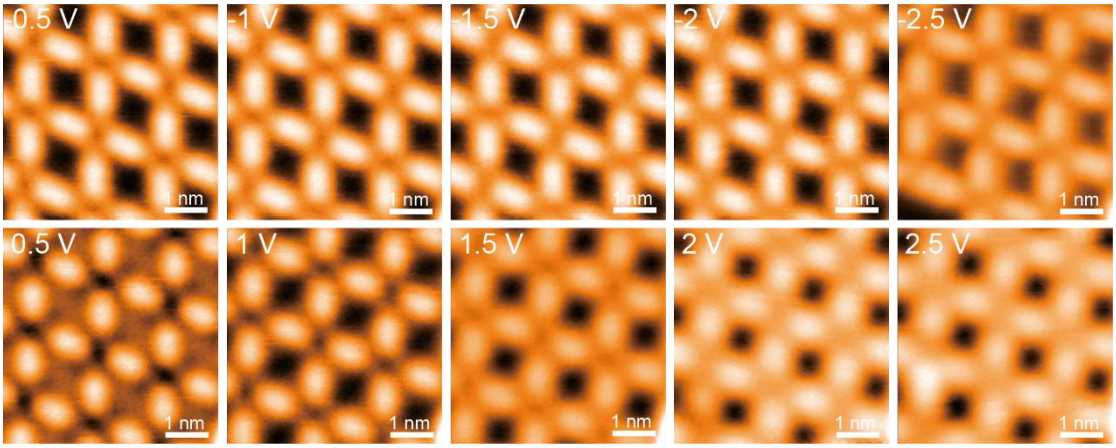

Figure 5.18: Bias-dependent STM images for EABP-Cu OMN. I_t = 1 nA

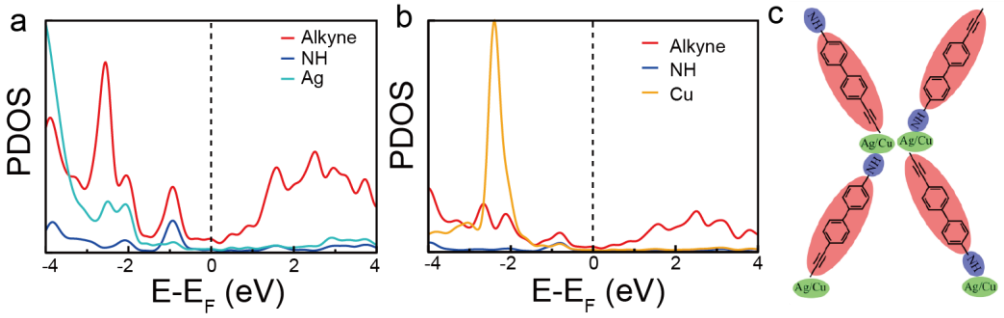

Figure 5.19: Projected density of states of (a) EABP-Ag OMN and (b) EABP-Cu OMN. (c) The red, purple, blue, and orange curves indicate the DOS projected on the alkyne with aromatic backbone, amino, silver and copper, respectively

To further elucidate the electronic structure, we calculated the projected density of states (PDOS) to identify the orbital contributions from different components within

the unit cells of both OMNs (cf. Figure 5.19). The analysis indicates that the primary electronic contribution originates from the aromatic moieties with alkynyl groups in both EABP-Ag and EABP-Cu systems. Furthermore, the contribution from Ag atoms in EABP-Ag OMN is significantly stronger than that from Cu atoms in EABP-Cu OMN, which explains the observed brighter appearance of Ag atoms compared to Cu atoms relative to other molecular components in the OMN structure, which is consistent with the bias-dependent images in Figure 5.17 and 5.18.

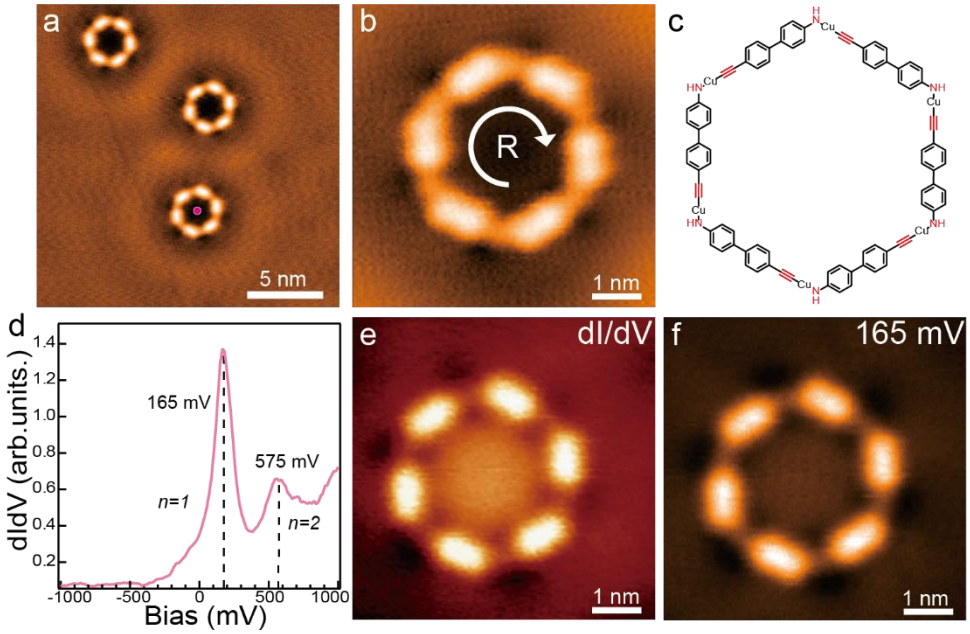

Figure 5.20: STM images and electronic properties of EABP-Cu OMRs. Panel (a) and (b) depict the STM images of EABP-Cu OMR. The pink dot in (a) denotes the tip position of STS measurement. The white circular arrow points the spin direction of the EABP-Cu OMR. (c) presents the chemical structure of the OMR from panel (b). The STS spectra of the OMR is shown in (d). (e) depicts the dI/dV mapping in constant height mode at bias of 165 mV. (f) shows the corresponding current images to (e). Scanning parameters: V_b = -100 mV, I_t = 100 pA for a; V_b = -10 mV, I_t = 1 nA for b; V_b = 165 mV, I_t = 1 nA for e and f.

Interestingly, followed by annealing at 425 K under low coverage conditions, the formation of EABP-Cu OMRs was observed, as demonstrated in Figure 5.20a (see Figure 5.14c for corresponding large-area image). High-resolution STM imaging revealed that all OMRs consist of six EABP molecules interconnected through C-Cu-N linkages, as clearly resolved in Figure 5.20b. Notably, the EABP-Cu OMRs exhibit intrinsic chirality, manifesting in two distinct enantiomers labeled as R and L in Figure

5.20b and Figure 5.21a. The corresponding chemical structure for Figure 5.20b is presented in Figure 5.20c. The electronic properties of the EABP-Cu OMR were investigated through STS measurements at the ring center, as indicated in Figure 5.20a. The tunneling spectra exhibit two distinct characteristic peaks centered at 165 mV and 575 mV, which correspond to quantum resonance states arising from surface stable confinement by localized potential variations induced by interfacial charge redistribution.[173, 174] For detailed analysis, constant-height dI/dV mapping at 165 mV is presented in Figure 5.20e, revealing a pronounced quantum resonance state within the ring. The corresponding current image is shown in Figure 5.20f. In rare instances, a unique dimeric structure formed by two incomplete rings was observed, as illustrated in Figure 5.21b.

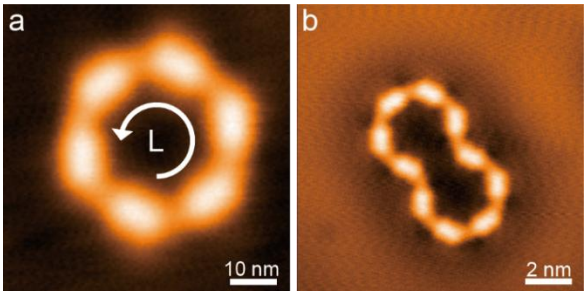

Figure 5.21: High-resolution STM images of EABP-Cu OMR. Scanning parameters: V_b = -500 mV, I_t = 300 pA for (a); V_b = -100 mV, I_t = 1 nA for (b).

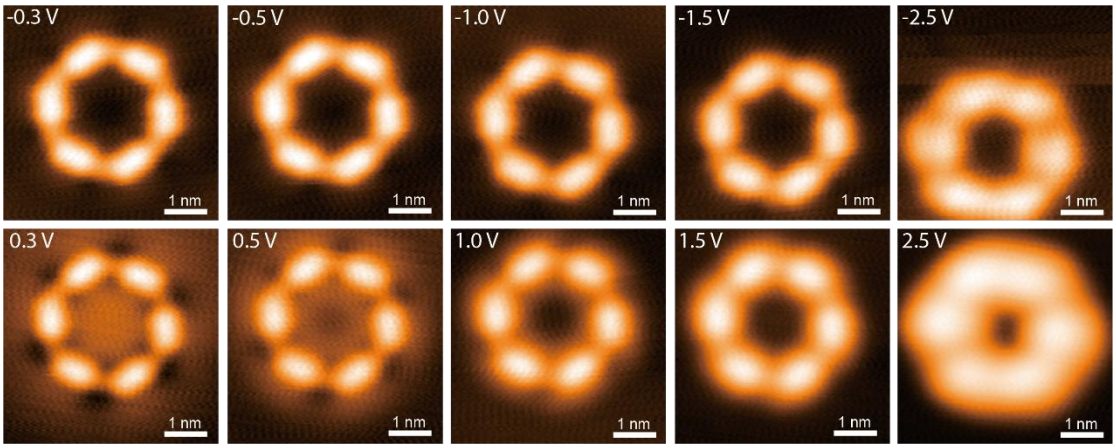

Figure 5.22: Bias-dependent STM images of EABP-Cu OMR. I_t = 1 nA

Bias-dependent STM images presented in Figure 5.22 further demonstrate the electronic characteristics, with the 300 mV and 500 mV bias images clearly indicating quantum resonances with a circular and a distinctive donut-shaped profile.

Conclusion

In conclusion, we have successfully fabricated dinuclear EABP-Ag OMN on Ag(111) through a gas-mediated synthesis strategy. Subsequently, well-ordered EABP-Cu OMN with similar periodicity was achieved via transmetalation by depositing extrinsic Cu atoms onto the EABP-Ag OMN, followed by thermal annealing at 375 K. Stability studies revealed that both OMNs initiate decomposition at 425 K, while EABP-Cu showing weaker interaction between adjacent OMCs. Thus, under low-coverage conditions, EABP-Cu OMRs formed and exhibited enhanced thermal stability, remaining intact up to 475 K. The electronic properties of both EABP-Ag/Cu OMNs and EABP-Cu OMRs were systematically investigated through STS. The analysis revealed surface states confinement at 448 mV for EABP-Cu OMN, showing an approximately 30 mV upward shift compared to the 417 mV state observed in EABP-Ag OMN. Furthermore, the EABP-Cu OMR exhibited two distinct quantum resonance states at 165 mV and 575 mV. Detailed DFT calculations, including charge density difference and ELF mapping analyses, provided insights into the interactions within these structures. The EABP-Ag OMN formation is primarily driven by argentophilic interactions between adjacent EABP-Ag OMCs, while the assembly of EABP-Cu OMN is governed by a combination of electrostatic interactions and hydrogen bonding between neighboring EABP-Cu OMCs

6. Conclusions and outlook

In this thesis, employing STM, STS, XPS and LEED for a molecular-level insight, we focus on engineering functional nano-architectures by the control of functional molecules on surface incorporating metal additions which were either intrinsically provided by the employed substrate or evaporated thereon under UHV conditions. Specifically, we investigated the reactivity of amino on Ag and Au substrates and the construction of single-atom layer OMNs using amino- and alkynyl-terminated molecular precursors through O_2-mediated dehydrogenation reaction. Additionally, we explored the tuning of OMN properties by integrating a transmetalation strategy on surfaces. Computational modeling was utilized to aid multi-technique studies and data interpretation.

Firstly, the O_2-mediated treatment effectively promotes the oxidative dehydrogenation of amino groups in aromatic amines, leading to the formation of organometallic nanopores on Ag(111) and Ag(100) surfaces. However, this process is hindered on Au(111). Systematic STM and XPS experiments, combined with complementary DFT calculations, demonstrate that the O_2 treatment significantly enhances the reactivity of aromatic amines by lowering the energy barrier compared to activation in the absence of O_2. Our findings reveal that the chemisorption of O_2 is the rate-limiting step in the dehydrogenation reaction, which is thermodynamically much less favorable on Au(111) than on Ag(111).

Secondly, we explored the modification of a surface-confined single-layer OMN through transmetalation, specifically converting an alkynyl-Ag-alkynyl to an alkynyl-Cu-alkynyl linking platform via a post-synthetic reaction. By depositing Cu adatoms on extended organometallic Ag-TEB networks and thermally annealing to an appropriate temperature, we achieved the distinct transformation of Ag-TEB into Cu-TEB OMN. The resulting Cu-TEB structure exhibits higher thermal stability while retaining similar lattice periodicity and pore symmetry as the Ag-TEB OMN.

Thirdly, we successfully fabricated dinuclear EABP-Ag OMN on Ag(111) using a gas-mediated synthesis strategy. Subsequently, a well-ordered EABP-Cu OMN with similar periodicity was achieved through transmetalation by depositing extrinsic Cu atoms onto the EABP-Ag OMN, followed by thermal annealing at 375 K. Stability studies revealed that both OMNs begin decomposing at 425 K, with EABP-Cu exhibiting weaker interactions between adjacent OMCs. Under low-coverage conditions, EABP-Cu OMRs formed and demonstrated enhanced thermal stability, remaining intact up to 475 K. The electronic properties of EABP-Ag/Cu OMNs and EABP-Cu OMRs were systematically investigated using STS. The analysis revealed a confined surface state at 448 mV for EABP-Cu OMN, showing an approximately 30 mV upward shift compared to the 417 mV state observed in EABP-Ag OMN. Additionally, the EABP-Cu OMR exhibited two distinct quantum resonance states at 165 mV and 575 mV. Detailed DFT calculations, including charge density difference and ELF mapping analyses, provided insights into the interactions within these structures. The formation of EABP-Ag OMN is primarily driven by argentophilic interactions between adjacent EABP-Ag OMCs, while the assembly of EABP-Cu OMN is governed by a combination of electrostatic interactions and hydrogen bonding between neighboring EABP-Cu OMCs.

In summary, this thesis provides systematic studies on the construction of OMNs on surfaces, using amino and alkynyl groups as the main components of the linkage. The applied strategies, including gas-mediated synthesis and transmetalation methods, have been explored, enriching the toolbox of bottom-up approaches for fabricating low-dimensional OMNs on surfaces. Furthermore, the fundamental principles of transmetalation on surfaces require further exploration in the future. This will enhance the capability to construct functional OMNs on diverse substrates, such as transition metal dichalcogenides, graphene, and others, potentially bestowing intriguing properties to the target materials.

List of publications

1. **W. Zhao**,# F. Haag,#, I. Piquero-Zulaiac,* Z. M. Abd El-Fattah, P. Pendem, P. V. Vicente, Y-Q. Zhang, N. Cao, A. P. Seitsonen, F. Allegretti,* B. Yang,* J. V. Barth. Transmetalation in Surface-Confined Single-Layer Organometallic Networks withAlkynyl−Metal−Alkynyl Linkages. *ACS Nano*, 2024,18, 20157-20166. (# equal contribution)

2. N. Cao,# **W. Zhao**,# K. Niu,# F. Haag, F. Allegretti, J. Rosen, J. Björk,* L. Chi,* J. V. Barth, B. Yang,* Substrate-Dependent Reactivity of Aromatic Amines under O_2 Exposure on Metal Surfaces. Submitted (# equal contribution)

3. F. Haag, **W. Zhao**, B. Yang, P. Knecht, K. Seufert, M. G. Cuxart, A. C. Papageorgiou, M. Muntwiler, W. Auwärter, C. R. Hess*, J. V. Barth, F. Allegretti.* Selective On-Surface Metalation and Uncommon Reordering of Self-Assembled Macrocyclic Biquinazoline Ligands on Ag(111). *Chem. Eur. J.*, 2025, 31, e202404350.

4. P. V. Vicente,* T. Weiss, D. Meier, **W. Zhao**, B. S. Tömekçe, M. G. Cuxart, B. P. Klein, D. A. Duncan, T-L. Lee, A. C. Papageorgiou, M. Muntwiler, A. P. Seitsonen, W. Auwärter, P. Feulner, J. V. Barth, F. Allegretti.* Holistic Structural Understanding of Epitaxially-Grown Bi/Au (111) Moiré Superstructures. *Phy. Rev. M*., 2024, 8, 104001.

5. B. Yang,* K. Niu, N. Cao, N. Grover, **W. Zhao**, A. Riss, J. Björk,* W. Auwärter, J. V. Barth,* M. O. Senge.* On-Surface Synthesis of Polyphenylene Wires Comprising Rigid Aliphatic Bicyclo[1.1.1]Pentane Isolator Units. *Angew. Chem.Int. Ed*., 2023, 62, e202218211.

6. J. Wang, K. Niu, H. Zhu, C. Xu, C. Deng, **W. Zhao**, P. Huang, H. Lin, D. Li, J.

Rosen, P. Liu, F. Allegretti, J. V. Barth, B. Yang,* J. Björk,* Q. Li,* L. Chi.* Universal Inter-Molecular Radical Transfer Reactions on Metal Surfaces. *Nat. Commun.,* 2024, 15, 3030.

7. W. Zhao, C. Kaderoğlu, E. Aktürk, M. O. Senge, B. Yang,* J. V. Barth. On-Surface Synthesis of Tunable Dinuclear Organometallic Networks Combining Transmetalation Strategy. *To be submitted*.

8. W. Zhao, J. Liu, B. Yang, Z. Liu, Y. Wang, H. Brune, I. Piquero-Zulaiac,* J. V. Barth.* On-surface synthesis on VSe_2 substrate. *To be submitted.*

9. W. Zhao, N. Cao, B. Kretz, D. Egger, B. Yang,* J. V. Barth. Constructing regular two-dimensional tessellation via bromine bonding on Ag (100) surface. *To be submitted.*

Bibliography

1. Liu, X.; Hersam, M. C., 2D Materials for Quantum Information Science. *Nature Reviews Materials* **2019,** *4* (10), 669-684.
2. Yu, S.; Wu, X.; Wang, Y.; Guo, X.; Tong, L., 2D Materials for Optical Modulation: Challenges and Opportunities. *Advanced Materials* **2017,** *29* (14), 1606128.
3. Mannix, A. J.; Kiraly, B.; Hersam, M. C.; Guisinger, N. P., Synthesis and Chemistry of Elemental 2D Materials. *Nature Reviews Chemistry* **2017,** *1* (2), 0014.
4. Anichini, C.; Czepa, W.; Pakulski, D.; Aliprandi, A.; Ciesielski, A.; Samorì, P., Chemical Sensing with 2D Materials. *Chemical Society Reviews* **2018,** *47* (13), 4860-4908.
5. Ares, P.; Novoselov, K. S., Recent Advances in Graphene and Other 2D Materials. *Nano Materials Science* **2022,** *4* (1), 3-9.
6. Lemme, M. C.; Akinwande, D.; Huyghebaert, C.; Stampfer, C., 2D Materials for Future Heterogeneous Electronics. *Nature Communications* **2022,** *13* (1), 1392.
7. Dhakshinamoorthy, A.; Asiri, A. M.; Garcia, H., 2D Metal–Organic Frameworks as Multifunctional Materials in Heterogeneous Catalysis and Electro/Photocatalysis. *Advanced Materials* **2019,** *31* (41), 1900617.
8. Xie, Y.; Wu, X.; Shi, Y.; Peng, Y.; Zhou, H.; Wu, X.; Ma, J.; Jin, J.; Pi, Y.; Pang, H., Recent Progress in 2D Metal-Organic Framework-Related Materials. *Small* **2024,** *20* (1), 2305548.
9. Xiong, D.; Deng, X.; Cao, Z.; Tao, S.; Song, Z.; Xiao, X.; Deng, W.; Hou, H.; Zou, G.; Ji, X., 2D Metal–Organic Frameworks for Electrochemical Energy Storage. *ENERGY & ENVIRONMENTAL MATERIALS* **2023,** *6* (6), e12521.
10. Yao, M.-S.; Xiu, J.-W.; Huang, Q.-Q.; Li, W.-H.; Wu, W.-W.; Wu, A.-Q.; Cao, L.-A.; Deng, W.-H.; Wang, G.-E.; Xu, G., Van der Waals Heterostructured MOF-on-MOF Thin Films: Cascading Functionality to Realize Advanced Chemiresistive Sensing. *Angewandte Chemie International Edition* **2019,** *58* (42), 14915-14919.
11. Fan, H.; Peng, M.; Strauss, I.; Mundstock, A.; Meng, H.; Caro, J., MOF-in-COF Molecular Sieving Membrane for Selective Hydrogen Separation. *Nature Communications* **2021,** *12* (1), 38.
12. Chakraborty, G.; Park, I.-H.; Medishetty, R.; Vittal, J. J., Two-Dimensional

Metal-Organic Framework Materials: Synthesis, Structures, Properties and Applications. *Chemical Reviews* **2021,** *121* (7), 3751-3891.

13. Zhang, M.; Feng, G.; Song, Z.; Zhou, Y.-P.; Chao, H.-Y.; Yuan, D.; Tan, T. T. Y.; Guo, Z.; Hu, Z.; Tang, B. Z.; Liu, B.; Zhao, D., Two-Dimensional Metal–Organic Framework with Wide Channels and Responsive Turn-On Fluorescence for the Chemical Sensing of Volatile Organic Compounds. *Journal of the American Chemical Society* **2014,** *136* (20), 7241-7244.

14. Barth, J. V., Fresh Perspectives for Surface Coordination Chemistry. *Surface Science* **2009,** *603* (10), 1533-1541.

15. Stepanow, S.; Lin, N.; Barth, J. V.; Kern, K., Surface-Template Assembly of Two-Dimensional Metal−Organic Coordination Networks. *The Journal of Physical Chemistry B* **2006,** *110* (46), 23472-23477.

16. Li, Y.; Lv, J.; Li, S.; Dai, L.; Wang, B.; Li, P., In situ Post-Modification of Substoichiometric 2D Conjugated Mofs to Boost Ethylene Selectivity in Electrocatalytic CO_2 Reduction. *Journal of Materials Chemistry A* **2024,** *12* (36), 24549-24555.

17. Parshamoni, S.; Nasani, R.; Paul, A.; Konar, S., Synthesis of a Palladium Based MOF via an Effective Post-Synthetic Modification Approach and its Catalytic Activity Towards Heck Type Coupling Reactions. *Inorganic Chemistry Frontiers* **2021,** *8* (3), 693-699.

18. Zhong, W.; Zhang, T.; Chen, D.; Su, N.; Miao, G.; Guo, J.; Chen, L.; Wang, Z.; Wang, W., Synthesizing Cr-Based Two-Dimensional Conjugated Metal-Organic Framework Through On-Surface Substitution Reaction. *Small* **2023**, 2207877.

19. Eichhorn, J.; Strunskus, T.; Rastgoo-Lahrood, A.; Samanta, D.; Schmittel, M.; Lackinger, M., On-surface Ullmann Polymerization *via* Intermediate Organometallic Networks on Ag(111). *Chem. Commun.* **2014,** *50* (57), 7680-7682.

20. Yang, Z.; Gebhardt, J.; Schaub, T. A.; Sander, T.; Schönamsgruber, J.; Soni, H.; Görling, A.; Kivala, M.; Maier, S., Two-dimensional Delocalized States in Organometallic Bis-acetylide Networks on Ag(111). *Nanoscale* **2018,** *10* (8), 3769-3776.

21. Zhang, Y.-Q.; Paintner, T.; Hellwig, R.; Haag, F.; Allegretti, F.; Feulner, P.; Klyatskaya, S.; Ruben, M.; Seitsonen, A. P.; Barth, J. V.; Klappenberger, F., Synthesizing Highly Regular Single-Layer Alkynyl–Silver Networks at the Micrometer Scale via Gas-Mediated Surface Reaction. *Journal of the American Chemical Society* **2019,** *141* (13), 5087-5091.

22. Binnig, G.; Rohrer, H.; Gerber, C.; Weibel, E., Surface Studies by Scanning Tunneling Microscopy. *Physical Review Letters* **1982,** *49* (1), 57-61.

23. Hund, F., Zur Deutung der Molekelspektren. III. *Zeitschrift für Physik* **1927,** *43* (11), 805-826.

24. Bardeen, J., Tunnelling from a Many-Particle Point of View. *Physical Review Letters* **1961,** *6* (2), 57-59.

25. Tersoff, J.; Hamann, D. R., Theory of the Scanning Tunneling Microscope.

Physical Review B **1985,** *31* (2), 805-813.
26. Selloni, A.; Carnevali, P.; Tosatti, E.; Chen, C. D., Voltage-dependent Scanning-Tunneling Microscopy of a Crystal Durface: Graphite. *Physical Review B* **1985,** *31* (4), 2602-2605.
27. Hertz, H., Ueber einen Einfluss des ultravioletten Lichtes auf die electrische Entladung. *Annalen der Physik* **1887,** *267* (8), 983-1000.
28. Einstein, A., Über einen die Erzeugung und Verwandlung des Lichtes betreffenden heuristischen Gesichtspunkt. *Annalen der Physik* **1905,** *322* (6), 132-148.
29. Alford, T. L.; Feldman, L. C.; Mayer, J. W., *Fundamentals of nanoscale film analysis*. Springer Science & Business Media: 2007.
30. Paintner, T. Novel Reaction Pathways through On-Surface Conditions: Tunneling-mediated Hydroalkoxylation and Gas-induced Deprotonation. Technische Universität München, 2019.
31. Krenner, W. B. Supramolecular Templates: Routes Towards Steering Assembly and Electronic Properties at the Nanoscale. Technische Universität München, 2012.
32. GmbH, C. Heuserweg 14, 53842 Troisdorf (DE), url: http://www.cryovac.de.
33. Zhang, L.; Miyamachi, T.; Tomanić, T.; Dehm, R.; Wulfhekel, W., A compact sub-Kelvin ultrahigh vacuum scanning tunneling microscope with high energy resolution and high stability. *Review of Scientific Instruments* **2011,** *82* (10), 103702.
34. SPECS GmbH, V., 13355 Berlin (DE), http://www.specs.de/cms/upload/PDFs/SPECS_Prospekte/2010_02_JT-STM_brochure_final_web.
35. Haag, F. M. Atomic Level Studies of the Surface-Directed Synthesis of Novel Organometallic and Metal-Organic Two-Dimensional Assemblies. Technische Universität München, 2022.
36. L. Guglialmelli, M. R. F., *An. Asoc. Quim. Argent* **1931,** (19), 5-33.
37. Xie, J.; Seto, C. T., A Two Stage Click-based Library of Protein Tyrosine Phosphatase Inhibitors. *Bioorganic & Medicinal Chemistry* **2007,** *15* (1), 458-473.
38. Horcas, I.; Fernández, R.; Gómez-Rodríguez, J. M.; Colchero, J.; Gómez-Herrero, J.; Baro, A. M., WSXM: A Software for Scanning Probe Microscopy and a Tool For Nanotechnology. *Review of Scientific Instruments* **2007,** *78* (1), 013705.
39. Fairley, N.; Fernandez, V.; Richard-Plouet, M.; Guillot-Deudon, C.; Walton, J.; Smith, E.; Flahaut, D.; Greiner, M.; Biesinger, M.; Tougaard, S.; Morgan, D.; Baltrusaitis, J., Systematic and Collaborative Approach to Problem Solving Using X-Ray Photoelectron Spectroscopy. *Applied Surface Science Advances* **2021,** *5*, 100112.
40. Hermann , K. V. H., M. A. Software Utility LEEDpat (Version 4.2); Fritz Haber Institute: https://www.fhi.mpg.de/958975/LEEDpat4.
41. Kresse, G.; Furthmüller, J., Efficient Iterative Schemes for Ab Initio Total-Energy Calculations Using a Plane-Wave Basis Set. *Physical Review B* **1996,** *54* (16), 11169-11186.
42. Blöchl, P. E., Projector Augmented-Wave Method. *Physical Review B* **1994,** *50* (24), 17953-17979.

43. Hamada, I., van der Waals Density Functional Made Accurate. *Physical Review B* **2014,** *89* (12), 121103.
44. Björk, J.; Stafström, S., Adsorption of Large Hydrocarbons on Coinage Metals: A van der Waals Density Functional Study. *ChemPhysChem* **2014,** *15* (13), 2851-2858.
45. Chen, L.; Rosen, J.; Björk, J., A Density Functional Benchmark for Dehydrogenation and Dehalogenation Reactions on Coinage Metal Surfaces. *ChemPhysChem* **2025,** *26* (1), e202400865.
46. Henkelman, G.; Jónsson, H., Improved Tangent Estimate in the Nudged Elastic Band Method for Finding Minimum Energy Paths and Saddle Points. *The Journal of Chemical Physics* **2000,** *113* (22), 9978-9985.
47. Henkelman, G.; Jónsson, H., A Dimer Method for Finding Saddle Points on High Dimensional Potential Surfaces Using Only First Derivatives. *The Journal of Chemical Physics* **1999,** *111* (15), 7010-7022.
48. Lorente, N.; Persson, M., Theoretical Aspects of Tunneling-Current-Induced Bond Excitation and Breaking at Surfaces. *Faraday Discussions* **2000,** *117* (0), 277-290.
49. VandeVondele, J.; Krack, M.; Mohamed, F.; Parrinello, M.; Chassaing, T.; Hutter, J., Quickstep: Fast and Accurate Density Functional Calculations Using a Mixed Gaussian and Plane Waves Approach. *Computer Physics Communications* **2005,** *167* (2), 103-128.
50. Perdew, J. P.; Burke, K.; Ernzerhof, M., Generalized Gradient Approximation Made Simple. *Physical Review Letters* **1996,** *77* (18), 3865-3868.
51. Grimme, S.; Antony, J.; Ehrlich, S.; Krieg, H., A Consistent and Accurate Ab Initio Parametrization of Density Functional Dispersion Correction (DFT-D) for the 94 Elements H-Pu. *The Journal of Chemical Physics* **2010,** *132* (15), 154104.
52. Goedecker, S.; Teter, M.; Hutter, J., Separable Dual-Space Gaussian Pseudopotentials. *Physical Review B* **1996,** *54* (3), 1703-1710.
53. VandeVondele, J.; Hutter, J., Gaussian Basis Sets for Accurate Calculations on Molecular Systems in Gas and Condensed Phases. *The Journal of Chemical Physics* **2007,** *127* (11), 114105.
54. Kohn, W.; Sham, L. J., Self-Consistent Equations Including Exchange and Correlation Effects. *Physical Review* **1965,** *140* (4A), A1133-A1138.
55. Hohenberg, P.; Kohn, W., Inhomogeneous Electron Gas. *Physical Review* **1964,** *136* (3B), B864-B871.
56. Kresse, G.; Hafner, J., Ab Initio Molecular-Dynamics Simulation of the Liquid-Metal--Amorphous-Semiconductor Transition In Germanium. *Physical Review B* **1994,** *49* (20), 14251-14269.
57. Kresse, G.; Hafner, J., Ab Initio Molecular Dynamics for Liquid Metals. *Physical Review B* **1993,** *47* (1), 558-561.
58. Kresse, G.; Furthmüller, J., Efficiency of Ab-Initio Total Energy Calculations for Metals and Semiconductors Using a Plane-Wave Basis Set. *Computational Materials Science* **1996,** *6* (1), 15-50.

59. Grimme, S., Semiempirical GGA-type Density Functional Constructed with a Long-range Dispersion Correction. *Journal of Computational Chemistry* **2006,** *27* (15), 1787-1799.
60. Monkhorst, H. J.; Pack, J. D., Special Points for Brillouin-zone integrations. *Physical Review B* **1976,** *13* (12), 5188-5192.
61. Henkelman, G.; Arnaldsson, A.; Jónsson, H., A Fast and Robust Algorithm for Bader Decomposition of Charge Density. *Computational Materials Science* **2006,** *36* (3), 354-360.
62. Momma, K.; Izumi, F., VESTA 3 for Three-dimensional Visualization of Crystal, Volumetric and Morphology Data. *Journal of Applied Crystallography* **2011,** *44* (6), 1272-1276.
63. Pereira, L.; Mondal, P. K.; Alves, M., Aromatic Amines Sources, Environmental Impact and Remediation. In *Pollutants in Buildings, Water and Living Organisms*, Lichtfouse, E.; Schwarzbauer, J.; Robert, D., Eds. Springer International Publishing: Cham, 2015; pp 297-346.
64. Edebali, Ö.; Krupčíková, S.; Goellner, A.; Vrana, B.; Muz, M.; Melymuk, L., Tracking Aromatic Amines from Sources to Surface Waters. *Environmental Science & Technology Letters* **2024,** *11* (5), 397-409.
65. Li, X.; Xu, Z.; Bu, D.; Cai, J.; Chen, H.; Chen, Q.; Chen, T.; Cheng, F.; Chi, L.; Dong, W.; Dong, Z.; Du, S.; Fan, Q.; Fan, X.; Fu, Q.; Gao, S.; Guo, J.; Guo, W.; He, Y.; Hou, S.; Jiang, Y.; Kong, H.; Li, B.; Li, D.; Li, J.; Li, Q.; Li, R.; Li, S.; Lin, Y.; Liu, M.; Liu, P.; Liu, Y.; Lü, J.; Ma, C.; Pan, H.; Pan, J.; Pan, M.; Qiu, X.; Shen, Z.; Tan, S.; Wang, B.; Wang, D.; Wang, L.; Wang, L.; Wang, T.; Wang, X.; Wang, X.; Wang, X.; Wang, Y.; Wang, Y.; Wu, K.; Xu, W.; Xue, N.; Yan, L.; Yang, F.; Yang, Z.; Zhang, C.; Zhang, X.; Zhang, Y.; Zhang, Y.; Zhou, X.; Zhu, J.; Zhang, Y.; Gao, F.; Wang, Y., Recent Progress on Surface Chemistry II: Property and Characterization. *Chinese Chemical Letters* **2024**, 110100.
66. Grill, L.; Hecht, S., Covalent On-Surface Polymerization. *Nature Chemistry* **2020,** *12* (2), 115-130.
67. Shen, Q.; Gao, H.-Y.; Fuchs, H., Frontiers of On-Surface Synthesis: From Principles to Applications. *Nano Today* **2017,** *13*, 77-96.
68. Clair, S.; de Oteyza, D. G., Controlling a Chemical Coupling Reaction on a Surface: Tools and Strategies for On-Surface Synthesis. *Chemical Reviews* **2019,** *119* (7), 4717-4776.
69. Yang, B.; Dong, B.; Chi, L., On-Surface Intramolecular Reactions. *ACS Nano* **2020,** *14* (6), 6376-6382.
70. Cai, J.; Ruffieux, P.; Jaafar, R.; Bieri, M.; Braun, T.; Blankenburg, S.; Muoth, M.; Seitsonen, A. P.; Saleh, M.; Feng, X.; Müllen, K.; Fasel, R., Atomically Precise Bottom-up Fabrication of Graphene Nanoribbons. *Nature* **2010,** *466* (7305), 470-473.
71. Moreno, C.; Vilas-Varela, M.; Kretz, B.; Garcia-Lekue, A.; Costache, M. V.; Paradinas, M.; Panighel, M.; Ceballos, G.; Valenzuela, S. O.; Peña, D.; Mugarza, A., Bottom-up Synthesis of Multifunctional Nanoporous Graphene. *Science* **2018,** *360*

(6385), 199-203.
72. Lackinger, M., Surface-assisted Ullmann Coupling. *Chemical Communications* **2017,** *53* (56), 7872-7885.
73. Cirera, B.; Zhang, Y.-Q.; Björk, J.; Klyatskaya, S.; Chen, Z.; Ruben, M.; Barth, J. V.; Klappenberger, F., Synthesis of Extended Graphdiyne Wires by Vicinal Surface Templating. *Nano Letters* **2014,** *14* (4), 1891-1897.
74. Klappenberger, F.; Hellwig, R.; Du, P.; Paintner, T.; Uphoff, M.; Zhang, L.; Lin, T.; Moghanaki, B. A.; Paszkiewicz, M.; Vobornik, I.; Fujii, J.; Fuhr, O.; Zhang, Y. Q.; Allegretti, F.; Ruben, M.; Barth, J. V., Functionalized Graphdiyne Nanowires: On-Surface Synthesis and Assessment of Band Structure, Flexibility, and Information Storage Potential. *Small* **2018,** *14* (14), 1704321.
75. Cao, N.; Yang, B.; Riss, A.; Rosen, J.; Björk, J.; Barth, J. V., On-surface Synthesis of Enetriynes. *Nature Communications* **2023,** *14* (1).
76. Zhou, H.; Liu, J.; Du, S.; Zhang, L.; Li, G.; Zhang, Y.; Tang, B. Z.; Gao, H.-J., Direct Visualization of Surface-Assisted Two-Dimensional Diyne Polycyclotrimerization. *Journal of the American Chemical Society* **2014,** *136* (15), 5567-5570.
77. Liu, J.; Ruffieux, P.; Feng, X.; Müllen, K.; Fasel, R., Cyclotrimerization of Arylalkynes on Au(111). *Chem. Commun.* **2014,** *50* (76), 11200-11203.
78. Zhao, W.; Haag, F.; Piquero-Zulaica, I.; Abd El-Fattah, Z. M.; Pendem, P.; Vezzoni Vicente, P.; Zhang, Y.-Q.; Cao, N.; Seitsonen, A. P.; Allegretti, F.; Yang, B.; Barth, J. V., Transmetalation in Surface-Confined Single-Layer Organometallic Networks with Alkynyl–Metal–Alkynyl Linkages. *ACS Nano* **2024,** *18* (31), 20157-20166.
79. Chen, C.; Joshi, T.; Li, H.; Chavez, A. D.; Pedramrazi, Z.; Liu, P.-N.; Li, H.; Dichtel, W. R.; Bredas, J.-L.; Crommie, M. F., Local Electronic Structure of a Single-Layer Porphyrin-Containing Covalent Organic Framework. *ACS Nano* **2018,** *12* (1), 385-391.
80. Yang, B.; Niu, K.; Haag, F.; Cao, N.; Zhang, J.; Zhang, H.; Li, Q.; Allegretti, F.; Björk, J.; Barth, J. V.; Chi, L., Abiotic Formation of an Amide Bond via Surface-Supported Direct Carboxyl–Amine Coupling. *Angewandte Chemie International Edition* **2022,** *61* (5).
81. Schmitz, C. H.; Ikonomov, J.; Sokolowski, M., Two-Dimensional Ordering of Poly(p-phenylene-terephthalamide) on the Ag(111) Surface Investigated by Scanning Tunneling Microscopy. *The Journal of Physical Chemistry C* **2009,** *113* (28), 11984-11987.
82. Liu, X. H.; Mo, Y. P.; Yue, J. Y.; Zheng, Q. N.; Yan, H. J.; Wang, D.; Wan, L. J., Isomeric Routes to Schiff-Base Single-layered Covalent Organic Frameworks. *Small* **2014,** *10* (23), 4934-4939.
83. Yue, J.-Y.; Mo, Y.-P.; Li, S.-Y.; Dong, W.-L.; Chen, T.; Wang, D., Simultaneous Construction of Two Linkages for the On-surface Synthesis of Imine–boroxine Hybrid Covalent Organic Frameworks. *Chemical Science* **2017,** *8* (3), 2169-2174.

84. Gong, Z.; Yang, B.; Lin, H.; Tang, Y.; Tang, Z.; Zhang, J.; Zhang, H.; Li, Y.; Xie, Y.; Li, Q.; Chi, L., Structural Variation in Surface-Supported Synthesis by Adjusting the Stoichiometric Ratio of the Reactants. *ACS Nano* **2016,** *10* (4), 4228-4235.
85. Fu, C.; Mikšátko, J.; Assies, L.; Vrkoslav, V.; Orlandi, S.; Kalbáč, M.; Kovaříček, P.; Zeng, X.; Zhou, B.; Muccioli, L.; Perepichka, D. F.; Orgiu, E., Surface-Confined Macrocyclization via Dynamic Covalent Chemistry. *ACS Nano* **2020,** *14* (3), 2956-2965.
86. Treier, M.; Richardson, N. V.; Fasel, R., Fabrication of Surface-Supported Low-Dimensional Polyimide Networks. *Journal of the American Chemical Society* **2008,** *130* (43), 14054-14055.
87. Schmitz, C. H.; Ikonomov, J.; Sokolowski, M., Two-Dimensional Polyamide Networks with a Broad Pore Size Distribution on the Ag(111) Surface. *The Journal of Physical Chemistry C* **2011,** *115* (15), 7270-7278.
88. Schmitz, C. H.; Schmid, M.; Gärtner, S.; Steinrück, H.-P.; Gottfried, J. M.; Sokolowski, M., Surface Polymerization of Poly(p-phenylene-terephthalamide) on Ag(111) Investigated by X-ray Photoelectron Spectroscopy and Scanning Tunneling Microscopy. *The Journal of Physical Chemistry C* **2011,** *115* (37), 18186-18194.
89. Lischka, M.; Dong, R.; Wang, M.; Martsinovich, N.; Fritton, M.; Grossmann, L.; Heckl, W. M.; Feng, X.; Lackinger, M., Competitive Metal Coordination of Hexaaminotriphenylene on Cu(111) by Intrinsic Copper Versus Extrinsic Nickel Adatoms. *Chemistry – A European Journal* **2019,** *25* (8), 1975-1983.
90. Li, Q.; Yang, B.; Björk, J.; Zhong, Q.; Ju, H.; Zhang, J.; Cao, N.; Shi, Z.; Zhang, H.; Ebeling, D.; Schirmeisen, A.; Zhu, J.; Chi, L., Hierarchical Dehydrogenation Reactions on a Copper Surface. *Journal of the American Chemical Society* **2018,** *140* (19), 6076-6082.
91. Song, L.; Yang, B.; Liu, F.; Niu, K.; Han, Y.; Wang, J.; Zheng, Y.; Zhang, H.; Li, Q.; Chi, L., Synthesis of Two-Dimensional Metal–Organic Frameworks via Dehydrogenation Reactions on a Cu(111) Surface. *The Journal of Physical Chemistry C* **2020,** *124* (23), 12390-12396.
92. Knor, M.; Gao, H.-Y.; Amirjalayer, S.; Studer, A.; Gao, H.; Du, S.; Fuchs, H., Stereoselective Formation of Coordination Polymers with 1,4-diaminonaphthalene on Various Cu Substrates. *Chemical Communications* **2015,** *51* (54), 10854-10857.
93. Ren, J.; Bao, D.-L.; Dong, L.; Gao, L.; Wu, R.; Yan, L.; Wang, A.; Yan, J.; Wang, Y.; Du, S.-X.; Huan, Q.; Gao, H.-J., Thermo-controllable Self-assembled Structures of Single-layer 4, 4″-diamino-p-terphenyl Molecules on Au (110). *Chinese Physics B* **2017,** *26* (8), 086801.
94. Cao, N.; Ding, J.; Yang, B.; Zhang, J.; Peng, C.; Lin, H.; Zhang, H.; Li, Q.; Chi, L., Deprotonation-Induced Phase Evolutions in Co-Assembled Molecular Structures. *Langmuir* **2018,** *34* (26), 7852-7858.
95. Grossmann, L.; King, B. T.; Reichlmaier, S.; Hartmann, N.; Rosen, J.; Heckl, W. M.; Björk, J.; Lackinger, M., On-surface Photopolymerization of Two-dimensional Polymers Ordered on the Mesoscale. *Nature Chemistry* **2021,** *13* (8), 730-736.

96. Murray, D. J.; Patterson, D. D.; Payamyar, P.; Bhola, R.; Song, W.; Lackinger, M.; Schlüter, A. D.; King, B. T., Large Area Synthesis of a Nanoporous Two-Dimensional Polymer at the Air/Water Interface. *Journal of the American Chemical Society* **2015,** *137* (10), 3450-3453.
97. Müller, V.; Shao, F.; Baljozovic, M.; Moradi, M.; Zhang, Y.; Jung, T.; Thompson, W. B.; King, B. T.; Zenobi, R.; Schlüter, A. D., Structural Characterization of a Covalent Monolayer Sheet Obtained by Two-Dimensional Polymerization at an Air/Water Interface. *Angewandte Chemie International Edition* **2017,** *56* (48), 15262-15266.
98. Zhong, Q.; Ihle, A.; Ahles, S.; Wegner, H. A.; Schirmeisen, A.; Ebeling, D., Constructing Covalent Organic Nanoarchitectures Molecule by Molecule via Scanning Probe Manipulation. *Nature Chemistry* **2021,** *13* (11), 1133-1139.
99. Kawai, S.; Silveira, O. J.; Kurki, L.; Yuan, Z.; Nishiuchi, T.; Kodama, T.; Sun, K.; Custance, O.; Lado, J. L.; Kubo, T.; Foster, A. S., Local Probe-induced Structural Isomerization in a One-dimensional Molecular Array. *Nature Communications* **2023,** *14* (1), 7741.
100. Gao, Y.; Albrecht, F.; Rončević, I.; Ettedgui, I.; Kumar, P.; Scriven, L. M.; Christensen, K. E.; Mishra, S.; Righetti, L.; Rossmannek, M.; Tavernelli, I.; Anderson, H. L.; Gross, L., On-surface Synthesis of a Doubly Anti-aromatic Carbon Allotrope. *Nature* **2023,** *623* (7989), 977-981.
101. Feng, M.; Petek, H.; Shi, Y.; Sun, H.; Zhao, J.; Calaza, F.; Sterrer, M.; Freund, H.-J., Cooperative Chemisorption-Induced Physisorption of CO2 Molecules by Metal–Organic Chains. *ACS Nano* **2015,** *9* (12), 12124-12136.
102. Abyazisani, M.; MacLeod, J. M.; Lipton-Duffin, J., Cleaning Up after the Party: Removing the Byproducts of On-Surface Ullmann Coupling. *ACS Nano* **2019,** *13* (8), 9270-9278.
103. Tran, B. V.; Pham, T. A.; Grunst, M.; Kivala, M.; Stöhr, M., Surface-Confined [2 + 2] Cycloaddition Towards One-dimensional Polymers Featuring Cyclobutadiene units. *Nanoscale* **2017,** *9* (46), 18305-18310.
104. Bronner, C.; Björk, J.; Tegeder, P., Tracking and Removing Br during the On-Surface Synthesis of a Graphene Nanoribbon. *The Journal of Physical Chemistry C* **2015,** *119* (1), 486-493.
105. Kestell, J.; Boscoboinik, J. A.; Cheng, L.; Garvey, M.; Bennett, D. W.; Tysoe, W. T., Structural Changes in Self-Catalyzed Adsorption of Carbon Monoxide on 1,4-Phenylene Diisocyanide Modified Au(111). *The Journal of Physical Chemistry C* **2015,** *119* (32), 18317-18325.
106. De Marchi, F.; Galeotti, G.; Simenas, M.; Tornau, E. E.; Pezzella, A.; Macleod, J.; Ebrahimi, M.; Rosei, F., Room-temperature Surface-assisted Reactivity of a Melanin Precursor: Silver Metal–organic Coordination *versus* Covalent Dimerization on Gold. *Nanoscale* **2018,** *10* (35), 16721-16729.
107. Ji, P.; Galeotti, G.; De Marchi, F.; Cui, D.; Sun, K.; Zhang, H.; Contini, G.; Ebrahimi, M.; MacLean, O.; Rosei, F.; Chi, L., Oxygen-Induced 1D to 2D Transformation of On-Surface Organometallic Structures. *Small* **2020,** *16* (35),

2002393.
108. Bischoff, F.; Seufert, K.; Auwärter, W.; Joshi, S.; Vijayaraghavan, S.; Écija, D.; Diller, K.; Papageorgiou, A. C.; Fischer, S.; Allegretti, F.; Duncan, D. A.; Klappenberger, F.; Blobner, F.; Han, R.; Barth, J. V., How Surface Bonding and Repulsive Interactions Cause Phase Transformations: Ordering of a Prototype Macrocyclic Compound on Ag(111). *ACS Nano* **2013,** *7* (4), 3139-3149.
109. Shchyrba, A.; Wäckerlin, C.; Nowakowski, J.; Nowakowska, S.; Björk, J.; Fatayer, S.; Girovsky, J.; Nijs, T.; Martens, S. C.; Kleibert, A.; Stöhr, M.; Ballav, N.; Jung, T. A.; Gade, L. H., Controlling the Dimensionality of On-Surface Coordination Polymers via Endo- or Exoligation. *Journal of the American Chemical Society* **2014,** *136* (26), 9355-9363.
110. Yau, S.; Lee, Y.; Chang, C.; Fan, L.; Yang, Y.; Dow, W.-P., Structures of Aniline and Polyaniline Molecules Adsorbed on Au(111) Electrode: as Probed by in Situ STM, ex Situ XPS, and NEXAFS. *The Journal of Physical Chemistry C* **2009,** *113* (31), 13758-13764.
111. Grill, L.; Dyer, M.; Lafferentz, L.; Persson, M.; Peters, M. V.; Hecht, S., Nano-architectures by Covalent Assembly of Molecular Building Blocks. *Nature Nanotechnology* **2007,** *2* (11), 687-691.
112. Bieri, M.; Treier, M.; Cai, J.; Aït-Mansour, K.; Ruffieux, P.; Gröning, O.; Gröning, P.; Kastler, M.; Rieger, R.; Feng, X.; Müllen, K.; Fasel, R., Porous graphenes: Two-dimensional Polymer Synthesis with Atomic Precision. *Chemical Communications* **2009,** (45), 6919.
113. Goronzy, D. P.; Ebrahimi, M.; Rosei, F.; Arramel; Fang, Y.; De Feyter, S.; Tait, S. L.; Wang, C.; Beton, P. H.; Wee, A. T. S.; Weiss, P. S.; Perepichka, D. F., Supramolecular Assemblies on Surfaces: Nanopatterning, Functionality, and Reactivity. *ACS Nano* **2018,** *12* (8), 7445-7481.
114. Lin, N.; Stepanow, S.; Ruben, M.; Barth, J. V., Surface-Confined Supramolecular Coordination Chemistry. In *Templates in Chemistry III*, Broekmann, P.; Dötz, K.-H.; Schalley, C. A., Eds. Springer Berlin Heidelberg: Berlin, Heidelberg, 2009; pp 1-44.
115. Barth, J. V.; Costantini, G.; Kern, K., Engineering Atomic and Molecular Nanostructures at Surfaces. *Nature* **2005,** *437* (7059), 671-679.
116. Barth, J. V.; Weckesser, J.; Lin, N.; Dmitriev, A.; Kern, K., Supramolecular Architectures and Nanostructures at Metal Surfaces. *Applied Physics A* **2003,** *76* (5), 645-652.
117. Dong, L.; Gao, Z. A.; Lin, N., Self-assembly of Metal–organic Coordination Structures on Surfaces. *Progress in Surface Science* **2016,** *91* (3), 101-135.
118. Écija, D.; Urgel, J. I.; Seitsonen, A. P.; Auwärter, W.; Barth, J. V., Lanthanide-Directed Assembly of Interfacial Coordination Architectures–From Complex Networks to Functional Nanosystems. *Accounts of Chemical Research* **2018,** *51* (2), 365-375.
119. Parreiras, S. O.; Martín-Fuentes, C.; Moreno, D.; Mathialagan, S. K.; Biswas, K.; Muñiz-Cano, B.; Lauwaet, K.; Valvidares, M.; Valbuena, M. A.; Urgel, J. I.; Gargiani, P.; Camarero, J.; Miranda, R.; Martínez, J. I.; Gallego, J. M.; Écija, D., 2D Co-Directed

Metal–Organic Networks Featuring Strong Antiferromagnetism and Perpendicular Anisotropy. *Small* **2024,** *20* (22), 2309555.

120. Urgel, J. I.; Ecija, D. Auwärter, W.; Stassen, D.; Bonifazi, D.; Barth, J. V., Orthogonal Insertion of Lanthanide and Transition-Metal Atoms in Metal–Organic Networks on Surfaces. *Angewandte Chemie International Edition* **2015,** *54* (21), 6163-6167.

121. Uphoff, M.; Michelitsch, G. S.; Hellwig, R.; Reuter, K.; Brune, H.; Klappenberger, F.; Barth, J. V., Assembly of Robust Holmium-Directed 2D Metal–Organic Coordination Complexes and Networks on the Ag(100) Surface. *ACS Nano* **2018,** *12* (11), 11552-11560.

122. Moreno, D.; Parreiras, S. O.; Urgel, J. I.; Muñiz-Cano, B.; Martín-Fuentes, C.; Lauwaet, K.; Valvidares, M.; Valbuena, M. A.; Gallego, J. M.; Martínez, J. I.; Gargiani, P.; Camarero, J.; Miranda, R.; Écija, D., Engineering Periodic Dinuclear Lanthanide-Directed Networks Featuring Tunable Energy Level Alignment and Magnetic Anisotropy by Metal Exchange (Small 22/2022). *Small* **2022,** *18* (22), 2270117.

123. Lafferentz, L.; Eberhardt, V.; Dri, C.; Africh, C.; Comelli, G.; Esch, F.; Hecht, S.; Grill, L., Controlling On-surface Polymerization by Hierarchical and Substrate-directed growth. *Nature Chemistry* **2012,** *4* (3), 215-220.

124. Franc, G.; Gourdon, A., Covalent Networks Through On-surface Chemistry in Ultra-High Vacuum: State-of-The-Art and Recent Developments. *Physical Chemistry Chemical Physics* **2011,** *13* (32), 14283-14292.

125. Fan, Q.; Gottfried, J. M.; Zhu, J., Surface-Catalyzed C–C Covalent Coupling Strategies toward the Synthesis of Low-Dimensional Carbon-Based Nanostructures. *Accounts of Chemical Research* **2015,** *48* (8), 2484-2494.

126. Krasnikov, S. A.; Doyle, C. M.; Sergeeva, N. N.; Preobrajenski, A. B.; Vinogradov, N. A.; Sergeeva, Y. N.; Zakharov, A. A.; Senge, M. O.; Cafolla, A. A., Formation of Extended Covalently Bonded Ni Porphyrin Networks on the Au(111) surface. *Nano Research* **2011,** *4* (4), 376-384.

127. Zhang, Y.-Q.; Kepčija, N.; Kleinschrodt, M.; Diller, K.; Fischer, S.; Papageorgiou, A. C.; Allegretti, F.; Björk, J.; Klyatskaya, S.; Klappenberger, F.; Ruben, M.; Barth, J. V., Homo-coupling of Terminal Alkynes on a Noble Metal Surface. *Nature Communications* **2012,** *3* (1), 1286.

128. Sun, Q.; Cai, L.; Ma, H.; Yuan, C.; Xu, W., Dehalogenative Homocoupling of Terminal Alkynyl Bromides on Au(111): Incorporation of Acetylenic Scaffolding into Surface Nanostructures. *ACS Nano* **2016,** *10* (7), 7023-7030.

129. Piquero-Zulaica, I.; Hu, W.; Seitsonen, A. P.; Haag, F.; Küchle, J.; Allegretti, F.; Lyu, Y.; Chen, L.; Wu, K.; El-Fattah, Z. M. A.; Aktürk, E.; Klyatskaya, S.; Ruben, M.; Muntwiler, M.; Barth, J. V.; Zhang, Y.-Q., Unconventional Band Structure via Combined Molecular Orbital and Lattice Symmetries in a Surface-Confined Metallated Graphdiyne Sheet. *Advanced Materials* **2024,** *36* (31), 2405178.

130. Shu, C.-H.; He, Y.; Zhang, R.-X.; Chen, J.-L.; Wang, A.; Liu, P.-N., Atomic-Scale Visualization of Stepwise Growth Mechanism of Metal-Alkynyl Networks on Surfaces.

Journal of the American Chemical Society **2020,** *142* (39), 16579-16586.
131. Yang, Z.; Sander, T.; Gebhardt, J.; Schaub, T. A.; Schönamsgruber, J.; Soni, H. R.; Görling, A.; Kivala, M.; Maier, S., Metalated Graphyne-Based Networks as Two-Dimensional Materials: Crystallization, Topological Defects, Delocalized Electronic States, and Site-Specific Doping. *ACS Nano* **2020,** *14* (12), 16887-16896.
132. Rabia, A.; Tumino, F.; Milani, A.; Russo, V.; Bassi, A. L.; Bassi, N.; Lucotti, A.; Achilli, S.; Fratesi, G.; Manini, N.; Onida, G.; Sun, Q.; Xu, W.; Casari, C. S., Structural, Electronic, and Vibrational Properties of a Two-Dimensional Graphdiyne-like Carbon Nanonetwork Synthesized on Au(111): Implications for the Engineering of sp-sp2 Carbon Nanostructures. *ACS Applied Nano Materials* **2020,** *3* (12), 12178-12187.
133. Lalonde, M.; Bury, W.; Karagiaridi, O.; Brown, Z.; Hupp, J. T.; Farha, O. K., Transmetalation: Routes to Metal Exchange Within Metal–organic Frameworks. *Journal of Materials Chemistry A* **2013,** *1* (18), 5453-5468.
134. Noori, Y.; Akhbari, K., Post-synthetic Ion-exchange Process in Nanoporous Metal–organic Frameworks; An Effective Way for Modulating Their Structures and Properties. *RSC Advances* **2017,** *7* (4), 1782-1808.
135. Xu, M.-M.; Chen, Q.; Xie, L.-H.; Li, J.-R., Exchange Reactions in Metal-organic Frameworks: New advances. *Coordination Chemistry Reviews* **2020,** *421*, 213421.
136. Doyle, C. M.; Cunniffe, J. P.; Krasnikov, S. A.; Preobrajenski, A. B.; Li, Z.; Sergeeva, N. N.; Senge, M. O.; Cafolla, A. A., Ni–Cu Ion Exchange Observed for Ni(ii)–Porphyrins on Cu(111). *Chemical Communications* **2014,** *50* (26), 3447.
137. Li, J.; Fan, Y.; Ren, Y.; Liao, J.; Qi, C.; Jiang, H., Development of Isostructural Porphyrin–Salen Chiral Metal–Organic Frameworks through Postsynthetic Metalation Based on Single-Crystal to Single-Crystal Transformation. *Inorganic Chemistry* **2018,** *57* (3), 1203-1212.
138. Gottfried, J. M., Surface Chemistry of Porphyrins and Phthalocyanines. *Surface Science Reports* **2015,** *70* (3), 259-379.
139. Rieger, A.; Schnidrig, S.; Probst, B.; Ernst, K.-H.; Wäckerlin, C., Ranking the Stability of Transition-Metal Complexes by On-Surface Atom Exchange. *The Journal of Physical Chemistry Letters* **2017,** *8* (24), 6193-6198.
140. Zhang, Y.-Q.; Paszkiewicz, M.; Du, P.; Zhang, L.; Lin, T.; Chen, Z.; Klyatskaya, S.; Ruben, M.; Seitsonen, A. P.; Barth, J. V.; Klappenberger, F., Complex Supramolecular Interfacial Tessellation Through Convergent Multi-Step Reaction of a Dissymmetric Simple Organic Precursor. *Nature Chemistry* **2018,** *10* (3), 296-304.
141. Abd El-Fattah, Z. M.; Kher-Elden, M. A.; Piquero-Zulaica, I.; De Abajo, F. J. G.; Ortega, J. E., Graphene: Free Electron Scattering Within an Inverted Honeycomb Lattice. *Physical Review B* **2019,** *99* (11).
142. Piquero-Zulaica, I.; Lobo-Checa, J.; El-Fattah, Z. M. A.; Ortega, J. E.; Klappenberger, F.; Auwärter, W.; Barth, J. V., Engineering Quantum States and Electronic Landscapes Through Surface Molecular Nanoarchitectures. *Reviews of Modern Physics* **2022,** *94* (4).
143. Piquero-Zulaica, I.; Lobo-Checa, J.; Sadeghi, A.; El-Fattah, Z. M. A.; Mitsui, C.;

Okamoto, T.; Pawlak, R.; Meier, T.; Arnau, A.; Ortega, J. E.; Takeya, J.; Goedecker, S.; Meyer, E.; Kawai, S., Precise Engineering of Quantum Dot Array Coupling Through Their Barrier Widths. *Nature Communications* **2017,** *8* (1).

144. Piquero-Zulaica, I.; Abd El-Fattah, Z. M.; Popova, O.; Kawai, S.; Nowakowska, S.; Matena, M.; Enache, M.; Stöhr, M.; Tejeda, A.; Taleb, A.; Meyer, E.; Ortega, J. E.; Gade, L. H.; Jung, T. A.; Lobo-Checa, J., Effective Determination of Surface Potential Landscapes from Metal-Organic Nanoporous Network Overlayers. *New Journal of Physics* **2019,** *21* (5), 053004.

145. Dong, R.; Zhang, T.; Feng, X., Interface-Assisted Synthesis of 2D Materials: Trend and Challenges. *Chemical Reviews* **2018,** *118* (13), 6189-6235.

146. Furukawa, H.; Cordova, K. E.; O'Keeffe, M.; Yaghi, O. M., The Chemistry and Applications of Metal-Organic Frameworks. *Science* **2013,** *341* (6149), 1230444.

147. Klappenberger, F., Two-dimensional Functional Molecular Nanoarchitectures – Complementary Investigations with Scanning Tunneling Microscopy and X-ray Spectroscopy. *Progress in Surface Science* **2014,** *89* (1), 1-55.

148. Vaňo, V.; Reale, S.; Silveira, O. J.; Longo, D.; Amini, M.; Kelai, M.; Lee, J.; Martikainen, A.; Kezilebieke, S.; Foster, A. S.; Lado, J. L.; Donati, F.; Liljeroth, P.; Yan, L., Emergence of Exotic Spin Texture in Supramolecular Metal Complexes on a 2D Superconductor. *Physical Review Letters* **2024,** *133* (23), 236203.

149. Lowe, B.; Field, B.; Hellerstedt, J.; Ceddia, J.; Nourse, H. L.; Powell, B. J.; Medhekar, N. V.; Schiffrin, A., Local Gate Control of Mott Metal-Insulator Transition In a 2D Metal-Organic Framework. *Nature Communications* **2024,** *15* (1), 3559.

150. Kumar, A.; Banerjee, K.; Foster, A. S.; Liljeroth, P., Two-Dimensional Band Structure in Honeycomb Metal–Organic Frameworks. *Nano Letters* **2018,** *18* (9), 5596-5602.

151. Lyu, C.; Gao, Y.; Zhou, K.; Hua, M.; Shi, Z.; Liu, P.-N.; Huang, L.; Lin, N., On-Surface Self-Assembly Kinetic Study of Cu-Hexaazatriphenylene 2D Conjugated Metal–Organic Frameworks on Coinage Metals and MoS_2 Substrates. *ACS Nano* **2024,** *18* (30), 19793-19801.

152. Lobo-Checa, J.; Hernández-López, L.; Otrokov, M. M.; Piquero-Zulaica, I.; Candia, A. E.; Gargiani, P.; Serrate, D.; Delgado, F.; Valvidares, M.; Cerdá, J.; Arnau, A.; Bartolomé, F., Ferromagnetism on an Atom-Thick & Extended 2D Metal-Organic Coordination Network. *Nature Communications* **2024,** *15* (1), 1858.

153. Hou, R.; Guo, Y.; Yi, Z.; Zhang, Z.; Zhang, C.;Xu, W., Construction and Structural Transformation of Metal–Organic Nanostructures Induced by Alkali Metals and Alkali Metal Salts. *The Journal of Physical Chemistry Letters* **2023,** *14* (15), 3636-3642.

154. Shan, H.; Zhou, L.; Ji, W.; Zhao, A., Flexible Alkali–Halogen Bonding in Two Dimensional Alkali-Metal Organic Frameworks. *The Journal of Physical Chemistry Letters* **2021,** *12* (44), 10808-10814.

155. Skomski, D.; Abb, S.; Tait, S. L., Robust Surface Nano-Architecture by Alkali–Carboxylate Ionic Bonding. *Journal of the American Chemical Society* **2012,** *134* (34),

14165-14171.
156. Liu, J.; Li, J.; Xu, Z.; Zhou, X.; Xue, Q.; Wu, T.; Zhong, M.; Li, R.; Sun, R.; Shen, Z.; Tang, H.; Gao, S.; Wang, B.; Hou, S.; Wang, Y., On-Surface Preparation of Coordinated Lanthanide-Transition-Metal Clusters. *Nature Communications* **2021,** *12* (1), 1619.
157. Parreiras, S. O.; Moreno, D.; Cirera, B.; Valbuena, M. A.; Urgel, J. I.; Paradinas, M.; Panighel, M.; Ajejas, F.; Niño, M. A.; Gallego, J. M.; Valvidares, M.; Gargiani, P.; Kuch, W.; Martínez, J. I.; Mugarza, A.; Camarero, J.; Miranda, R.; Perna, P.; Écija, D., Tuning the Magnetic Anisotropy of Lanthanides on a Metal Substrate by Metal–Organic Coordination. *Small* **2021,** *17* (35), 2102753.
158. Wang, Y.; Li, X.; Yang, Q.; Shen, Q.; He, Y.; Zhang, Y.;Wang, Y., Multinuclear Metal-Organic Coordination Structures Containing Metal-Cluster Nodes Studied by Scanning Tunneling Microscopy. *Fundamental Research* **2023**.
159. Krull, C.; Castelli, M.; Hapala, P.; Kumar, D.; Tadich, A.; Capsoni, M.; Edmonds, M. T.; Hellerstedt, J.; Burke, S. A.; Jelinek, P.; Schiffrin, A., Iron-Based Trinuclear Metal-Organic Nanostructures on a Surface with Local Charge Accumulation. *Nature Communications* **2018,** *9* (1).
160. Das, L. K.; Biswas, A.; Kinyon, J. S.; Dalal, N. S.; Zhou, H.; Ghosh, A., Di-, Tri-, and Tetranuclear Nickel(II) Complexes with Oximato Bridges: Magnetism and Catecholase-like Activity of Two Tetranuclear Complexes Possessing Rhombic Topology. *Inorganic Chemistry* **2013,** *52* (20), 11744-11757.
161. Bebensee, F.; Svane, K.; Bombis, C.; Masini, F.; Klyatskaya, S.; Besenbacher, F.; Ruben, M.; Hammer, B.; Linderoth, T. R., A Surface Coordination Network Based on Copper Adatom Trimers. *Angewandte Chemie International Edition* **2014,** *53* (47), 12955-12959.
162. Kang, L.-X.; Wang, B.-X.; Zhang, X.-Y.; Zhu, Y.-C.; Li, D.-Y.; Liu, P.-N., Construction of Two-Dimensional Organometallic Coordination Networks with Both Organic Kagome and Semiregular Metal Lattices on Au(111). *The Journal of Physical Chemistry Letters* **2024,** *15* (23), 6108-6114.
163. Lalonde, M.; Bury, W.; Karagiaridi, O.; Brown, Z.; Hupp, J. T.; Farha, O. K., Transmetalation: Routes to Metal Exchange Within Metal–organic Frameworks. *Journal of Materials Chemistry A* **2013,** *1* (18), 5453.
164. Shen, K.; Narsu, B.; Ji, G.; Sun, H.; Hu, J.; Liang, Z.; Gao, X.; Li, H.; Li, Z.; Song, B.; Jiang, Z.; Huang, H.; Justin; Song, F., On-surface Manipulation of Atom Substitution Between Cobalt Phthalocyanine and the Cu(111) Substrate. *RSC Advances* **2017,** *7* (23), 13827-13835.
165. Sun, Y.; Fan, W.; Li, Y.;Sui, N. L. D.; Zhu, Z.; Zhou, Y.; Lee, J.-M., Tuning Coordination Structures of Zn Sites Through Symmetry-Breaking Accelerates Electrocatalysis. *Advanced Materials* **2024,** *36* (4), 2306687.
166. Lu, A.-Y.; Zhu, H.; Xiao, J.; Chuu, C.-P.; Han, Y.; Chiu, M.-H.; Cheng, C.-C.; Yang, C.-W.; Wei, K.-H.; Yang, Y.; Wang, Y.; Sokaras, D.; Nordlund, D.; Yang, P.; Muller, D. A.; Chou, M.-Y.; Zhang, X.; Li, L.-J., Janus Monolayers of Transition Metal

Dichalcogenides. *Nature Nanotechnology* **2017,** *12* (8), 744-749.
167. Zhang, Y.; Chen, Y.; Wang, X.; Feng, Y.; Zhang, H.; Zhang, G., Self-Polarization Triggered Multiple Polar Units Toward Electrochemical Reduction of CO2 to Ethanol with High Selectivity. *Angewandte Chemie International Edition* **2023,** *62* (26), e202302241.
168. Nishio, M., CH/π Hydrogen Bonds in Crystals. *CrystEngComm* **2004,** *6* (27), 130-158.
169. Saravanan, R. K.; Saha, P.; Venkatesh, V.; Gopakumar, T. G.;Verma, S., Coordination-Controlled One-Dimensional Molecular Chains in Hexapodal Adenine–Silver Ultrathin Films. *Inorganic Chemistry* **2017,** *56* (7), 3976-3982.
170. Castiñeiras, A.; Fernández-Hermida, N.; García-Santos, I.; Pérez-Lustres, J. L.; Rodríguez-González, I., Luminescent Complexes of Silver(i) with Pyridylbis(3-Hexamethyleneiminyl Thiosemicarbazone): Effect of the Counterion on the Nuclearity. *Dalton Transactions* **2012,** *41* (13), 3787-3796.
171. Schmidbaur, H.; Schier, A., Argentophilic Interactions. *Angewandte Chemie International Edition* **2015,** *54* (3), 746-784.
172. Sun, Q.; Cai, L.; Wang, S.; Widmer, R.; Ju, H.; Zhu, J.; Li, L.; He, Y.; Ruffieux, P.; Fasel, R.; Xu, W., Bottom-Up Synthesis of Metalated Carbyne. *Journal of the American Chemical Society* **2016,** *138* (4), 1106-1109.
173. Peng, X.; Mahalingam, H.; Dong, S.; Mutombo, P.; Su, J.; Telychko, M.; Song, S.; Lyu, P.; Ng, P. W.; Wu, J.; Jelínek, P.; Chi, C.; Rodin, A.; Lu, J., Visualizing designer quantum states in stable macrocycle quantum corrals. *Nature Communications* **2021,** *12* (1), 5895.
174. Braun, S.; Salaneck, W. R.; Fahlman, M., Energy-Level Alignment at Organic/Metal and Organic/Organic Interfaces. *Advanced Materials* **2009,** *21* (14-15), 1450-1472.

Acknowlegement

Finally, I would like to express my heartfelt gratitude to everyone who contributed to this work.

First and foremost, I extend my deepest thanks to Prof. Johannes V. Barth for providing me with an invaluable learning opportunity and an exceptional research platform. His insightful guidance and unwavering support have been instrumental in the development of the research presented in this paper. Beyond his academic mentorship, his remarkable personality and passion for science have left a lasting impression on me, continually inspiring my dedication to scientific exploration and fostering a profound appreciation for the beauty of life.

Secondly, I sincerely thank Prof. Biao Yang for his patient guidance, which introduced me to STM area and led me to complete these projects. His management of JT-STM lab deepened my understanding of STM and instilled excellent habits in its use. I am also grateful for his influence on my analytical and problem-solving skills, which have greatly shaped my thinking. His long-term support and encouragement have been invaluable, and he will be an important guide and friend to me.

I would like to extend my sincere gratitude to Dr. Allegretti Francesco and Dr. Ignacio Piquero-Zulaica for their collaboration and guidance throughout these projects, which made this research possible.

I am also deeply thankful to Prof. Peter Feulner and Karl Eberle for their technical support in ESCA lab and JT-STM lab. Their expertise and dedication ensured the smooth operation of the lab, and I greatly appreciate their contributions. Special thanks go to Dr. Knud Seufert for his support with AFM and JT-STM. I would also like to thank Victoria Blaschek for her consistent organizational support, which allowed us to focus on our research. Additionally, I am grateful to Dr. Joachim Reichert and Prof. Wilhelm Auwärter for their assistance during my time in E20.

My heartfelt thanks go to Dr. Nan Cao, Dr. Hongxiang Xu, Shengming Zhang, Pengfei Zhao, and Longfeng Huang. Your friendship and support have meant the world to me and will always hold a special place in my life. You made my time in Germany truly unforgettable. I also extend my gratitude to all members of E20 for their help and

encouragement over the years.

Last but not least, I would like to express my deepest thanks to my family and my girlfriend for their unwavering understanding, love, and support throughout this journey.